Test of the Electroweak Sector of the Standard Model by Measuring the Anomalous $WW\gamma$ Couplings

by

Tom Fahland

B.S., University of California, Riverside, 1991
Sc.M., Brown University, 1993

Thesis

Submitted in partial fulfillment of the requirements for
the Degree of Doctor of Philosophy
in the Department of Physics at Brown University

May 1997

This dissertation by Tom Fahland is accepted in its present form by
the Department of Physics as satisfying the
dissertation requirement for the degree of
Doctor of Philosophy

Date ....
Dave Cutts

Recommended to the Graduate Council

Date ....
Robert Lanou

Date ....
Gerry Guralnik

Approved by the Graduate Council

Date ....

Abstract of "Test of the Electroweak Sector of the Standard Model by Measuring the Anomalous $WW\gamma$ Couplings," by Tom Fahland, Ph.D., Brown University, May 1997

An analysis of $W\gamma$ events has been performed in $\overline{p}p$ collisions at $\sqrt{s} = 1.8$ TeV with data collected using the DØ detector from the 1994-1995 Tevatron run at Fermilab. The process $W\gamma \rightarrow \mu\nu\gamma$ was studied using a total integrated luminosity of 73.0 pb^{-1}. Fifty-eight candidate events were identified including an estimated backgound of 23.3 events. The total cross section for $p\overline{p} \rightarrow W\gamma + X$ (for $p_T^\gamma > 10$ GeV/c and $\Delta R_{\mu\gamma} > 0.7$) times the branching ratio of W bosons to muons is measured to be:

$$\sigma(p\overline{p} \rightarrow W\gamma + X) \times \mathrm{BR}(W \rightarrow \mu\nu) = 13.1^{+3.2}_{-2.8} \pm 2.11\ (syst)\ \pm 1.6\ (lum)\ \mathrm{pb}.$$

Limits on $WW\gamma$ couplings are obtained from a maximum likelihood fit to the photon transverse momentum distribution. Assuming a form factor scale of $\Lambda = 1.5$ TeV, the 95% CL limits on the CP-conserving couplings are $-1.95 < \Delta\kappa < 1.95$, $-0.52 < \lambda < 0.52$. This analysis is combined with the $W\gamma \rightarrow e\nu\gamma$ analysis to produce the tightest possible limits on the anomalous couplings. The combined 95% CL limits are $-0.98 < \Delta\kappa < 1.01$, and $-0.33 < \lambda < 0.31$ with similar limits on the CP-violating couplings.

Acknowledgments

It is customary at this point to give thanks to the many helpful people who along the way have given me the opportunity to finish this work. This dissertation not only represents my work, but the work of countless others who contributed in many ways. It all starts with my thesis advisor, Dave Cutts. He has always treated me fairly and provided me with the necessary tools to allow me to perform my work. Knowing I had moral and financial support throughout graduate school meant I had one less thing to worry about. Also I was able to travel to some cool conferences to show my work. I would also like to thank the others members of my thesis committee including Robert Lanou and Gerry Guralnik for reading my thesis and giving me comments.

Next I would like to thank some of the people in the diboson group and others who have given me considerable help with the analysis. Brajesh Choudary deserves some special mention as he helped me starting out when I was totally clueless and gave me some direction. I will surely forget some, but a few of the other people are Mike Kelly, Steve Glenn, Paul Bloom, Greg Landsberg, Taka Yasuda, Paul Quintas, Darien Wood, Uli Baur, etc. Special thanks to John Ellison, the chair of my editorial board who helped push this analysis through completion. I also want to thank Ellizabeth Gallas who wrote the MTC package that greatly improved the signal-to-noise ratio of this analysis.

There are also many friends at Fermilab I would like to thank for various reasons. I want to thank some of my fellow Brown colleagues for helping me out in different aspects of the PhD experience, namely Freddy Nang, David Cullen, Jeff Bantly, Jan Hoftun, Gordan Watts, and Howei Xu. I must thank the 'large' number of people subsidizing my income by entering all my sports pools, a few of those contributors are Freedy, Bryan, Gian, Sal, Peter, Jamal, Bill C., Jim J., David C., Gene, Tom M., Andrew, Eric, and many others (you were very kind!) Also I need to thank Freedy and Ray F. who pushed me to continue to go to the gym to get in good shape. (Some days were very boring). I can't forget Darien Wood and Joe Incandela who got me into rock climbing; this turned out to be one of my favorite pastimes. Going back further in the past, I want to thank some of my friends at Brown including Mohan, Jay, Khurram, Bill, Antonella, Kostas, etc. They helped me get through the first year of graduate school which is the toughest year. Going back even further I want to thank a couple friends from my undergrad years at Riverside, namely John and Joe Palmeri, Eric Schlah, and Amanda Flohr. I shared many good times with these folks. Last but not least, I thank my family. I can't forget my uncle, Ron Johnson, who provided me a fun place to go skiing (Colorado) for Christmas while in grad school. I dedicate this dissertation to my father who passed away while I was in graduate school. He always had a special interest in science.

Contents

List of Tables

List of Figures

Chapter 1

Introduction

For thousands of years people have been trying to understand how the universe around them operates. In the last few decades, high energy physics has made great strides in understanding the fundamental building blocks in nature. This thesis describes in detail the $WW\gamma$ interaction which can be used to test the Standard Model of particle physics. The analysis was performed using the DØ detector at the Fermi National Accelerator Laboratory.

The $WW\gamma$ interaction is probed by studying the process $\overline{p}p \rightarrow W\gamma \rightarrow \mu\nu\gamma$. By measuring the cross section for this proccess and by using some kinematic infomation from the interactions, limits on the anomalous couplings are determined.

A short outline of this thesis is given below. Chapter 2 provides an introduction to the Standard Model and explains in some detail the trilinear vector boson couplings in this framework. This is only an introduction; references are provided for more extensive information about the complete theoretical aspects of the Standard Model. Chapter 3 describes the DØ detector and triggering systems used to collect the data as well as the Tevatron accelerator. Chapter 4 describes the offline algorithms and reconstruction programs used to process the candidate events. The particle identification variables that are used in the selection are described in detail. Chapter 5 describes the data selection, offline event selection, and calculation of all the efficiencies including the trigger and particle identification efficiencies. The calculation of all the backgrounds to the signal is described in chapter 6. Chapter 7 describes in detail the results of this analysis of $W\gamma \rightarrow \mu\nu\gamma$ events. First, the cross section calculation is described and compared to the theoretical predictions. The technique used in determining confidence level limits on the anomalous couplings is discussed. Two methods are used to calculate limits on the anomalous couplings; a fit to the measured cross section and a fit to the observed p_T spectrum of the photon. Results from this analysis are combined with the analysis of $W\gamma \rightarrow e\nu\gamma$ events to produce a combined limit on the anomalous couplings.

Chapter 2

The Standard Model and Vector Boson Physics

This chapter discusses the Standard Model of particle physics and in particular, provides some detail about the electroweak sector and the self interaction of gauge bosons. The $WW\gamma$ interaction vertex is described as well as its associated production properties.

2.1 A Tour of the Standard Model

The Standard Model is a culmination of physics ideas that have been developed over roughly the last 50 years. It provides a description of nature at very small distances, distances on the order of $10^{-15}m$. For quantities that can be calculated from the Standard Model, the theory provides predictions that give a good description of nature in this regime.

The Standard Model is a theory of interacting quantum fields. It incorporates the excitations in these fields (particles) into three separate categories: quarks and leptons, gauge bosons, and Higgs particles. Quarks and leptons are spin-$\frac{1}{2}$ particles which follow the Pauli exclusion principle. The quarks and leptons are divided into three generations each of which contains two particles. Each generation of leptons consists of one charged particle (electron, muon, and tau) and its associated neutral partner (electron neutrino, muon neutrino, and tau neutrino). The charged leptons interact electromagnetically, while the neutrinos only interact by the weak interaction; thus for the most part neutrinos are not detected directly.

Quarks are also divided into three generations; the first generation consists of the up and down quarks which make up most of the matter around us. The second (charm and strange quark) and third (bottom and top quark) generation of quarks are much more massive than the first. Quarks have two major differences from that of leptons. First, they carry a fractional electric charge, and second, they interact through the strong interaction. Table 2.1 [1] shows all the quarks, leptons and gauge bosons as well as some of their properties.

The second major class of particles, the gauge bosons, is responsible for the interactions between particles. The Standard Model couples the fields of each gauge boson with the fields of all particles that feel the force. An interaction involves two couplings and can be viewed as the exchange of a virtual gauge boson between two particles. There are four fundamental forces in nature and

Table 2.1: Elementary particles of the Standard Model

Type of particle	name	Charge	Effective Mass (MeV/c^2
quark	down (d)	$-1/3$	≈ 10
	up (u)	$+2/3$	≈ 5
	strange (s)	$-1/3$	≈ 200
	charm (c)	$+2/3$	≈ 1500
	bottom (b)	$-1/3$	≈ 4500
	top (t)	$+2/3$	$\approx 170 \times 10^3$
lepton	electron	-1	0.511
	electron neutrino	0	$< 7eV$
	muon	-1	105.7
	muon neutrino	0	< 0.27
	tau	-1	1777
	tau neutrino	0	< 31
gauge bosons	photon	0	0
	W	1	80.3 GeV/c^2
	Z	0	91.2 GeV/c^2
	gluon	0	0
Higgs sector	Higgs	?	?

each has its characteristic gauge boson that mediates the force.

The strong force, also known as Quantum Chromodynamics (QCD), is mediated by gluons. Gluons couple to particles which contain 'color charge'; these include quarks and gluons. Unlike electrical charge which contains two types, the color charge has three possible values labeled 'red', 'green', and 'blue'. The strength of the strong force, parametized by the strong coupling constant, changes with the interaction energy. As the interaction energy increases, the value of the coupling becomes smaller. This means that at high energies quarks behave like free particles, a process known as 'asymptotic freedom' [2]. This feature allows one to use perturbation theory to calculate properties from QCD and make predictions.

The electromagnetic force, known as Quantum Electrodynamics (QED), is mediated by the photon, which couples to particles with electric charge. As is the case with the strong interaction, the coupling strength is not a constant. The larger the interaction energy becomes, the larger the coupling gets.

The weak force is mediated by the W and Z bosons, which are very massive particles (about 80 and 90 GeV/c^2). The large mass of the W and Z bosons means the weak force acts on very short distances. A key ingredient of the Standard Model is the unification of the electromagnetic and weak force. The description of the so-called 'electroweak' force is based on the Glashow-Weinberg-Salam (GWS) theory [3]. This theory will be described in more detail in the following section. The last force is gravity, which is mediated by the graviton. The gravitational force is so weak that it can be completely ignored in high energy physics.

The last important piece of the Standard Model is the Higgs boson. By demanding gauge symmetry, theories require the associated gauge bosons to be massless. This is obviously a problem for the Standard Model which contains the massive W and Z bosons. The Higgs mechanism introduces a new scalar particle with which the W and Z bosons interact, to acquire mass. Actually, the Higgs mechanism explains how all the quarks and leptons acquire mass, via a process known as spontaneous local symmetry breaking (LSB) [4].

2.2 The Electroweak Interaction

The electroweak interaction, as was previously mentioned, is described by the GWS theory, and is based on $SU(2)_L \times U(1)_Y$ gauge symmetry. The SU(2) group is a non-Abelian group containing three generators which can be represented by W^i_μ, where $i = 1, 2, 3$. The group $U(1)_Y$ is an Abelian group with the generator given by B_μ where the quantum number Y is called the weak hypercharge and is related to the electric charge (Q) and weak isospin (t) by the following formula: $Q = t_3 + Y/2$.

The leptons are grouped into separate left-handed and right-handed fermion fields given by:

$$t = \frac{1}{2}\begin{pmatrix} \nu_l \\ l^- \end{pmatrix}_{\mathrm{L}} \begin{cases} t_3 = +1/2 \\ t_3 = -1/2 \end{cases} \qquad l = e,\ \mu,\ \tau$$

The left-handed fields transform as weak-isospin doublets, while the the right-handed fields transform as weak-isospin singlets. The Standard Model does not contain right-handed neutrino fields. The quarks are represented in a similar fashion with the doublets given by:

$$\begin{pmatrix} u_i \\ d'_i \end{pmatrix},\ u_{iR},\ and\ d_{iR}.$$

where i denotes the three quark families and d'_i are the rotated quark fields: $d'_i = \sum V_{ij} d_j$, where V_{ij} is the Cabibbo-Kobayashi-Maskawa matrix [6].

The Lagrangian for the electroweak sector introduces four gauge bosons;

W_μ^i, where $i = 1, 2, 3$ and B_μ. These boson are required to be massless, as are the fermions. In order to give the masses to the gauge bosons via (LSB), an isospin doublet of scalar Higgs fields needs to be introduced. The Higgs doublet can be represented as:

$$\phi = \begin{pmatrix} \phi^+ \\ \phi^0 \end{pmatrix} = \begin{pmatrix} \frac{1}{\sqrt{2}}(\phi_1 + i\phi_2) \\ \frac{1}{\sqrt{2}}(\phi_3 + i\phi_4) \end{pmatrix}$$

By minimizing the Higgs potential, the Higgs field can be reparameterized so that three of the four scalar ϕ_i's can be associated with a phase transformation [4]. This leaves one scalar, the Higgs scalar, with a non-zero vacuum expectation value. The mass of the Higgs boson is a free parameter and must be determined from experiment.

The total Lagrangian for the electroweak interaction can be written as

$$\mathcal{L} = \mathcal{L}_{fermion} + \mathcal{L}_{Higgs} + \mathcal{L}_{gauge\ boson}$$

The next section will go into the details of the gauge boson sector of the electroweak model.

2.3 Self Interaction of Gauge Bosons

The Lagrangian for the gauge boson portion of the Standard Model is given by

$$\mathcal{L}_g = -\frac{1}{4} W_{\mu\nu}^j W_j^{\mu\nu} - \frac{1}{4} B_{\mu\nu} B^{\mu\nu}. \tag{2.1}$$

with the following definitions

$$B_{\mu\nu} = \partial_\mu A_\nu - \partial_\nu A_\mu,$$

$$W^j_{\mu\nu} = \partial_\mu W^j_\nu - \partial_\nu W^j_\mu - g f_{jkl} W^k_\mu W^l_\nu$$

where A is the electromagnetic field tensor, W is the weak field tensor, and f_{jkl} are the structure constants of the weak isospin group. This portion of the Lagrangian is responsible for all the self-interactions of the gauge bosons. There are two types of self-interactions, the cubic couplings (WWZ, $WW\gamma$), and the quartic couplings ($WWWW$, $WWZZ$, $WWZ\gamma$, $WW\gamma\gamma$).

The gauge sector of the Standard Model contains three independent free parameters which must be measured by experiment. They consist of the fine structure constant $\alpha = e^2/(4\pi) = 1/(137.0359895 \pm 0.0000061)$, the Fermi coupling constant $G_f = (1.16639 \pm 0.00002)10^{-5}\ GeV^{-2}$, and the Weinberg mixing angle $sin^2\theta_W = 0.2319 \pm 0.0005$ [7]. Particle masses are also free parameters although all the masses have been measured except that of the Higgs boson. This allows the Standard Model to have great predictive power.

This thesis is specifically about the self-interaction of gauge bosons involving the trilinear coupling $WW\gamma$. The quartic couplings are much rarer processes that are beyond the scope of this work [8]. Examining the trilinear couplings directly tests the gauge structure of the Standard Model while studying the quartic couplings, which are more rare, give insight into the mechanism of electroweak symmetry breaking.

As mentioned previously, the Standard Model can make powerful predictions. For example, it can predict various production properties of the $WW\gamma$ vertex. The work in this thesis compares the experimental data to the predictions from the theory and looks for possible deviations from the Standard Model. The so called 'anomalous' $WW\gamma$ couplings represent a possible deviation from the Standard Model. In order to study the effects of anomalous couplings, they must be parametrized so the theory can be compared with experimental data. This is done by making a modification to the gauge boson portion of the Standard Model Lagrangian and writing an effective Lagrangian that describes the $WW\gamma$ vertex. The Lagrangian [9, 10] is given by

$$\begin{aligned}
\mathcal{L}_{WW\gamma} \;=\; & -i\,\mathrm{e}[(W^{\dagger}_{\mu\nu}W^{\mu}A^{\nu} - W^{\dagger}_{\mu}A_{\nu}W^{\mu\nu}) \\
& + \kappa\, W^{\dagger}_{\mu}W_{\nu}F^{\mu\nu} + \frac{\lambda}{m_W^2}W^{\dagger}_{\lambda\mu}W^{\mu}_{\nu}F^{\nu\lambda} \\
& + \tilde{\kappa}\, W^{\dagger}_{\mu}W_{\nu}\tilde{F}^{\mu\nu} + \frac{\tilde{\lambda}}{m_W^2}W^{\dagger}_{\lambda\mu}W^{\mu}_{\nu}\tilde{F}^{\nu\lambda}\,]
\end{aligned}$$

where $F_{\mu\nu} = \partial_\mu A_\nu - \partial_\nu A_\mu$ and $\tilde{F}^{\mu\nu} = \frac{1}{2}\epsilon_{\mu\nu kl}F^{kl}$.

The variables κ, λ, $\tilde{\kappa}$, and $\tilde{\lambda}$ are the anomalous coupling parameters. The $SU(2)_L \times U(1)_Y$ gauge structure of the Standard Model fixes the values of the parameters: $\kappa = 1$, $\lambda = \tilde{\lambda} = \tilde{\kappa} = 0$. The first two couplings κ and λ are CP-conserving while the last two, $\tilde{\kappa}$ and $\tilde{\lambda}$, are CP-violating. By measuring the production properties of $W\gamma$ production, limits can be set on the anomalous couplings.

The anomalous couplings are related to the electromagnetic multipole moments of the W boson. The couplings κ and λ are related to the electric quadrupole moment Q_W and the magnetic dipole moment μ_W by:

$$Q_W = -\frac{e}{m_W^2}\,(\kappa - \lambda)$$

and

$$\mu_W = \frac{e}{2\,m_W}\,(1 + \kappa + \lambda).$$

Similiarly, the CP-violating couplings $\tilde{\kappa}$ and $\tilde{\lambda}$ are related to the electric dipole moment d_W and the magnetic quadrupole moment Q_W^m by:

$$d_W = \frac{e}{2\,m_W}\,(\tilde{\kappa} + \tilde{\lambda})$$

and

$$Q_W^m = -\frac{e}{m_W^2}\,(\tilde{\kappa} - \tilde{\lambda}).$$

To make the anomalous couplings self-consistent, S-matrix unitarity must be respected. It can be shown that in order not to violate the unitarity limit, the couplings at high energy need to asymptotically approach the Standard Model values [11]. The method used to do this is to introduce *form factors* which are energy dependent and dampen the growth of the scattering amplitude at high energies. A generalized form factor is used, given by the following expressions, where for the dipole form, $n = 2$ is used.

$$\lambda \rightarrow \frac{\lambda}{\left(1+\frac{\hat{s}}{\Lambda^2}\right)^n} \quad \text{and} \quad \Delta\kappa \rightarrow \frac{\Delta\kappa}{\left(1+\frac{\hat{s}}{\Lambda^2}\right)^n}$$

The parameter Λ is the form factor scale for which new physics might be present. Unitarity sets limits on the anomalous couplings, these limits depend on the form factors and are given below [10]:

$$|\Delta\kappa| < 7.4 \text{ TeV}^2/\Lambda^2$$

$$|\tilde{\kappa}| < 35 \text{ TeV}/\Lambda$$

$$|\lambda|, |\tilde{\lambda}| < 4.0 \text{ TeV}^2/\Lambda^2$$

where $\Delta\kappa = \kappa - 1$.

The scale of Λ cannot be too small (of the order m_Z) since the measured properties of the W and Z bosons would be different from that of the Standard Model, which is not observed. Λ can also be viewed as a 'compositeness scale' or a scale in which new physical phenomena outside the Standard Model could exist, consistent with present measurements.

It is possible to relate the anomalous contributions to the $W\gamma$ production amplitudes in terms of the helicity states (dot product of spin and momentum) of the W and photon, β_W and β_γ. Defining these contributions by $\Delta M_{\beta_W \beta_\gamma}$

we can write:

$$(2.2) \qquad \Delta M_{\pm 0} = \frac{e^2}{sin\theta_W}\frac{\sqrt{\hat{s}}}{2M_W}[\Delta\kappa + \lambda \mp i(\tilde{\kappa} + \tilde{\lambda})]\frac{1}{2}(1 \mp cos\theta)$$

$$(2.3) \qquad \Delta M_{\pm\pm} = \frac{e^2}{sin\theta_W}\frac{1}{2}[\frac{\hat{s}}{M_W^2}(\lambda \mp i\tilde{\lambda}) + (\Delta\kappa \mp i\tilde{\kappa})]\frac{1}{\sqrt{2}}sin\theta$$

From the equations above only four pairs of helicity combinations are allowed. The combinations $(\beta_W, \beta_\gamma) = (+-)$ and $(-+)$ are forbidden by angular momentum conservation because they require a total spin of $J = 2$ for the W boson, where the W spin is equal to one. The fact that there are four allowed helicity states explains why four free parameters suffice to completely describe the $WW\gamma$ vertex.

2.3.1 Characteristics of $W\gamma$ Events

From equation 2.1 the matrix elements can be calculated for $W\gamma$ production. The W boson is a massive particle compared to other elementary particles and thus decays quickly to lighter particles.

The W boson can decay into a pair of leptons $(e\nu_e, \mu\nu_\mu, \tau\nu_\tau)$ or into hadrons $(u\bar{d}, c\bar{s})$. The hadronic decay mode of the W boson is overwhelmed by a large QCD background, so the leptonic decay mode is the only mode where a significant signal can be seen. One of the leptonic decay modes, $W \rightarrow \tau\nu_\tau$ is also very experimentally challenging; thus only the electron and muon channels are usually considered. This thesis presents an analysis of $W\gamma$ production, with the W decaying via the muon channel. It describes briefly the electron channel in a final section which combines results on the $W\gamma$ production.

The Feynman diagrams involving W production that correspond to the final state of $\mu\nu_\mu\gamma$ are shown in Figure 2.1. The first two diagrams represent initial state radiation where either one of the incoming partons or antipartons emits a hard photon by *bremsstrahlung.* Diagram (c) is the trilinear coupling ($WW\gamma$ vertex) that has been discussed; this is the only diagram that would be affected by the anomalous couplings. The last process that gives the same final state, shown in diagram (d), is radiative decay, in which a photon is emitted by the final state lepton. The first three diagrams can be classified as *production* diagrams while the last diagram is classified as a *decay* diagram.

The theoretical calculations for the Standard Model and anomalous coupling processes that are shown in Figure 2.1 were provided by U. Baur and E. Berger through a Monte Carlo generator program. This program can provide differential cross sections for many different distributions. It takes into account the finite W-width effects, interference effects, and next to leading order (NLO) effects by using a k-factor of the following form.

$$K = 1 + \frac{8\pi}{9}\alpha_s \approx 1.34$$

All the calculations are done for the Tevatron energy ($\sqrt{s} = 1.8$ TeV). At this energy the NLO contributions are not too large, but do become significant at higher center-of-mass energies. A complete simulation package that simulates

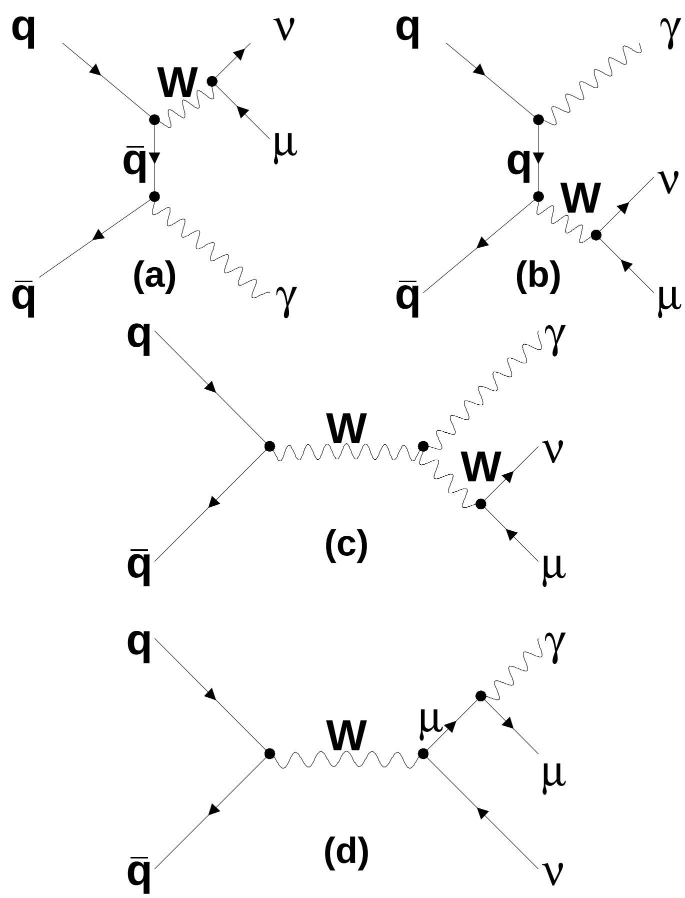

Figure 2.1: Leading order tree level Feynman diagrams for the process $q\bar{q}\rightarrow\ \mu\nu_{\mu}\gamma$ final states. Diagrams (a) and (b) represent initial state radiation and diagram (d) is a radiative decay diagram that gives the same final state. Diagram (c) is the one of interest, containing the $WW\gamma$ vertex.

the DØ detector was used with this generator, as will be described in detail later.

In order to compare the theoretical predictions with the experimental data, a few simple cuts must be applied to the Monte Carlo. The cross section for the process

$$\bar{p}p \rightarrow \mu\nu_\mu\gamma \tag{2.4}$$

contains several divergences which cause the cross section to blow up [12]. The first divergence, the *infrared divergence*, occurs when the photon energy goes to zero. The second divergence, the *collinear divergence*, occurs when the separation between the photon and the lepton shrinks to zero. These divergence are not a problem when comparing to the real experimental data because it is impossible to detect the photon under the conditions where the divergence occur. To take care of the two divergences, two cuts are applied to both the data and the Monte Carlo simulation:

$$p_t^\gamma > 10 \text{ GeV/c and } \Delta R(\mu - \gamma) \equiv \sqrt{(\Delta\phi_{\mu\gamma})^2 + (\Delta\eta_{\mu\gamma})^2} \geq 0.7$$

where p_T^γ is the photon's transverse momentum; ϕ and η are the azimuthal angle and the pseudorapidity of the particle (see section 3.3).

A principal result from the Monte Carlo calculations is the variation in the production cross section. The cross section as a function of the two anomalous couplings is shown in Figure 2.2. One can see that the cross section increases with non Standard Model couplings thus implying that the trilinear diagram contribution becomes larger for larger anomalous couplings. Thus by counting the number of observed $W\gamma$ events and measuring the cross section, the effect of the couplings can be measured.

The cross section has a minimum at the Standard Model value ($\Delta\kappa = \lambda = 0$) and can be expressed as a bilinear form of the anomalous couplings. By comparing the measured cross section to the theoretical predictions, limits can be set on the anomalous couplings. There are more advanced methods of obtaining confidence limits which will be discussed later in this section.

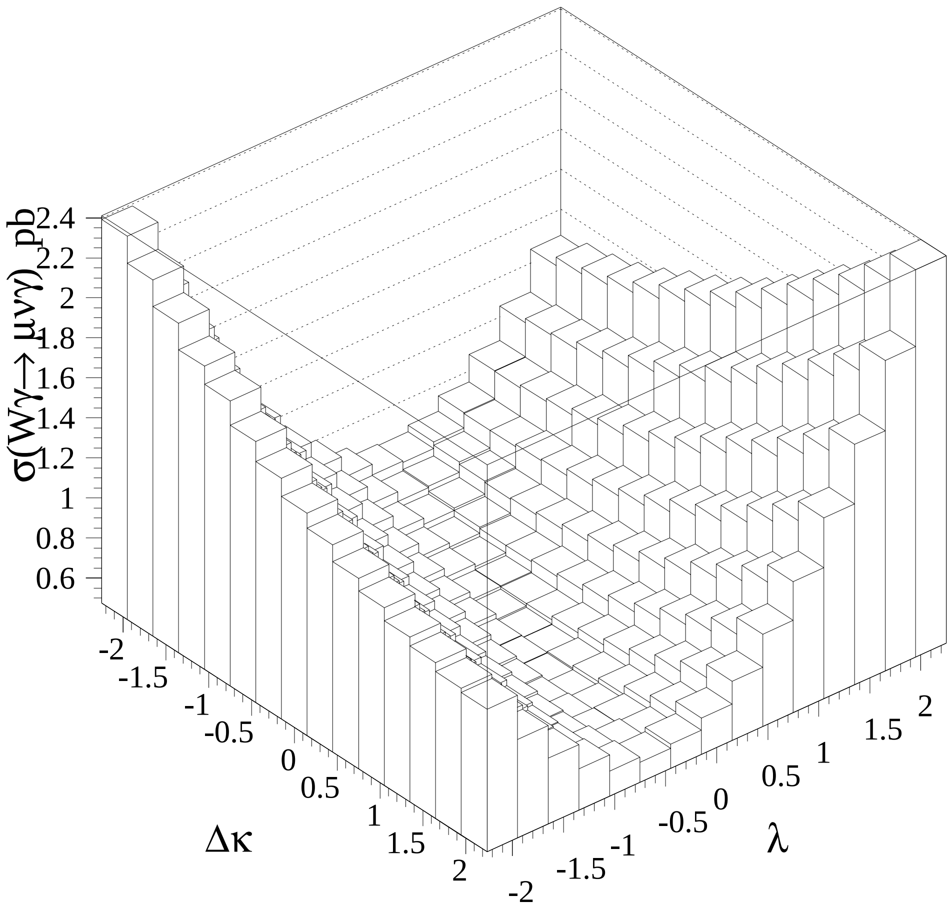

Figure 2.2: The cross section for $q\overline{q} \rightarrow W(\mu\nu)\gamma$ as a function of the anomalous couplings. The only cut applied to the Monte Carlo is the $\Delta R_{\mu\gamma}$ and p_T cut. There is a large increase in the cross section away from the standard model values of $\Delta\kappa = \lambda = 0$.

The following two figures show different kinematical distributions for the reaction $\bar{p}p \rightarrow \mu\nu_\mu\gamma$. For all the plots, the Standard Model values and those from pairs of two anomalous couplings will be shown. Figure 2.3 shows the invariant mass distribution of the $\mu\nu_\mu\gamma$ system. The solid line corresponds to the total Standard Model case and the two dashed lines correspond to the anomalous couplings shown in the figure. One can see the increase in the invariant mass distribution for the non Standard Model case. The peak at about 100 GeV/c^2 is dominated by the decay diagram. It should be noted that the effects of the anomalous couplings show up at high invariant masses; this is the reason one needs a high energy collider to probe the phase space.

The most sensitive kinematic variable to the effect of anomalous couplings is the p_T spectrum of the photon. Shown in Figure 2.4 is the p_T^γ spectrum for again the Standard Model and two variants of the model with different anomalous couplings. Anomalous couplings cause the emission of harder photons; thus by fitting the shape of the observed p_T^γ spectrum, the tightest limits can be set on the anomalous couplings. Having a cut on the photon at 10 GeV/c does not affect the sensitivity to anomalous couplings because they manifest themselves at high p_T.

The production and decay processes shown in Figure 2.1 were included together in the previous distributions. One can distinguish between the production and decay processes by making a cut on the cluster transverse mass of the $\mu\nu_\mu\gamma$ system which is given below.

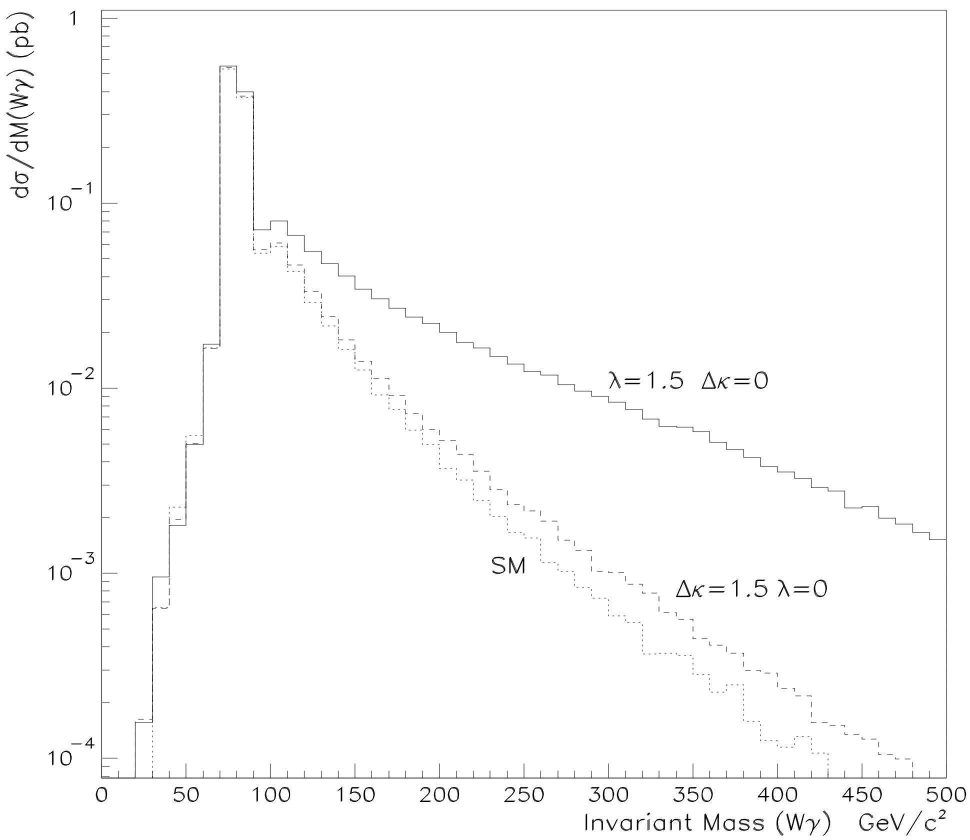

Figure 2.3: Invariant mass of the $W\gamma$ system for the reaction $q\bar{q} \to W(\mu\nu)\gamma$. Distributions for two different values of anomalous couplings are shown. The anomalous contribution increases the cross section at high masses, while the decay diagrams contribute to the low end.

$$M_T(\gamma\mu;\nu) = \sqrt{(((m_{\gamma\mu}^2 + |\mathbf{E}_T^{\gamma} + \mathbf{E}_T^{\mu}|^2)^{\frac{1}{2}} + \not{E}_T)^2 - |\mathbf{E}_T^{\gamma} + \mathbf{E}_T^{\mu} + \not{\mathbf{E}}_T|^2)}$$

The cluster transverse mass is preferred over the invariant mass because the neutrino is not observed and the invariant mass cannot be known exactly. Figure 2.5 shows the ΔR distribution for the decay and production diagrams separtly. As previously mentioned, the decay diagram peaks at small separa-

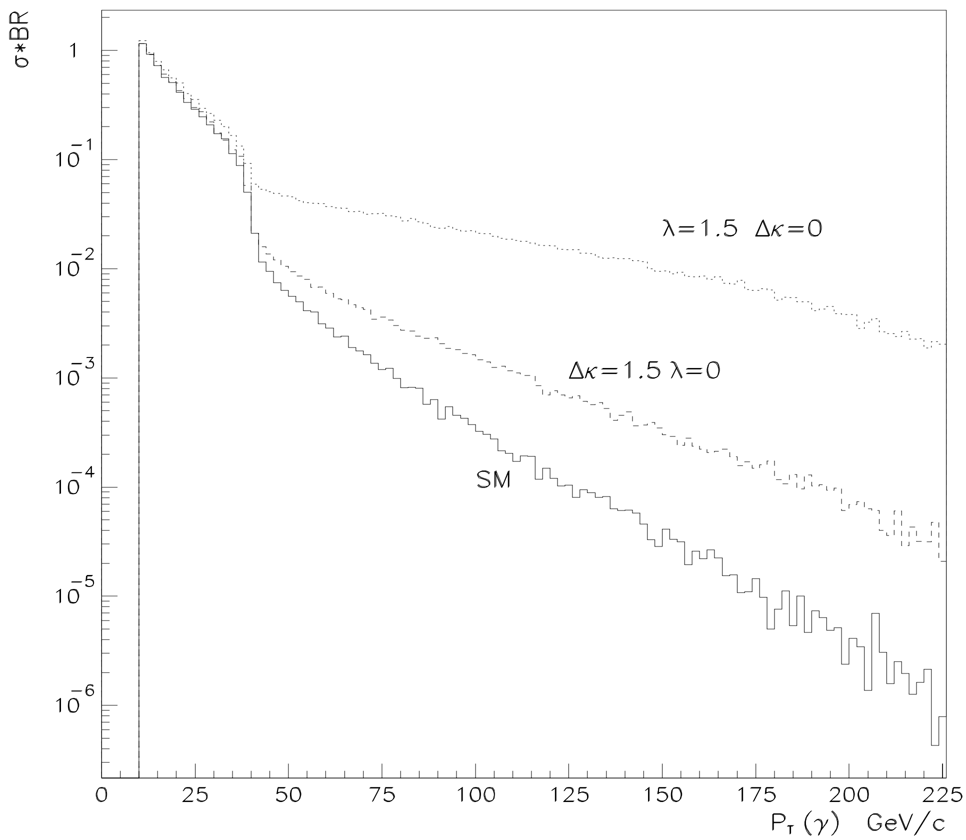

Figure 2.4: P_T of the $W\gamma$ system for the reaction $q\overline{q} \rightarrow W(\mu\nu)\gamma$. Distributions for the SM and for two different pairs of values of anomalous couplings are shown. One can see a large affect for higher p_T photons from anomalous couplings.

tions as one expects from *bremsstrahlung* and falls off rapidly as ΔR increases. The production diagrams produce larger ΔR separations, with a peak occuring at approximately π. This peak occurs since the W and the photon are produced mainly in the central region and back-to-back with high transverse momentum. As shown from the distribution, the ΔR cut of 0.7 has a very small effect on the production diagram and thus does not affect the sensitivity to the anomalous couplings.

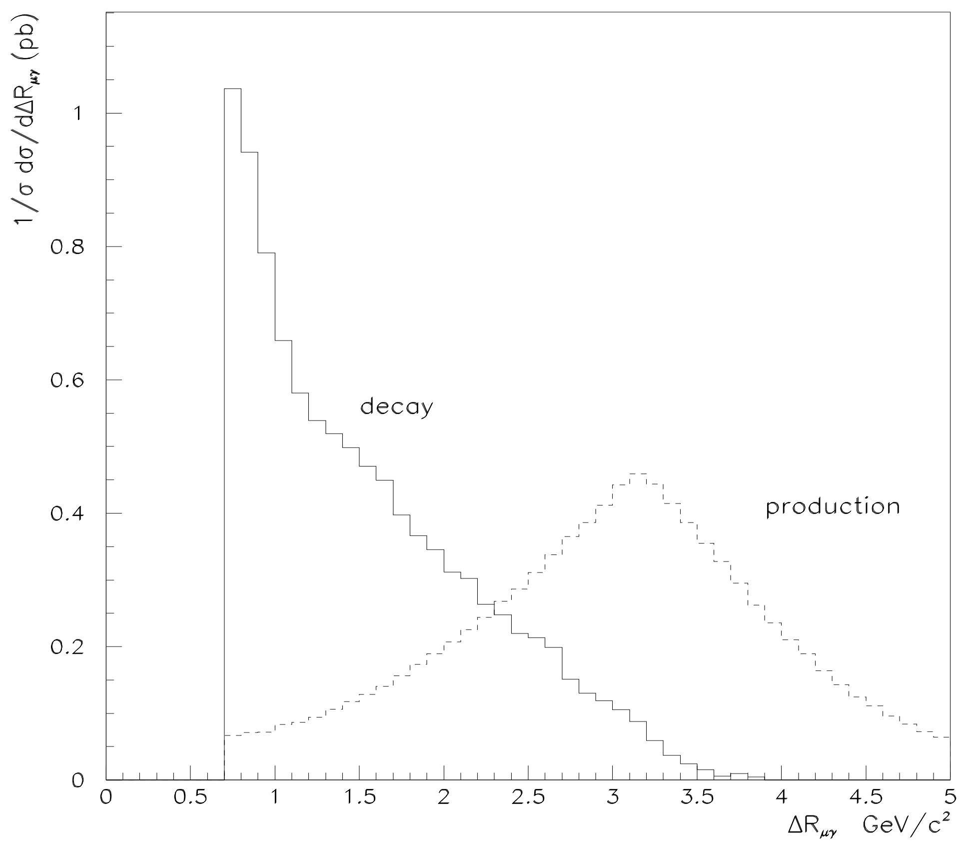

Figure 2.5: ΔR distribution for the decay and production diagrams. The cut of $\Delta R > 0.7$ greatly reduces the contribution from the decay diagram (which diverges as $\Delta R \rightarrow 0$) while having almost no effect for the production diagrams. The diagrams were separated by applying a cluster transverse mass cut of $M_T(\gamma\mu;\nu) > 90$ GeV/c^2 for the production diagrams and $M_T(\gamma\mu;\nu) <$ 90GeV/c^2 for the decay diagrams.

One more interesting feature of $W\gamma$ production is the characteristic called the *radiation zero*. Details about the *radiation zero* can be found in [12, 13, 14]. Due to the interference between the different diagrams, the $W\gamma$ differential cross section vanishes at a particular point in phase space. This point called the *radiation zero*, occurs at the value of $cos\theta^* = -1/3(+1/3)$ for $W^+(W^-)$. θ^* is the scattering angle of the photon relative to the quark direction in the $W\gamma$ center-of-mass frame. It is the presence of the trilinear diagram that causes the destructive interference that produces the *radiation zero*. Observation of the *radiation zero* would be another direct test of the Standard Model. Figure 2.6 shows the effect of the radiation zero for the Standard Model case and for two anomalous couplings. One can see that the effect of the anomalous couplings is too fill in the zero.

In reality the *radiation zero* is somewhat washed out by various physics affects, making the observation non-trival. Since the neutrino is not detected, the longitudinal momentum can only be determined with a twofold ambiguity, thus causing the wrong solution to be picked some of the time. This causes the zero to be partially filled in. Also, the decay diagram does not contain a *radiation zero*; but most of these can be removed by making a cluster transverse mass cut as mentioned earlier. However, a fraction of the events from the decay diagram will still be present, thus causing the zero to be partially filled in. Furthermore, since the number of $W\gamma$ events is small, one needs to sum up the W^+ and W^- states, which causes the *radiation zero* to shift to $cos\theta^* = 0$. The last item that causes a partial filling of the *radiation zero* is the contribution

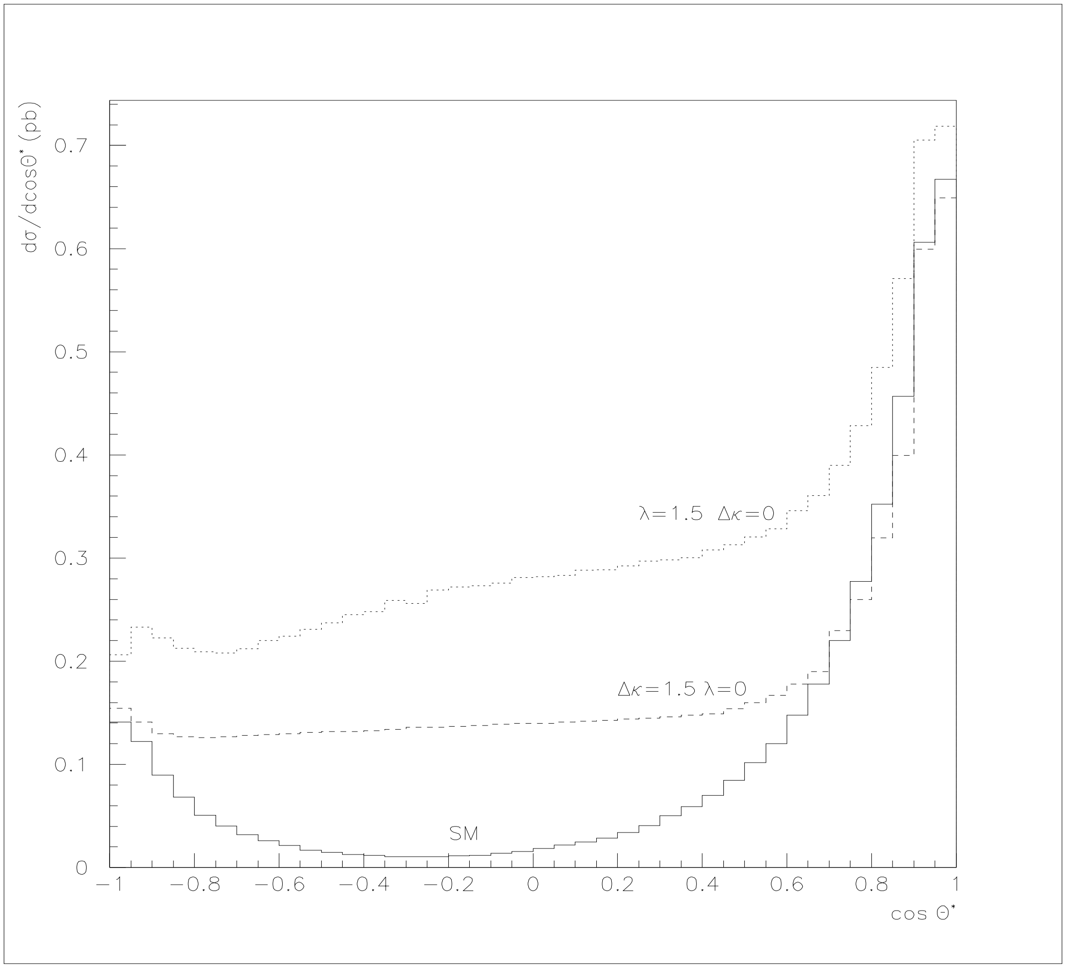

Figure 2.6: Distribution for W^+ in $cos\theta^*$, where θ^* is the scattering angle of the photon relative to the quark direction in the $W\gamma$ center-of-mass frame. The dip becomes filled in for anomalous couplings.

of higher order QCD processes [15]. Jets from higher order processes interfere with the destructive cancellation that cause the *radiation zero* and partially fill it in. The statistics gathered for DØ are not great enough to see the *radiation zero*.

2.4 Probing the $WW\gamma$ Vertex in Low Energy Experiments

As mentioned earlier, currently the only direct test of the $WW\gamma$ interaction is performed by studying the reaction $q\overline{q} \to W\gamma$. There are other indirect methods that can be made by low energy experiments. The low energy experiments are sensitive to the anomalous couplings, via loop corrections that arise in penguin type diagrams. But unlike the direct tests from high energy experiments, these results are sensitive to regularization schemes and loop cutoff parameters used in calculations [16]. This sensitivity makes the results model dependant and somewhat controversial.

The limits on the anomalous couplings from these indirect tests have a drastically different form from those obtained from the high energy experiments. From direct production experiments, the limits form closed contours in the same plane because the total cross section has a bilinear form for any given pair of couplings. On the contrary, the limits from indirect tests form bands that extend to infinity when both couplings are allowed to vary. If one coupling is fixed however, the limits can be very stringent.

The best limits from the low energy indirect studies come from the CLEO experiment [17]. This experiment studies the rare decay mode of $b \to s\gamma$. By measuring the cross section for this rare process, limits can be computed for $\Delta\kappa$ and λ. The 95% confidence level limits on $\Delta\kappa$ ($\lambda = 0$) are $-2.6 < \Delta\kappa < -1.2$ and $-0.6 < \Delta\kappa < 0.4$. Interference effects from the model exclude the region of $-1.2 < \Delta\kappa < -0.6$. The tightest limits on λ from indirect measurements come from a measurement [18] of the magnetic moment of the muon, giving $|\lambda| < 5$.

Chapter 3

Experimental Apparatus

This chapter provides a description of the DØ detector as well as an introduction to the Tevatron and a few relevant quantities related to collider physics. An 'official' reference for the detector as a whole can be found in [19].

3.1 Tevatron Collider

The DØ experiment studies collisions between protons and antiprotons in the Tevatron Collider at the Fermi National Accelerator Laboratory. To produce the highest center of mass energies in the world, the Tevatron runs in a collider mode with the beams of protons and antiprotons colliding with each other with an energy of 900 GeV to produce a center of mass energy of 1.8 TeV. A collider can produce higher center of mass energies because the available energy to create new particles is equal to $2 \times E_{beam}$ whereas for a fixed target experiment the available energy equals $\sqrt{2 \times E_{beam}}$. This high energy allows one to probe the shortest distances inside the proton and study the fundamental building blocks of nature. What follows is only a brief discussion of the Tevatron; a complete discussion can be found in other sources [24, 20, 22]. A schematic layout of the Tevatron and all the separate accelerators that are associated with the Tevatron ring is shown in Figure 3.1.

The Tevatron accelerator complex uses five steps to accelerate protons from rest to the peak energy of 900 GeV. The first stage is the Cockcroft-Walton accelerator. This device first adds electrons to hydrogen atoms then pulls these negative ions toward a positive voltage. The ions leave the Cockcroft-Walton with an energy of 750 KeV, about 30 times the energy supplied to electrons in a television picture tube. The ions are then feed into the Linac which uses oscillating electric fields to accelerate the ions to an energy of 400 MeV. At the end of the Linac the ions are passed through a carbon foil which strips the electrons leaving only the positive charged proton. Negative ions are used in the Linac because it makes the transfer to the booster much easier. Since the negative ions are oppositly charged compared to the protons in the booster; they can be bent together and merged into one beam in the booster.

The protons then enter the booster, a 500 meter circumference synchrotron which accelerates the protons to an energy of 8 GeV. Electric fields accelerate the protons while magnetic fields are used to keep the particles in a circular path. The beam of protons, which is also 'bunched' by these fields, circulates about 20,000 times before entering the main ring. The main ring is a much larger synchrotron (6.28 km circumference) that accelerates the protons to an

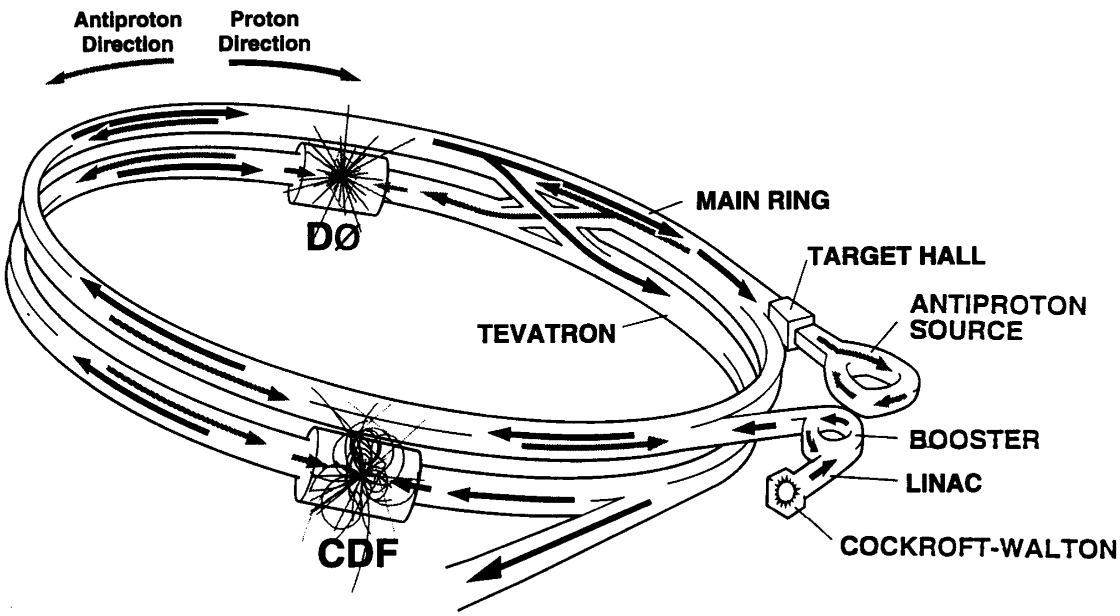

Figure 3.1: The Fermilab Tevatron Collider

energy of 150 GeV. In addition to accelerating rf cavities, it consists of 1000 conventional copper-coiled magnets that bend and focus the protons. The main ring has two major purposes; one is to feed the 150 GeV protons into the last accelerator, the Tevatron, and the other is to direct the protons onto a target to produce antiprotons.

Antiprotons are not easily produced; it takes many protons to produce an antiproton. The rate of antiprotons that are produced depend on the energy of the beam, and the size and composition of the target. The target used at Fermilab is a nickel target where it takes about 100,000 protons to produce one antiproton. The antiprotons are focused by lithium magnet lenses into the Debuncher which is a machine that collects the particles into a beam of equal energy using a technique known as stochastic cooling [21]. The antiprotons are then stored in the Accumulator until a sufficient amount of them have been produced at which time they are then injected back into the main ring and accelerated to 150 GeV.

The final stage is the Tevatron synchrotron which occupies the same tunnel as the main ring. The Tevatron magnets contain superconducting wire which must be cooled down to a temperature of -450 deg F by liquid helium. The superconducting magnets are necessary to produce the large magnetic fields required to bend protons with an energy of 900 GeV. The Tevatron can be operated in one of two major modes. In fixed target mode, the Tevatron is filled with protons that are directed toward experimental areas about once per minute. In collider mode, the Tevatron is filled with six bunches of protons and six bunches of antiprotons, travelling in opposite directions. The beams are typically kept colliding for about 20 hours after which the machine is emptied and injected with a new supply of protons and antiprotons.

3.2 Luminosity and Cross Sections

The term luminosity ($\mathcal{L}$) which is the interaction rate per unit cross section is often used to to describe the performance of a collider. The luminosity is given by the following formula:

$$\mathcal{L} = \frac{N_p N_{\bar{p}}}{\tau A} \tag{3.1}$$

where N_p and $N_{\bar{p}}$ denote the number of protons and antiprotons in a bunch,

τ is the time between collisions, and A is the geometrical area of the interaction point. Luminosities are typically measured in units of cm^{-2}s^{-1}, while cross sections (σ) are measured in *barns*, where 1 barn = $10^{-24}cm^2$. The luminosity at the Tevatron during run 1B typically was in the range $5 - 20\times10^{30}$cm^{-2}s^{-1}. The number of events produced in a given time period for a specific process is given by integrating the luminosity with respect to time:

$$N = \sigma \int \mathcal{L}dt. \tag{3.2}$$

The inelastic cross section for $\overline{p}p$ interactions at $\sqrt{s}$ = 1.8 TeV is about 48.2 millibarns so on the order of one million collisions a second occur at the peak luminosity of 20×10^{30} cm^{-2}s^{-1}. The quantity $\int \mathcal{L}dt$ is called the integrated luminosity; the total integrated luminosity for run 1B was almost 90 pb^{-1}. The luminosity is determined by measuring the rate of inelastic $\overline{p}p$ interactions and dividing by the cross section [25]. Measuring the luminosity is important for many physics analyses where the cross section is to be determined.

3.3 Coordinate Systems

A right-handed coordinate system is used with the positive z-axis aligned along the beam in the direction of the protons and the positive y-axis pointing up. Both cylindrical (r, ϕ, z) and spherical (r, θ, ϕ) coordinates are used with $\phi = \pi/2$ being parallel to the positive y-axis, and $\theta = 0$ coincident with the positive z-axis. Instead of θ, it is often convenient to use the pseudorapidity η

defined as

$$\eta = -\ln \tan(\theta/2) \tag{3.3}$$

The pseudorapidity is equal to the rapidity,

$$y = 1/2\ ln \frac{E + p_z}{E - p_z} \tag{3.4}$$

in the limit that $m \ll E$ (m is the invariant mass $m^2 = E^2 - p^2$).

It is also convenient to use instead of momentum, 'transverse momentum', which is the momentum vector projected onto the plane perpendicular to the beam axis. The same definition can also be applied to the energy giving 'transverse energy'. These quantities are useful in $\overline{p}p$ collisions since the momentum of the partons along the beam is not known due to particles escaping down the beam pipe.

3.4 The DØ Detector

The DØ detector surrounds the DØ interaction region on the Tevatron ring. It is a general all purpose detector that weighs 5500 tons and stands 40 feet tall; a picture of the entire detector is shown in Figure 3.2. The DØ detector was designed to meet the following goals:

- identification and good energy resolution for electrons and photons
- large muon coverage

- identification and good energy measurement of parton jets

- measurement of missing transverse energy for a signature of neutrinos

To achieve these goals the DØ detector is separated into three separate sections: tracking, calorimetry, and muon detection. The layout of these systems is dictated by the physics of how the particles interact with matter. The tracking system is the innermost detector and measures and reconstructs three-dimensional tracks of charged particles. Next is the calorimeter which measures the energy of both neutral and charged particles. The calorimeter should have a large number of radiation lengths so all particles (except muons and neutrinos) are absorbed while the tracking system should contain as little material as possible to minimize multiple scattering and losses prior to the calorimeter. Finally the muon system covers the outside of the detector. The muon system consists of a magnetic iron toroid plus muon chambers. By bending the muon with the toroid and using the hits from the muon chambers the muon momentum can be determined by reconstructing the track.

3.5 Tracking System

The purpose of the tracking system is to measure with high precision the position of charged particle tracks and to determine the z position of the interaction vertex. The presence of a charged track which points to an electromagnetic cluster distinguishes electrons from photons. A track also measures the tra-

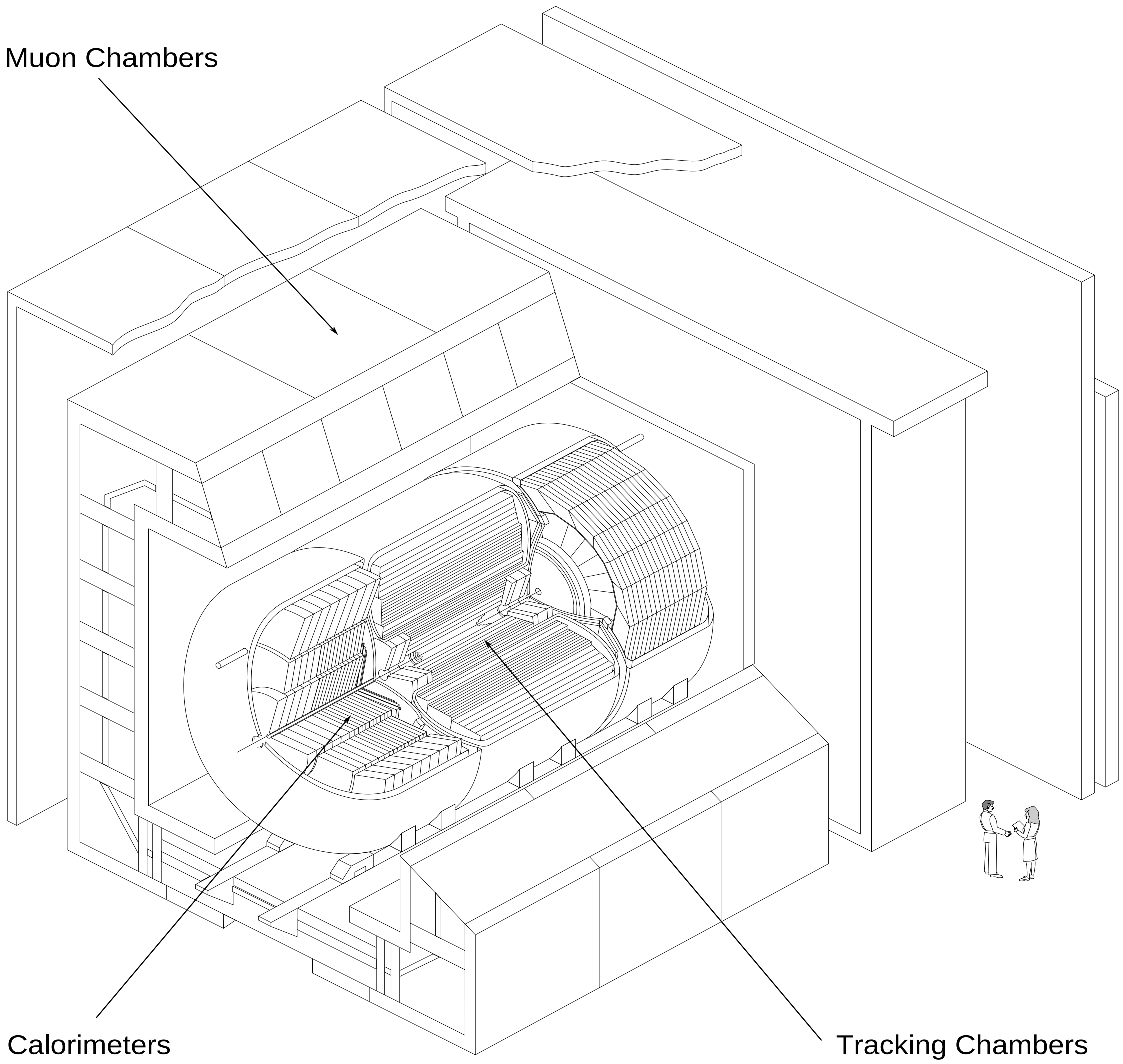

Figure 3.2: Cutaway view of the DØ detector

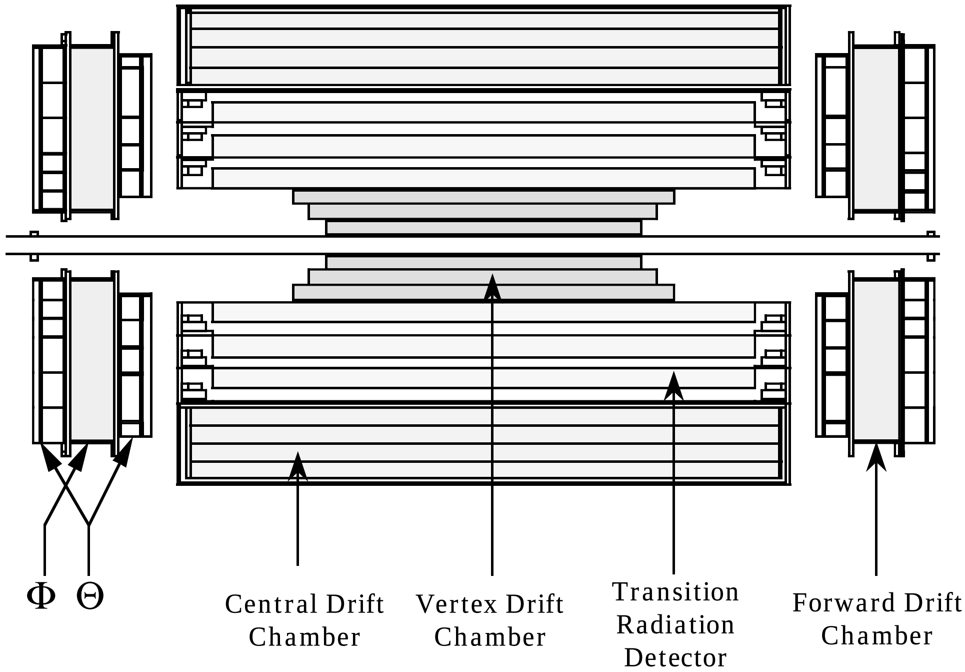

Figure 3.3: The DØ tracking system.

jectory of muons which helps in the identification of that particle. Additional information such as the number of tracks in a road and the ionizing energy along a track (dE/dx) help in distinguishing between electrons and converted photons coming from π^0's. The DØ tracking system, shown in Figure 3.3, consists of four separate detectors. The innermost detector is the Vertex Detector (VTX) which is used to determine the vertex of the event. Following that is the Transition Radiation Detector (TRD) which is used to discriminate between electrons and pions. Furthest from the beam pipe are the Central Drift Chamber (CDC) and the Forward Drift Chamber (FDC). The tracking system covers the region out to $\pm$ 135 cm along the beam axis, from the interaction region, and radially from $r = 3.7$ cm to 78 cm.

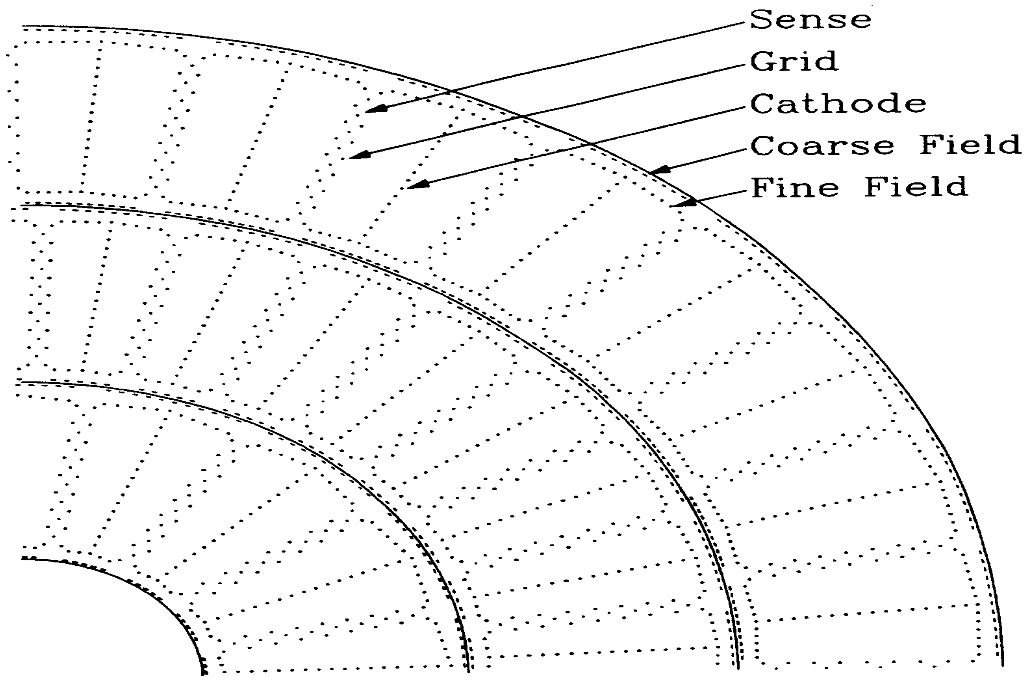

Figure 3.4: The DØ Vertex Detector.

3.5.1 Vertex Detector

The vertex detector (VTX), the innermost tracking detector, helps to determine the event vertex. A schematic of the VTX is shown in figure 3.4. The VTX also serves to compliment the other tracking detectors by reconstructing tracks and measuring dE/dx to help identify conversions which occur in the TRD.

The VTX consists of four carbon fiber cylinders enclosing 3 concentric layers of drift chambers. The important quantities of interest are shown in Table 3.1. As a charged particle passes through the gas in the drift chambers it ionizes the gas, creating electron/ion pairs along the path of the particle. The number of pairs produced depends on the energy of the particle and the type of gas [26]. An electric field is applied which causes the electrons to drift

Table 3.1: Vertex Drift Chamber Parameters

Parameter	**Specification**
Radius	3.7 cm - 16.2 cm
Overall Length	116.8 cm
Number of Layers	3
Number of Cells	16,32,32 (for Layers 1,2,3)
Number of Sense Wires	8 per cell (640 total)
Sense Wire Voltage	+2.5kV
Drift Field	1 kV/ cm
Gas Type	95% CO_2 + 5% ethane + 0.5% H_2O
Gas Pressure	1 atm
Gas Gain	4×10^4
Spatial Resolution	$r\phi \simeq 60\ \mu$m, $z \simeq 1.5$ cm

to a positive cathode while undergoing repeated collisions with the gas and generating further electrons. By measuring the time required to collect the electrons and knowing the drift velocity of the electrons in the gas, a position measurement can be made. In order to obtain a linear relationship between the distance and time, it is necessary that the electric field be made as constant as possible throughout the volume. One can also be aided by the fact that the relationship between the drift velocity and electric fields tends to flatten out for sufficiently large electric fields. Thus it is desirable to operate the drift chambers in this *saturation* region.

3.5.2 Transition Radiation Detector

The next tracking detector after the VTX is the Transition Radiation detector (TRD) [27]. When a charged particle passes through materials with different dielectric constants, it radiates photons in the forward direction. The intensity is proportional to the Lorentz factor, $\gamma = E/(mc^2)$, and is concentrated in a cone with an opening angle of $1/\gamma$. This characteristic allows one to discriminate particles which have similar energies but different masses. For DØ the discrimination is used to distinguish between electrons and pions, pions being the primary sources for fake electrons. The TRD consists of three layers of polypropylene radiator foils and an X-ray detector. The gaps between the radiator foils are filled with dry nitrogen. The X-ray detector consist of drift chambers filed with a gas consisting mostly of Xenon. The transition radiation photons ionize the gas in the drift chamber where the charge is collected on sense wires and read out. Some of the main parameters for the TRD are shown in Table 3.2.

Table 3.2: Transition Radiation Detector Parameters

Parameter	**Specification**
Radius	17.6 cm - 47 cm
Overall Length	165 cm
Number of Layers	3
Number of Sense Wires	256 per layer
Sense Wire Voltage	+1.6 kV
Drift Field	0.7 kV/cm
Gas Type	Radiation Chamber - N_2
	Gap - CO_2
	Drift Chamber - 95% Xe + 7% CH_4 + 2% C_2H_6
X-ray energy	$<$ 30 keV

3.5.3 Central and Forward Drift Chambers

The Central Drift Chamber (CDC) and the Forward Drift Chamber (FDC) [28] operate on the same principle as the VTX. Charged particles passing through a gas liberate electrons which are collected on sense wires. The CDC is the outermost tracker in the central region and has a pseudorapidity coverage of $\mid \eta \mid \leq 1.2$. The FDC extends the coverage of the CDC and continues down to a pseudorapidity of $\eta \approx 3.1$. The CDC and the FDC provide track reconstruction and dE/dx measurement for discriminating electrons from converted photons. The CDC consists of 4 concentric rings of 32 azimuthal cells per ring (shown in Figure 3.5); adjacent cells are staggered in ϕ by one half cell to improve pattern recognition. The FDC consists of 2 separate sets of the disks, two subdivided in θ and one sandwiched between (see Figure 3.6). The primary parameters for both the CDC and the CDC and the FDC are shown in Table 3.3.

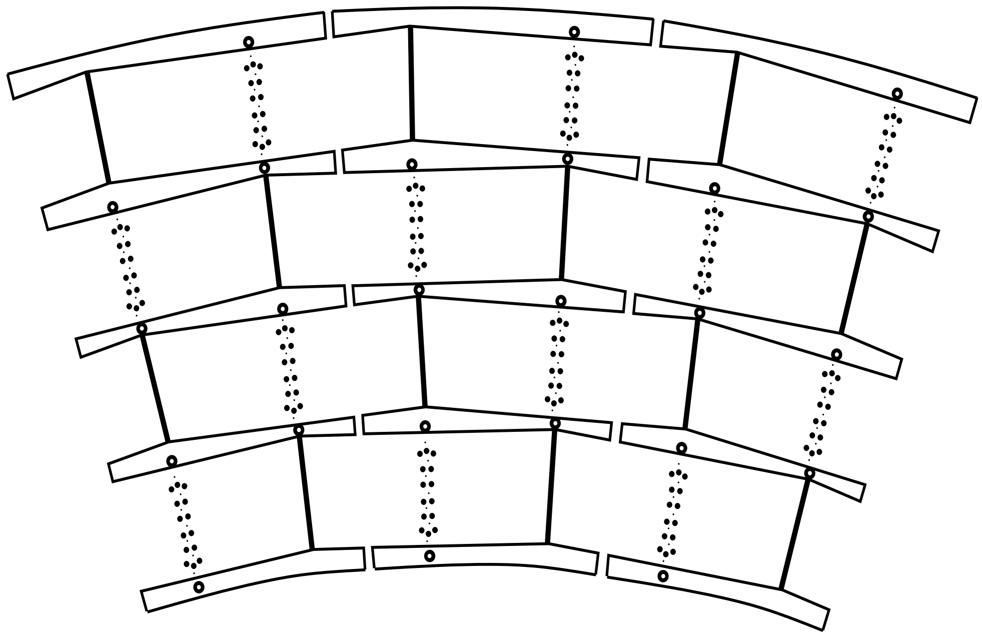

Figure 3.5: End view of the CDC.

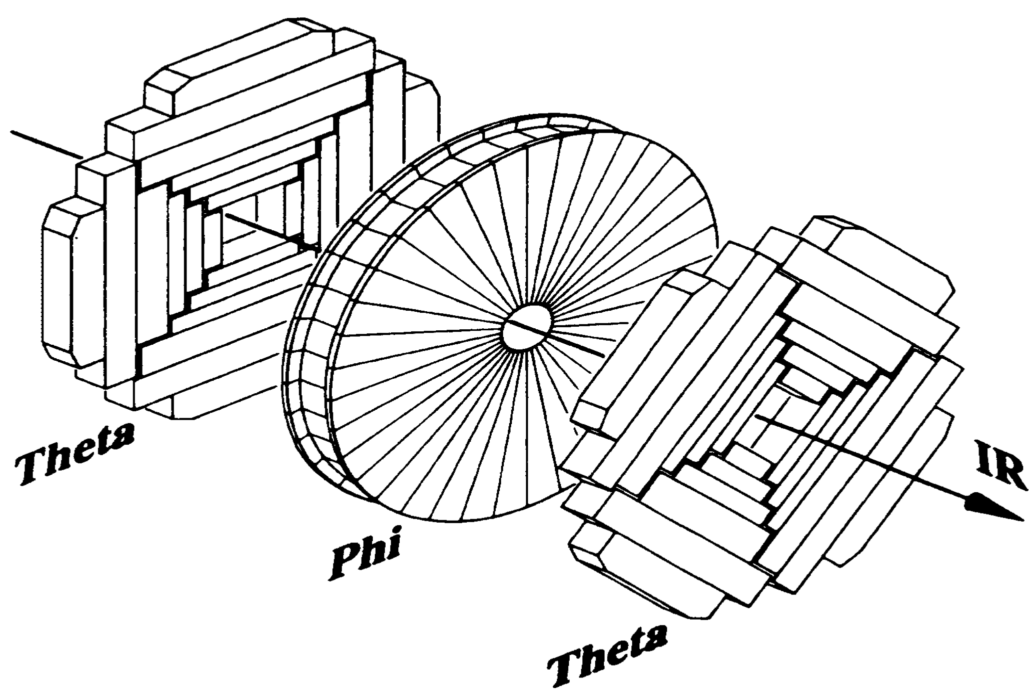

Figure 3.6: FDC, exploded view.

Table 3.3: Parameters of the DØ CDC and the FDC

	CDC	**FDC**
Radius	51.8 cm - 71.9 cm	11 cm - 62 cm
Overall Length	179.4 cm	$z = \pm$(104.8 cm - 135.2 cm)
Number of Layers	4	6 (4 Θ, 2 Φ)
Number of Cells	32 per layer	24 in each Θ module 36 in each Φ module
Number of Sense Wires	7 per cell (896 total)	8 per cell in each Θ module 16 per cell in each Φ module
Sense Wire Voltage	+1.45 kV (inner sense wires) +1.58 kV (outer sense wires)	+1.55 kV Θ modules +1.66 kV Φ modules
Drift Field	620 V/cm	1 kV/cm
Drift Velocity	34 μm/ns	40 μm/ns Θ modules 37 μm/ns Φ modules
Gas Type	93% Ar + 4% CH_4 + 3% CO_2 + 0.5% H_2O	same
Gas Gain	2×10^4 (inner sense wires) 6×10^4 (outer sense wires)	2.3×10^4 inner Θ sense wires 5.3×10^4 outer Θ sense wires
Spatial Resolution	$r\phi \simeq 180$ μm, $z \simeq 2.9$ mm	$\theta \simeq 300$ μm, $\phi \simeq 200$ μm

3.6 Calorimeter

The purpose of the calorimeter is to measure the energy of particles by absorbing them and sampling the deposited energy. Since DØ has no central magnetic field this is the only method available to determine the energy of particles except for muons which will pass through the outer toroid. For hadrons and electrons at high energies, this calorimetric measurement is more accurate than that which can be attained by a central solenoid field. Detailed discussions on calorimetry in high energy physics can be found in [29].

3.6.1 Calorimetry Principles

The discussion of calorimetry can be broken into two main sections, covering electromagnetic calorimetry and hadronic calorimetry. The two particles involved in electromagnetic calorimetry are the electron and the photon. When a high energy electron ($\gg 10$ MeV) passes through a material with a high atomic number, the main mechanism for energy loss is through Bremsstrahlung, a process where the electron interacts with the coulomb field of the nucleus and emits a photon. A high energy photon passing though material will interact primarily though pair production, producing an electron- positron pair in the vicinity of a nucleus. Thus an electron or photon will create a shower of secondary particles that will grow until the secondary particles do not have enough energy to produce further particles. The rate at which a particle looses energy is constant for a given material, and is given as the *radiation length* X_0:

$$\frac{dE}{E} = -\frac{dx}{X_0} \tag{3.5}$$

An example of a typical value, the radiation length for uranium, the material used in DØ , is about 3.2 mm.

The second type of calorimetry is hadronic calorimetry. Hadronic particles also create showers but with much different characteristics. At high energies, hadrons loose energy primarily through inelastic collisions with atomic nuclei. The collisions produce secondary hadrons which can in turn undergo inelastic collisions thus creating a hadronic shower. The length of the shower is paramatized by the nuclear interaction length, λ. For uranium, which is used in the DØ calorimeter, $\lambda = 10.5$ cm. As shown by the difference between the values of X_0 and λ, hadronic showers are less compact than electromagnetic showers and are extended in space.

To measure the energy of the showers, DØ uses a sampling calorimeter. A sampling calorimeter uses interleave layers of a dense, inert absorber, surrounded with an active medium which is sensitive to particles passing through it. Most of the energy is absorbed in the inert material; thus only a fraction of the energy can be detected. This fraction, called the sampling fraction, results from a statistical process; and variations in the energy sampled degrade the energy resolution of a calorimeter.

One important parameter of a calorimeter is the *e/π ratio*, the ratio of the response of the calorimeter to electrons and to pions. It is desirable to have this number as close to one as possible for the following reason. A hadronic shower will include hadronic as well as electromagnetic components made from π^0 and η decays. The fraction of electromagnetic energy in a hadronic shower can contain large fluctuations, but if $e/\pi \approx 1$ then these fluctuations will not change the energy resolution. This quality of a calorimeter is called compensation.

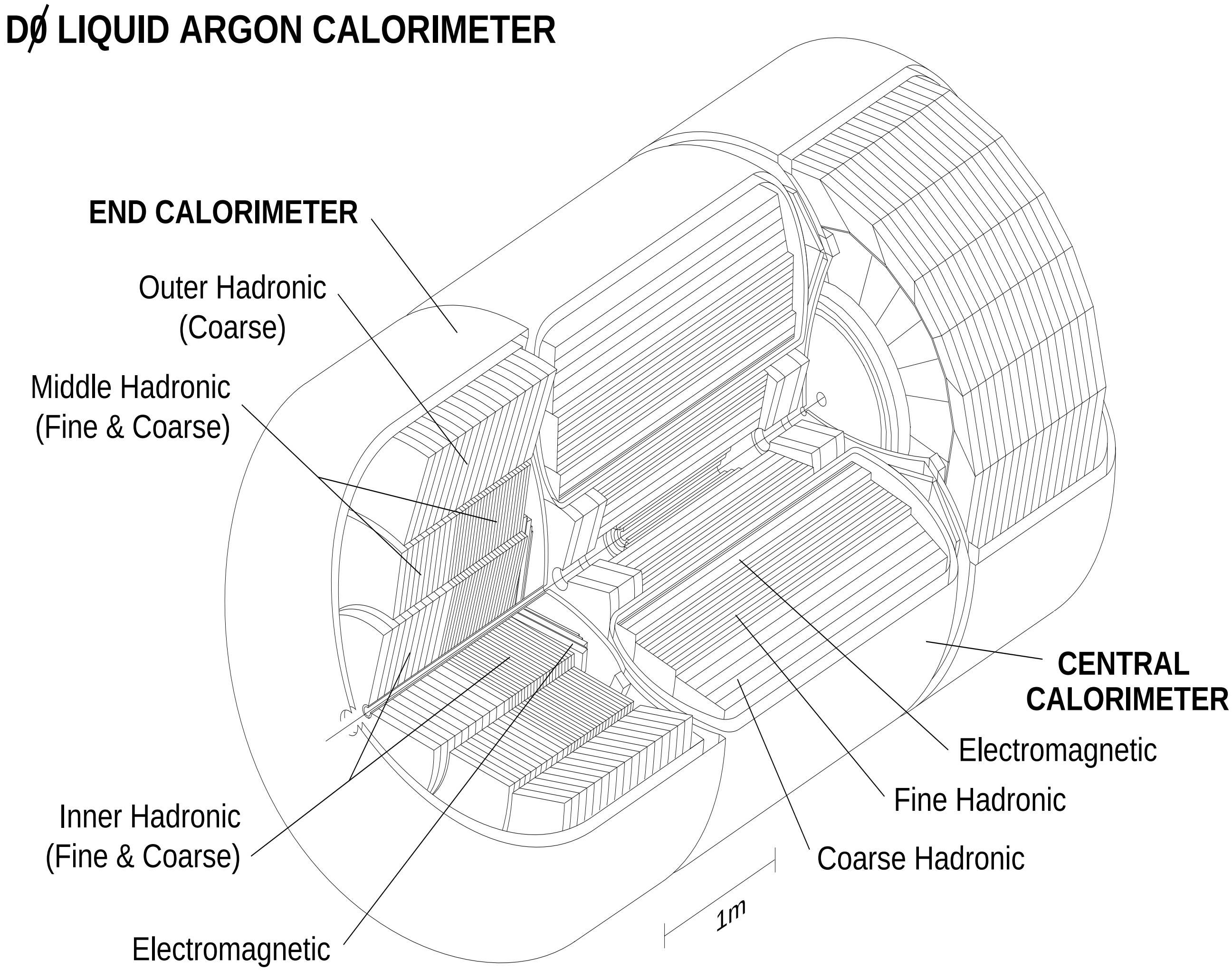

Figure 3.7: The DØ calorimetry, consisting of the Central Calorimeter with two End Calorimeters. The Inter-Cryostat Detector is mounted on the face of each End Calorimeter.

3.6.2 The DØ Calorimeter

The DØ calorimeter contains three sections, a central calorimeter (CC) and two endcap calorimeters (EC) both of which have electromagnetic and hadronic sections. A schematic of the DØ calorimeter is shown in Figure 3.7.

3.6.3 Central and Endcap Calorimeter

The Central Calorimeter (CC) has a length of 2.6 m and covers a range of pseudorapidity of $|\eta| \leq 1.2$. The CC is made up of three sections, an electromagnetic calorimeter (EM) with four layers, a fine hadronic calorimeter (FH), with three layers, and a single layer coarse hadronic (CH) calorimeter. Details of the CC are listed in Table 3.4. For the EM and FH calorimeters, depleted uranium is used as an absorber while stainless steel is used for the CH. Liquid argon is used as the active medium for all the DØ calorimeters.

Table 3.4: Parameters of the DØ Central Calorimeter

Section	**EM**	**FH**	**CH**
Pseudorapidity Coverage (η)	± 1.2	± 1.0	± 0.6
Absorber Material	U	U (1.7% Nb)	Cu
Absorber Thickness (mm)	2.3	2.3	46.5
Number of Readout Layers	4	3	1
Depth per Readout Layer	2, 2, 7, 10 X_0 (0.76 λ_a)	1.3, 1.0, 0.9 λ_a	3.2 λ_a
Total Radiation Lengths (X_0)	21	96	33
Total Nuc. Abs. Lengths (λ_a)	0.76	3.2	3.2
Sampling Fraction	11.79%	6.79%	1.45%
Segmentation ($\Delta\eta \times \Delta\phi$)	0.1×0.1 (Layers 1,2,4) 0.05×0.05 (Layer 3)	0.1×0.1	0.1×0.1
Total Number of Channels	10,368	3000	1224

The Endcap Calorimeters (EC) provide detection in the forward region in the interval $1.1 \leq \mid \eta \mid \leq 4.5$. As with the CC, the EC contains three sections, the EM, FH, and the CH. The FH is broken into the inner fine hadronic (IFH) and the middle fine hadronic (MFH), and the CH is broken into the inner coarse hadronic (ICH) and the outer coarse hadronic (OCH). The pseudorapidity coverage of the electromagnetic portion of the EC covers the interval $1.5 \leq \mid \eta \mid \leq 2.5$. Together with the CC, the DØ calorimeter system is almost completely hermetic and gives an accurate measure of the missing transverse energy. Details of the EC are listed in Table 3.5.

Table 3.5: Parameters of the DØ Endcap Calorimeters

Section	**ECEM**	**IFH**	**ICH**
Pseudorapidity Range (η)	$\pm$ (1.3–4.1)	$\pm$ (1.6–4.5)	$\pm$ (2.0–4.5)
Absorber Material	U	U (1.7% Nb)	Steel
Absorber Thickness (mm)	4.0	6.0	46.5
Number of Readout Layers	4	4	1
Total Depth	20 X_0 (0.95 λ_a)	4.4 λ_a	4.1 λ_a
Sampling Fraction	11.9%	5.7%	1.5%
Total Number of Channels	7488	4288	928
Section	**MFH**	**MCH**	**OH**
Pseudorapidity Range (η)	$\pm$ (1.0–1.7)	$\pm$ (1.3–1.9)	$\pm$ (0.7–1.4)
Absorber Material	U (1.7% Nb)	Steel	Steel
Absorber Thickness (mm)	6.0	46.5	46.5
Number of Readout Layers	4	1	3
Total Depth	3.6 λ_a	4.4 λ_a	4.4 λ_a
Sampling Fraction	6.7%	1.6%	1.6%
Total Number of Channels	1856	384	960

3.6.4 Intercryostat Detector (ICD) and Massless Gap Detector

The region between the CC and the EC, $0.8 \leq | \eta | \leq 1.5$, contains mostly cryostat walls and support structures. This region is an area where the energy is not well measured. To correct for this, two additional calormetric devices were added. The ICD is mounted between the cryostat walls and consists of scintillator tiles readout by phototubes. The Massless Gaps are mounted onto the insides of the cryostats and consist of signal boards which collect the ionization energy deposited near the cryostat wall.

3.7 Muon System

The outermost part of the detector is the muon system. A muon does not interact strongly and is too massive ($\approx 200m_e$) to deposit much energy in an electromagnetic shower. Figure 3.8 shows the interaction length as a function on η for the DØ calorimeters and the muon system. As shown in the figure, the calorimeter contains many interaction lengths. Punchthrough is thus not a problem for DØ since hadronic showers are completely contained within the calorimeter. Thus any charged particle that escapes the calorimeter is likely to be a muon. The DØ muon system is shown in Figure 3.9.

The muon system consist of five magnetized iron toroids surrounded by three layers of proportional drift tubes (PDTs) [30]. The PDTs measure the

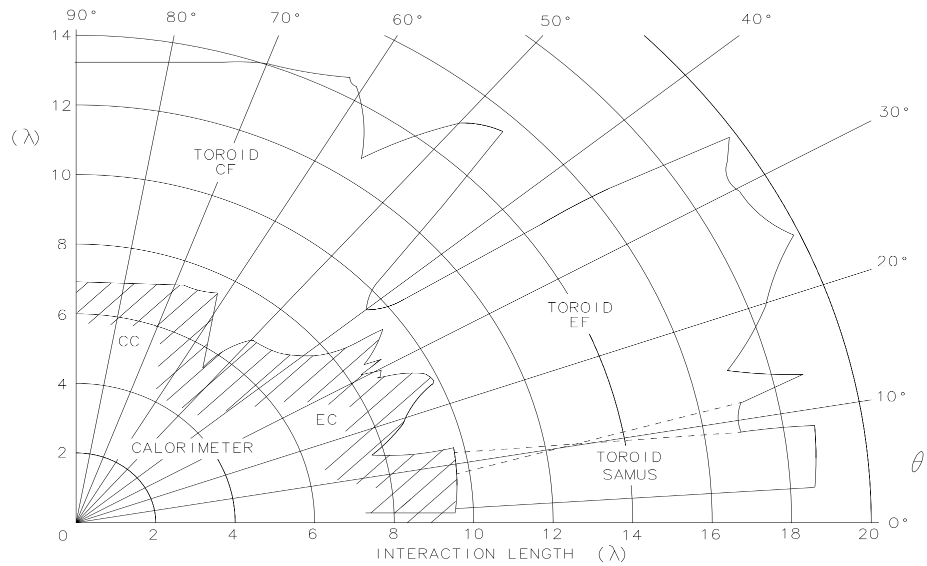

Figure 3.8: Interaction thickness of the DØ calorimeters and muon system as a function of η.

position of the muons before and after the iron toroids. Once this is done, a trajectory can be determined and thus the momentum of the muon can be measured. The first layer of PDTs are placed before the iron and the last two are positioned after the iron. When determining the momentum of the muon, the track obtained from the positions measured in the muon chambers is linked if possible to a track found in the central tracking system. The DØ muon system is divided into two sections, the WAMUS (wide angle muon system) and the SAMUS (small angle muon system), which are described in the following sections.

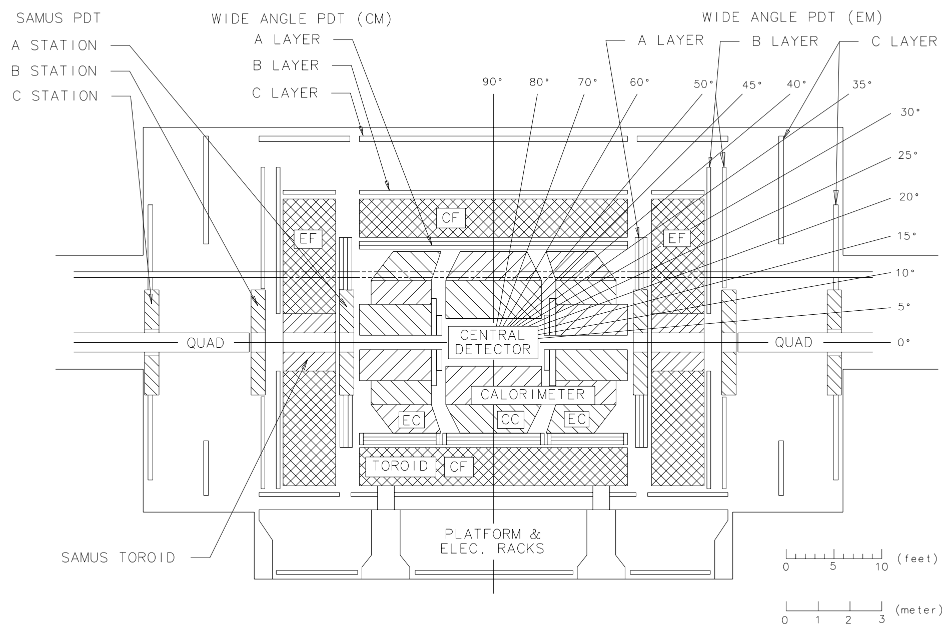

Figure 3.9: Side view of the DØ muon system.

3.7.1 WAMUS

The WAMUS System contains rectangular PDTs which have one sense wire per drift cell. The pure WAMUS region has an angular coverage of $|\ \eta\ | \leq 1.7$ For the three layers, A, B, and C (shown in Figure 3.9), there are respectively 4, 3, and 3 planes of drift cells. The front end electronics measures the arrival times of pulses at the end of each wire and the time difference between pulses arriving at the ends of each jumpered pair of wires. Using this time difference, a crude position measurement along the wire can be determined. A more precise measurement of the hit position is made using the vernier cathode pads in each tube. The muon creates an avalanche of electrons which induce pulses on the cathode pads. By measuring the ratio of the charge deposited on the inner and outer pads, a position measurement with about 3 mm accuracy can be made for the direction along the wire. The resolution obtained perpendicular to the sense wire (used for momentum determination) has an accuracy of about 0.53mm.

To measure the momentum of the muon, the trajectory is determined from the hits in the three layers. The momentum resolution depends not only on the accuracy of these position measurements but also on the multiple scattering in the iron, which smears the momentum direction coming out of the iron. A list of relevant parameters for the WAMUS as well as for the SAMUS is given in Table 3.6

3.7.2 SAMUS

The SAMUS muon system has a pseudorapidity range of $1.7 \leq | \eta | \leq 3.6$. Due to the higher particle densities in the forward region the SAMUS uses smaller drift tubes. The system consists of three stations each comprising of three drift tube planes. Each plane is composed of two subplanes, offset by half a tube diameter. The drift tubes are constructed from stainless steel tubes with a 3 cm diameter, each containing a single sense wire.

3.8 Trigger and Data Acquisition

The time between colliding bunches of protons and antiprotons in the Tevatron is 3.5 μsec, corresponding to 286,000 bunch crossing a second. The average

Table 3.6: Muon System Parameters

	WAMUS	SAMUS
Pseudorapidity Coverage (η)	± 1.7	$1.7 - 3.6$
Magnetic field	2 T	2 T
Nuclear interaction len	≈ 13.4	≈ 18.7
Number of modules	164	6
Number of drift cells	11,386	5308
Sense wire parameters	50μm Au-plated W, 300 g tension	50μm Au-plated W 208 g tension
maximum sagitta	0.6mm	2.4mm
Sense wire voltage	+4.56kV	+4.0kV
Cathode pad voltage	+2.3kV	+2.3kV
Gas composition	Ar 93%, CF_4 5%, CO_2 5%	CF_4 90% CH_4 10%
Bend view resolution	$\pm$ 0.53mm	$\pm$ 0.35mm
Non-bend view resolution	$\pm$ 3.0mm	$\pm$ 0.35mm
Average drift velocity	6.5cm/μs	9.7cm/μs

size of an event, the data digitized by the detector electronics for each interaction, is of the order 300 kilobytes. At an interaction rate in excess of 10^5 events/sec there would be far too much data to be recorded to tape. Most of the interaction rate derives from well studied processes and needs not be recorded, while the bulk of the interesting physics is quite rare. For these reasons, one needs to have a mechanism to be able to sift out the interesting events. This process is called triggering.

The difficult task of reducing the event rate by about a factor of 100,000 (200kHz to 2Hz) is accomplished in three trigger stages. The trigger system contains the required rejection but keeps high efficiency for the rare and interesting physics. For an event to make it into the data stream it must pass all levels of the trigger. The three stages of the triggering are called the Level 0, Level 1, and the Level 2 trigger. Each of these is described below.

3.8.1 Level 0

The Level 0 detector [31] performs two useful functions. First, it is the initial stage in the multi-stage system of triggering. It consists of two scintillator hodoscopes mounted on the inside faces of each of the EC cryostats, 140 cm from the center of the detector. The hodoscopes contain a checkerboard pattern of scintillators using long and short elements which are read out by photomultiplier tubes. If a minimum bias event occured (specifically, a coincidence of signals from both hodoscopes close in time to the bunch crossing), the Level 0 system would signal the Level 1 trigger to begin operation. The hodoscopes cover a pseudorapidity range of $1.9 <\mid \eta^{det} \mid< 4.3$.

The Level 0 detector also provides a measurement of the luminosity for the experiment. By measuring the rate for non-diffractive inelastic collisions and by knowing the inelastic cross section, the luminosity can be determined. As well as providing the luminosity, the Level 0 system provides information on the z-coordinate of the primary collision vertex by measuring accurately the time difference on the signals from the two hodoscopes. There are two measurements made for the z vertex, a 'fast vertex' and a 'slow vertex'. Both of these are performed quickly in hardware so the information can be used in the next level of triggering. Following the Level 0 trigger is the main hardware trigger, Level 1.

3.8.2 Level 1

The Level 1 trigger [32] is a special-purpose hardware trigger that provides roughly a rejection factor of about 1000 on the input data rate. The parts of the detector that are used in the Level 1 trigger are the Level 0 detector, the calorimeter, and the muon system. From these systems, triggering can be done for electrons, photons, jets, muons, and missing transverse energy. Most of all the trigger decisions made by the Level 1 system are done before the next beam crossing arrives; thus there is no deadtime associated with Level 1. A subset of the Level 1 trigger, the Level 1.5 trigger, is a more refined programmable hardware trigger which can incur some deadtime.

The calorimeter Level 1 trigger sums energy from towers of size 0.2×0.2 in $\eta - \phi$ space out to a pseudorapidity of 3.2. The trigger towers are subdivided longitudinally into the electromagnetic and hadronic trigger towers. The trigger data is derived from trigger pickoffs from the calorimeter BLS (Base Line Subtraction) cards. All the data are simultaneously flash digitized; all subsequent calculations are purely digital.

From the digitized data, a number of quantities can be calculated. The most relevant are:

- total electromagnetic energy
- total hadronic energy
- total scalar transverse energy

- missing tranverse energy

These quantities are compared with programmable thresholds to determine if the event is to be passed. Along with the global quantities shown above, the electromagnetic and hadronic energy are calculated for each tower and also compared with thresholds to see if the event satisfied the trigger. For example one can ask for 'one EM tower of 10 GeV in the central region'.

The muon trigger uses the pad latch outputs, where there is one bit for each tube, about 16,700 bits in total. The muon trigger divides the muon into 5 sections: CF, EF north and south, and SAMUS north and south. For each region the trigger looks for patterns of hits which are consistent with a muon coming from the interaction region.

In addition to the pure Level 1 muon trigger there is also a Level 1.5 muon trigger. This trigger uses tighter matches of tracks between the layers to make a rough momentum calculation. This calculation can take longer than the time needed for a pure Level 1 decision so some deadtime can incur when the Level 1.5 is used. Both single and dimuon triggers were used for DØ.

The calorimeter and muon trigger as well as the Level 0 detector feed into the global trigger framework. This is a hardware processor which is responsible for combining the results of all the individual Level 1 components to make a global decision. The primary input to the framework is 256 trigger terms. Each of these consist of a bit where each bit indicates a specific requirement. The 256 trigger terms are reduced to 32 Level 1 bits (specific triggers). Each trigger bit can be made from any combination of the existing trigger terms; a programmable prescale can also be included. Once the Level 1 trigger has been satisfied, a signal is sent to the Level 2 system and the data begins digitization.

3.8.3 Level 2 Data Acquisition System (DAQ)

The last stage in the three steps of triggering is the Level 2 data acquisition system [33]. The Level 2 trigger is made up of 48 VAXstation processors which run software filters using the entire data for an event. For this to happen all the data must be collected together. A general layout of the Level 2 DAQ system is show in Figure 3.10

Once the Level 1 trigger has fired, the detector front-end electronics begins the digitization process. This digitization occurs in VME crates which also contain a VME buffer/driver (VBD) card. Depending on the list of specific triggers fired, the appropriate data is digitized. The VME crates are doubled buffered so an event can be digitized while previous data is being transferred to the VBD. The VBD is also double buffered so it can be loading data from the digitizing electronics while an earlier event is being read out. The crates are divided into eight sections; each section outputs data on a high speed data cable, as described in the following section.

The DAQ system contains three control nodes: the supervisor, sequencer, and the surveyor. The supervisor controls the transferring of the data. When the supervisor receives a trigger from Level 1, it finds a free Level 2 node and

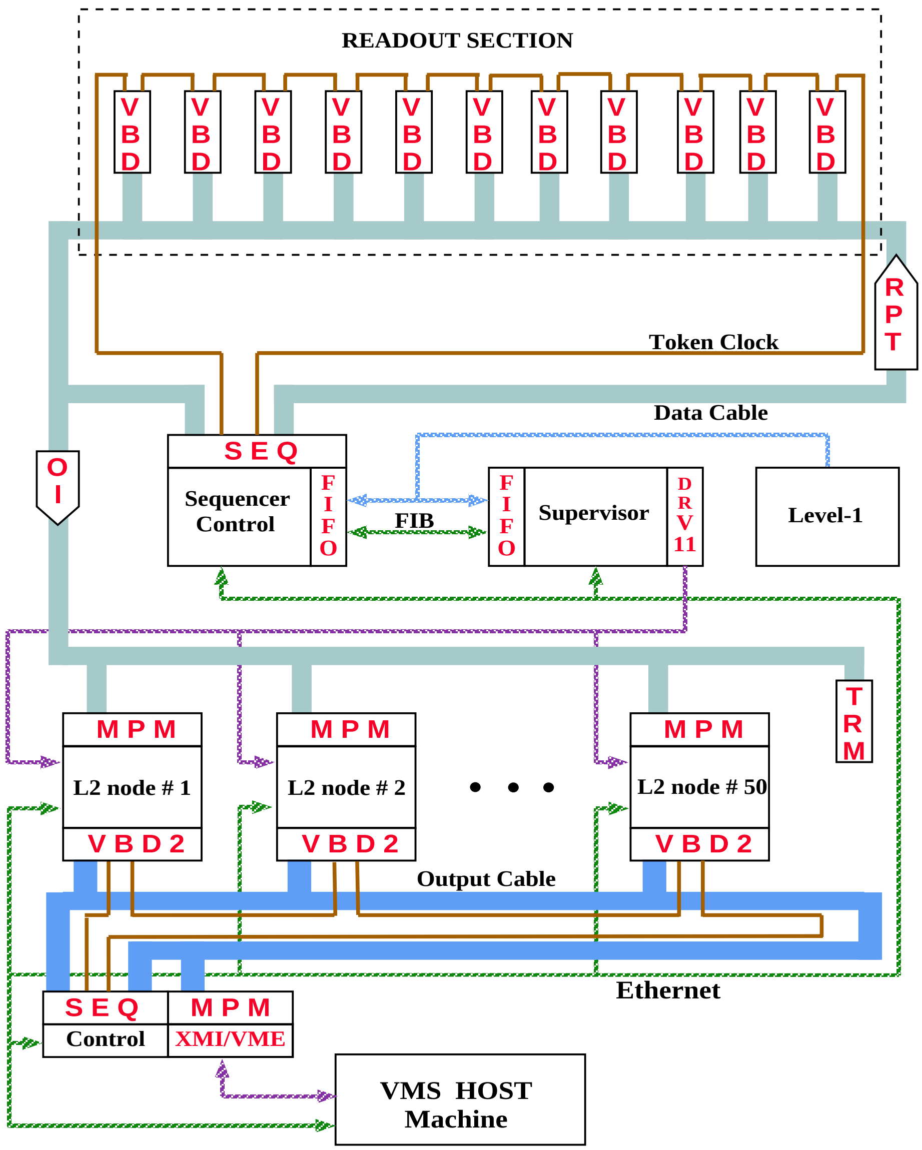

Figure 3.10: Overview of the DAQ system.

enables its mulit-port-memory(MPM) to take data. It then sends a signal to the sequencer to begin circulating tokens on the data cable. Each token, which includes the event number as well as a VME crate list, circulates on all the VME crates that are assigned to a specific data cable. A VBD will transfer its data onto the data cable when the token is present at the VME crate and when the event number in its data block matches that in the token. Once all the VBD's have transferred their data into the MPM's of the selected Level 2 node, a data structure header (Zebra) is added to the data. The surveyor performs monitoring of the system, keeping information that is useful for keeping track of system performance and for debugging problems. The supervisor, sequencer, and the surveyor all have a program that is sitting in memory that controls what operations are performed. These programs are written in VAXELN Pascal, a real time interrupt driven language.

The Level 2 nodes contain two types of software, the filtering software, and the framework software. The filtering software is similar to the reconstruction software that turns the raw data into physics objects that can then be studied. The algorithms are similiar to the offline reconstruction programs but are somewhat stripped down to maximize their speed. The software that controls the Level 2 system is known as the framework; this controls the data flow and contains the data format which determines if events are saved or not. Similar to the Level 1 trigger bits, the Level 2 framework contains 128 filter bits. Each Level 1 bit has an associated Level 2 filter script, which in turn calls the filter tools to perform the filtering. For each script that passes, a bit is set in the

128 bit mask of filter bits. If any bits are set, the event is sent to the host and saved on tape.

Chapter 4

Reconstruction and Particle ID

The data from the $\overline{p}p$ collisions are in an extremely raw format and obviously can not be used in this form. These data are at the level of ADC counts from tracking chambers, digitized signals from calorimeter cells, raw hit and time information from the muon chambers, etc. These quantities are by themselves not interesting in the physics sense and must be converted into physics quantities that relate to the particles coming from the $\overline{p}p$ collision. The process that performs this pattern recognition and calculates the relevant kinematic parameters is known as reconstruction. The program that DØ uses for reconstruction is called D0RECO and is run on a 'farm' of processors dedicated to this task.

4.1 D0RECO

The D0RECO program performs the basic reconstruction that is needed to start analyzing the data. In addition to reconstructing the data the program also reduces the size of the data by a considerable fraction. This is necessary because of the extremely large amount of data that was taken over the course of the run. From the raw data, D0RECO creates three types of data of decreasing size: STA's, DST's, and μDST's. Depending on the amount of detail one requires and the type of study that is being performed, one of the above types of data is used. The reconstruction can be broken up into five main categories, vertexing and tracking, electron/photon identification, muon identification, jet identification, and calculation of missing transverse energy. These categories are described below.

4.1.1 Vertexing and Tracking

The knowledge of the z-position of the interaction vertex is a useful quantity for doing physics analysis. Other quantities such as the transverse energy, transverse momentum, and missing transverse energy depend on the location of the interaction vertex. The x and y positions of the vertex are accurately known since the dimensions of the beam in that direction are very small (of order $50\mu m$) and are constantly maintained, in order to maximize the luminosity. The z-position of the interaction is much less constrained; the beam intensity forms a gaussian distribution with a mean of about 30cm. we describe below the procedure for determining the vertex position from the Central Drift Chamber (CDC) measurements.

- Hit finding: The raw digitized data of charge verses time is converted into a pulse; the total charge of the pulse is integrated to calculate dE/dx and the time arrival of the pulse is used to determine the position of the reconstructed hit.

- Tracking: The reconstructed hits in a given layer are joined to produce track segments for each layer. These segments are then matched between the layers to form tracks, all of which are saved.

- All the CDC tracks are projected back to the center of the detector and for each track the impact parameter (shortest distance between track and the z-axis) is calculated. Tracks with an impact parameter larger than some value are thrown out.

- Each track is projected into the (r,z) plane and the z-axis intersection is computed and entered into a histogram.

- A gaussian is fitted to the peak with the mean being the z-position of the vertex. Secondary vertices are searched for around the initial peak.

This method produces a resolution of about 2-3 cm in the vertex position, and multiple vertices can be separated if they are at least 8 cm apart. More information about the central detector hit finding and tracking can be found in [34, 35].

4.1.2 Electron/Photon Reconstruction

Electrons and photons are identified as producing localized deposits of energy in the electromagnetic calorimeter. The reconstruction performs the following steps:

- The EM towers are ordered from the highest to lowest in transverse energy. To reduce noise, the towers must have a minimum E_T of 50 MeV to be included in the list.

- Using a 'nearest neighbor' algorithm [36] and starting with the highest E_T tower, clusters are formed by adding the closest tower with the highest E_T.

- The centroid of the cluster is computed by using the cells in the third electromagnetic layer [37]. The position is found by using the log-weighted center-of-gravity of the energies. The position resolution achieved with these procedures is about 1.5–2 mm.

- For a localized energy deposit to be considered 'electromagnetic' (produced by either an electron or a photon), at least 90% of the total energy of the cluster must be in the electromagnetic calorimeter, and at least 40% of its total energy (including both the hadronic and the electromagnetic energy) must be in a single tower.

- For an electron identification to be associated with a localized deposit of energy, a central detector track is required to be within a road of

$\Delta\eta = \pm 0.1$, $\Delta\phi = \pm 0.1$. If a track is not found with this criteria, the particle producing the EM cluster is identified as a photon.

4.1.3 Muon Reconstruction

The muon reconstruction is somewhat similar to the CDC reconstruction. The following items are performed in the D0RECO program:

- The muon timing information is used to determine the position of the hits in the muon system; in each of the three layers (B, C outside the toroid and A, inside).
- The hits from these three layers are used to form tracks in the muon system.
- A global fit for the best measured parameters is performed using the muon system tracks, the interaction vertex, energy deposition in the calorimeter, and a track from the CDC (FDC) if one is present [38, 39]. Additional corrections are made for the effects of multiple scattering in the calorimeter and the iron toroid and for the expected energy loss from ionization in the calorimeter.

4.1.4 Jet Reconstruction

The jet reconstruction uses the electromagnetic and hadronic calorimeters to find and reconstruct jets. When a quark or gluon is produced it does not remain free, but hadronizes into colorless particles. These particles will appear as a 'jet' in a cone around the original direction of motion of the parent particle. The most common definition of a jet at DØ is that defined by the cone algorithm [40]. The following items describe the jet cone algorithm:

- Preclustering: Calorimeter towers are sorted in E_T and seed clusters are formed from the towers with largest E_T. Looping over towers, a precluster is formed from all neighboring towers within $|\Delta\eta| < 0.3$, $|\Delta\phi| < 0.3$ with $E_T >$ 1GeV.

- Cone Clustering: A new cluster is defined around the axis of the precluster with all calorimeter cells added to it in a given radius of η, ϕ. The centroid of this cluster is computed and the process is continued until the centroid stabilizes.

- Merging: After clustering, some cells can be assigned to more than one jet. If the fraction of the cells shared between two jets is greater than 50% the jets are merged together and the jet axis is recalculated.

A jet is also required to have at least an E_T of 8 GeV. In the analysis presented here, jets were reconstructed with the cone algorithm of radius $R = 0.5$.

Jet Energy Corrections

The reconstructed jet energy needs to be corrected for inefficiencies in the calorimeter and various physics effects. Due to the fact that jets are extended in space and consist of many particles, there are quite a few corrections that need to be made. The main corrections are listed below.

- Out of cone corrections: Since the hadronic shower extends over a large area in space, some portion of the shower will fall outside the cone and all the energy will not be accounted for.

- Low energy particles: Hadronic showers contain many low energy particles (of order 2 GeV) where the calorimeter response is nonlinear so simple summing of energies is not correct.

- Underlying energy: Energy is measured from the underlying event that is due to the spectator quarks, and must be subtracted from the measured energy. Also there is noise due to the radioactivity of the uranium absorber plates.

The method used to obtain the jet corrections is called the Missing E_T Projection Fraction (MPF) method [41]. For these studies, one uses the principal of balancing the transverse momentum in events with only two objects. Events are used which consist of one jet, one highly electromagnetic object (photon which passes offline cuts), and no other objects in the event. These events should not contain a neutrino and thus the missing transverse energy ($\not{E}_T$) in the event can be attributed to the mismeasurement of the hadronic jet. By projecting the $\not{E}_T$ along the jet axis, the correction can be computed. The corrections are computed as functions of jet E_T, η, and electromagnetic content. In addition to the MPF method which uses electromagnetic events, Monte Carlo and minimum-bias events are also used to understand and make corrections for the various effects listed earlier, including out of cone showering, underlying event, and noise effects.

4.1.5 Missing Transverse Energy Reconstruction ($\not\!\!E_T$)

Neutrinos are produced in many interactions but unfortunately interact only weakly and thus cannot be detected directly. Their presence in an event can, however, be detected indirectly by measuring the $\not\!\!E_T$ of the entire event. The longitudinal component of the missing energy cannot be inferred since the momenta of the incoming partons is not known and also many particles escape down the beam pipe. The energy transverse to the direction of incoming partons can be computed since the particles that escape down the beam pipe contain very low transverse energy.

Each calorimeter cell is assigned two quantities, the measure of energy in that cell and the direction of the energy from the vertex to the center of the cell. All the transverse components of the cells are added together to produce the calorimeter missing E_T defined below:

$$\not\!\!E_T{}^{cal} = -\sum_i E_T^i \tag{4.1}$$

If a muon is present in the event, the total $\not\!\!E_T$ is equal to the calorimeter missing E_T minus the muon p_T vector. Any corrections made to jet energies must be included in the $\not\!\!E_T$ calculation. [42]

4.2 Particle Identification

The minimum cuts that are applied by the reconstruction program are very loose and are meant as a starting point to clean up further a particular sample of events. Unless additional quality cuts are applied to the data, large backgrounds can cause false identification to particles of interest. By adding quality cuts that are specifically designed to be highly efficient for the signal while reducing the backgrounds by a large amount, very clean identification of signal can be achieved. The particle ID parameters were developed using monte carlo, test beam and real data.

Most of the physics analyses at DØ involve investigating a given signal which manifests itself in a final state that contains electrons, photons, muons, jets, neutrinos, and taus. Independent of the physics source, the particle identification is somewhat universal. Similar particle identification can be used for different analyses; although the cuts which are applied depend on the particular analysis. Particle identification cuts are chosen to maximize the signal to background ratio for a given analysis. This analysis primarily uses photons and muons and thus only the particle identification of these is discussed in detail. The photon identification is similar to the electron identification except for the tracking requirements. The muon identification is useful for all muons but in this analysis is optimized for high p_T muons.

4.2.1 Photon ID

The additional quality cuts that are applied to the photon are listed below.

- Covariance matrix. This is the main tool for photon ID which quantifies the information contained in the electromagnetic shower shape. This algorithm, called the H-matrix algorithm [43], constructs a covariance matrix of the form:

$$M_{ij} = \frac{1}{N}\sum_{n=1}^{N}(x_i^n - \bar{x}_i)(x_j^n - \bar{x}_j) \tag{4.2}$$

  where x_i^n is the value of the observable i for electron n and $\bar{x}_i$ is the mean value of the observable i for the comparison sample. The sample used to determine the mean values was a sample of monte carlo and test beam electrons. Once the matrix is tuned on a signal sample, a χ^2 can be computed for each candidate given by:

$$\chi^2 = \sum_{i,j}(x_i^k - \bar{x}_i)H_{ij}(x_j^k - \bar{x}_j) \tag{4.3}$$

  where H is defined as:

$$H = M^{-1} \tag{4.4}$$

  There are 41 observables used for the H-matrix χ^2 which include the fractional energy in layers 1, 2, and 4, fractional energies of each cell in a 6×6 window centered on the most energetic tower in the third layer, the z-position of the interaction vertex, and the logarithm of the total energy. Thirty seven H matrices, one for each η tower, were tuned and calculated to account for the η dependance. The rejection power of the χ^2 variable is shown in Figure 4.1.

- Isolation. Only isolated photons can be accurately measured. An isolation variable is defined as:

$$\frac{E_{tot}(0.4) - E_{em}(0.2)}{E_{em}(0.2)} \tag{4.5}$$

where $E_{tot}(0.4)$ is the total calorimeter energy inside a cone of $R = \sqrt{(\Delta\eta)^2 + (\Delta\phi)^2} = 0.4$ and $E_{em}(0.2)$ is the total electromagnetic calorimeter energy inside a cone of $R = 0.2$, about the photon's direction (η, ϕ).

- No track match from the CDC or FDC within a road of $\Delta\eta = \pm 0.1,\ \Delta\phi = \pm 0.1$ about the photon's direction.

4.2.2 Muon ID

The additional muon cuts that are applied to the selection are:

- Hits in two layers: Two out of the three layers including the first layer must have hits from the muon reconstruction.

- Impact parameters: Two different impact parameter cuts are required; these impose the constraint that the muon track point back to the vertex.

The first, a *non-bend impact parameter* projects the muon track into the xy plane, and extrapolates the track to the center of the detector and calculates the impact parameter from the vertex. The second, the *bend-view impact parameter* projects the muon track in the plane that it bends in and again determines the impact parameter from the vertex.

- Timing of track: In order to reduce the contamination from cosmic rays and random tracks, a cut is made on the timing of the track relative to the beam crossing of the interaction.

- Muon Quality (IFW4): The muon reconstruction makes a number of cuts on the number of hit modules, impact parameters, and hit residuals. IFW4 is the number of items which fail the cuts.

- Muon calorimeter track (MTC): This cut uses the fact that the muons are the only particle that completely penetrate the calorimeter. A muon will on average deposit between 1 to 3 GeV of energy in the calorimeter. A useful cut is the requirement that a large fraction of the hadronic layers of the calorimeter has non-zero energy along the muon track. More details will be mentioned later when discussing the backgrounds to the $W\gamma$ signal.

- Path length through iron. In order to have the muon momentum measured well, it must pass through enough magnetized iron. A cut is placed on the integrated magnetic field, $\int B \cdot dl$.

- Isolation: The muons coming from W's should be isolated from other objects in the event. The isolation is defined by requiring the muon to be separated by a given ΔR from a jet above some minimum E_T. For this analysis a cut of $R = 0.5$ from any jet which has $E_T > 10$ GeV was made.

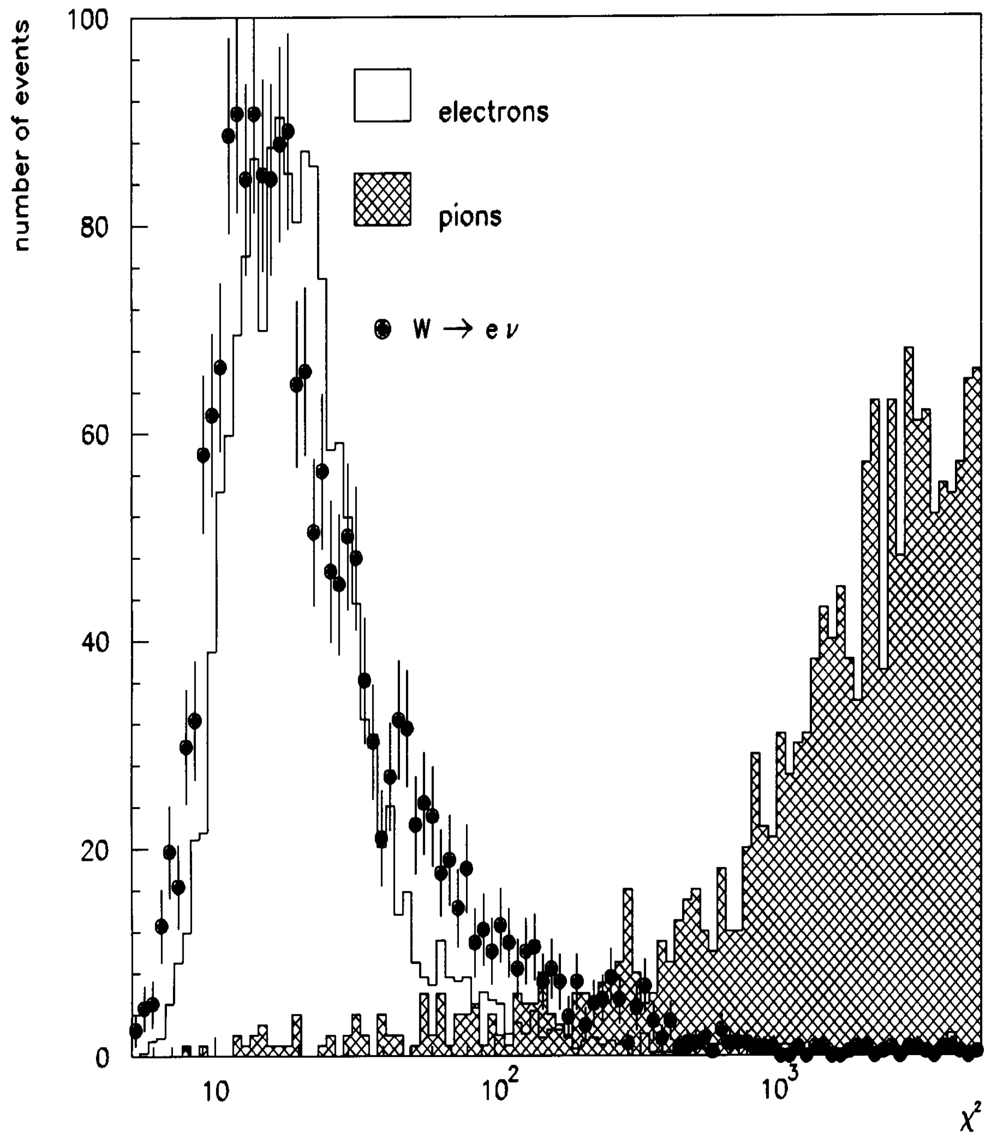

Figure 4.1: χ^2 distributions from test beam electrons and pions, and electrons from $W \to e\nu$ events.

Chapter 5

Event Selection and Efficiency

This chapter describes the criteria used for the selection of $W\gamma$ candidates, including particle identification (ID) and kinematic cuts. It also describes the data stream and triggers that were used to collect this data. Finally the efficiencies for the triggers and particle selection are presented. Plots showing various particle identification (ID) variables and kinematic distributions are shown.

5.1 Data Selection

The amount of data that is reconstructed is too large to be easily accessible to do physics analysis. Instead the data are broken up into various 'data streams' that allow one to use a smaller sample of events to perform the analysis. The 'single high p_T muon' stream was used for this analysis. Some minimum cuts were applied to this data stream and are listed below.

- 1 muon $p_T > 15$ GeV/c
- $\mid \eta \mid < 2.4$
- IFW4 ≤ 1
- $\mid$ impact bend view $\mid \leq 25$ cm
- $\mid$ Tfloat $\mid \leq 600$ nsec
- Min Cal Energy(2NN) = 0.5 GeV

All of the above selection criteria have been discussed in the reconstruction section except the min cal energy cut. The cut looks for energy deposition in the calorimeter around the muon and requires that all the nearest neighbor cells and next to nearest neighbor cells ('2NN') have at least a total of 0.5 GeV of energy deposited in them. Many different analyses based on events with a muon make use of the data selected with these cuts. This data stream was cross checked by examining a second data stream which required a lower p_T muon and also an electromagnetic cluster with $E_T > 8$ GeV. The final $W\gamma$ event sample from both the data streams contained identical events.

5.2 Particle Identification and Kinematic Cuts

The particle ID cuts that are used in selecting events were described in the last chapter. These criteria were optimized using data and Monte Carlo. The cuts are listed below:

Muon

- IFW1 ≤ 1
- $|$ impact bend view $| \leq 25$ cm
- $|$ impact nonbend view $| \leq 25$ cm
- $|$ Arrival time (Tfloat) $| \leq 600$ sec
- MTC Hadronic Fraction (Hfrac) ≥ 0.75
- $\int B \cdot dl \geq 0.6$ for $| \eta | \geq 0.7$

Photon

- no track
- EM fraction > 0.9
- Hmatrix $\chi^2 \leq 100/200$ for CC/EC
- Isolation ≤ 0.1

Kinematic cuts

The particle ID cuts can be studied independently of a particular signal and simply optimized to be efficient for a given particle, regardless of the overall event source. This is true assuming the characteristics of the particle (E_T, η) are similiar for the signal and study samples. The kinematic cuts however, are uniquely related to the particular event signal that one is interested in. In this case the cuts are optimized by examining the effects of the selection criteria on acceptance of the $W\gamma$ Monte Carlo events and on events from the most significant backgrounds to this signal. All the kinematic selection criteria are listed below:

- 1 muon $p_T > 15$ GeV/c
- 1 Photon $E_T > 10$ GeV
- $\mid \eta_{\rm muon} \mid \leq 1.0$
- $\mid \eta_{\rm photon} \mid \leq 1.1$ and $1.5 \leq \mid \eta_{photon} \mid \leq 2.5$
- No additional muon with $p_T \geq 10.0$ GeV/c

  for $\mid \eta \mid \leq 1.7$ (no quality cuts)
- $\not\!\!E_T \geq 15$ GeV
- $\Delta R(\mu - \gamma) \geq 0.7$
- $M_T(\mu\nu) \geq 30$ GeV/c^2
- MTC Track with $\mid \phi - \phi(\not\!\!E_T\ ) \mid \leq 0.3$ and Hadronic Fraction (Hfract) > 0.75, Energy deposited in calorimeter (Etrack) ≥ 0.8 GeV, $\mid \eta \mid \leq 2.7$ (explained in section on $Z\gamma$ bkg (Section 6.3).

The η cut on the muon requires the muon to be in the central muon chambers (CF) while the η cut on the photon requires it to be in the CC or EC, rather then in the Inter Cryostat Detector (ICD) where the photon identification is poor. The elimination of events with an additional muon that has a

p_T >10 GeV/c is designed to remove $Z\gamma$ events, where the Z decays to two muons. The missing E_T ($\not\!\!E_T$) requirement selects events with a neutrino; here ($\not\!\!E_T$) is defined as the vector difference of the calorimeter missing E_T ($\not\!\!E_{T\ cal}$) and the muon p_T. The ΔR cut as discussed earlier suppresses radiative decays while maintaining a high acceptance for production events, thus increasing sensitivity for the anomalous couplings. The M_t cut is based on the transverse mass of the $\mu\nu$ system, defined as

$$M_T = \sqrt{2P_T^{\mu}P_T^{\nu}(1 - \cos\phi^{\mu\nu})}$$

where $\phi^{\mu\nu}$ is the azimuthal angle between the muon and the $\not\!\!E_T$. This cut is fully efficient for the signal and provides some rejection for the QCD background (chapter 6). The MTC Track cut (also explained in much more detail in chapter 6) is applied because it greatly reduces the substantial $Z\gamma$ background. The MTC track cut uses the calorimeter to find additional lost muons that were not found by the muon system that for example, could arise from $Z\gamma$ production with the Z decaying into two muons. More information about the MTC package can be found in [44]. After all of the above cuts are applied, 58 candidate events are left from the initial sample of events.

Some of the kinematical distributions are shown in the next few figures for these 58 $W\gamma$ candidates. Figure 5.1 presents some of the distributions of the muon, including its p_T η, and ϕ. These distributions are consistent with muons coming from W's. The p_T spectrum falls off rapidly while the η

distribution falls off at $\eta = \pm 1$ due to geometric coverage. Figure 5.2 shows the kinematical distributions for the photon including the photon E_T, η, and ϕ. The photon p_T spectrum also falls off rapidly as expected from the Monte Carlo. Finally, Figure 5.3 gives the cluster transverse mass of the $W\gamma$ system, the ΔR distribution, and the jet multiplicity. The cluster transverse mass distribution has a peak at about 80 GeV/c^2 as is expected from radiative decay of the W. The jet multiplicity shows the rapid decrease in the number of jets in each event for the $W\gamma$ candidates. The distribution follows approximately that of standard W production where the jet multiplicity is falling off as α_S, since each jet introduces a factor of α_S in the cross section.

Figure 5.4 shows an event display for a $W\gamma$ candidate. The event contains an isolated muon with three layers of hits and a matching calorimeter track, an isolated photon, and a substantial amount of $\not{E}_T$. This event has the muon and photon well separated and a large cluster transverse mass, indicating a production event.

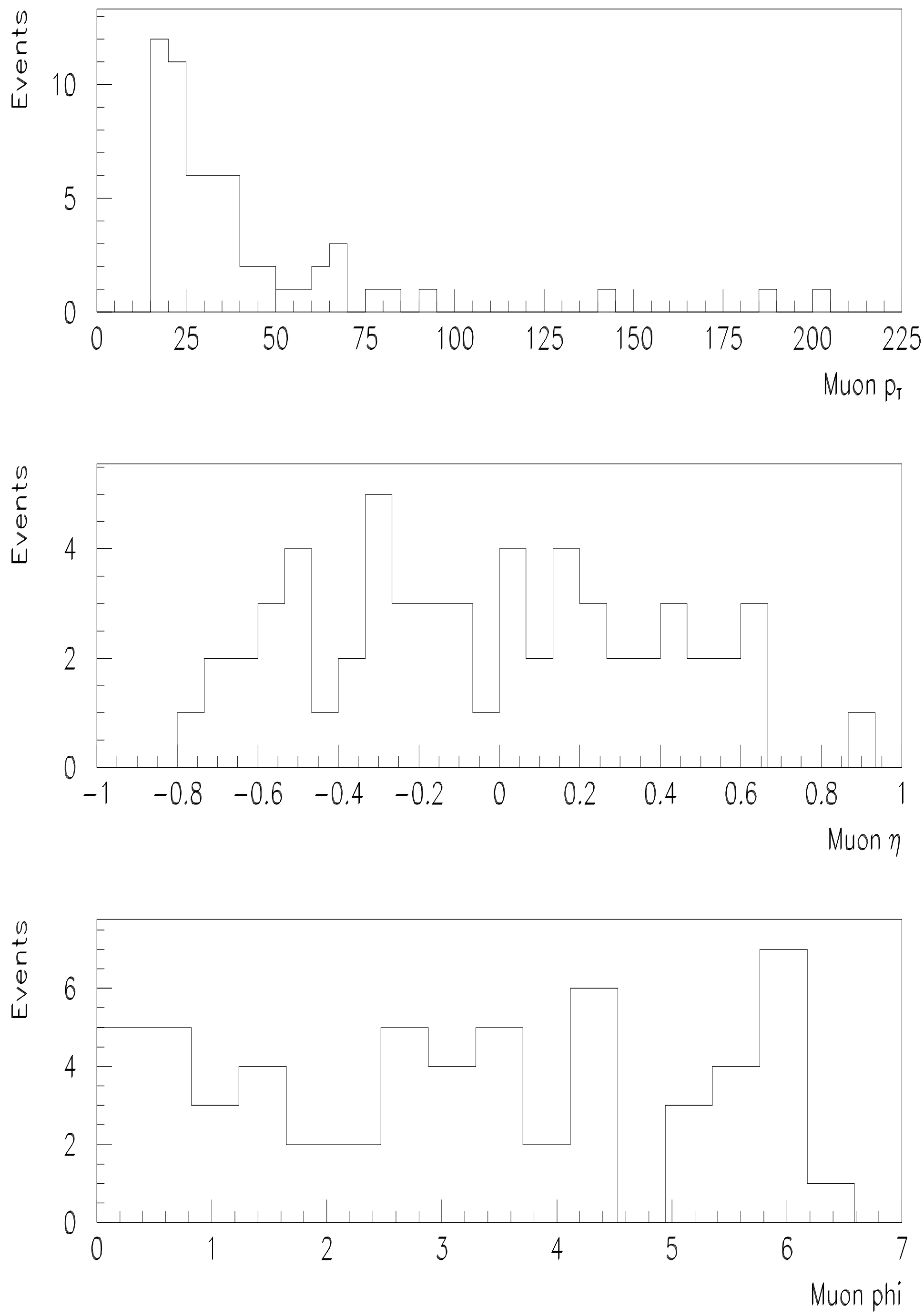

Figure 5.1: Kinematical distributions for the muon in $W\gamma$ events.

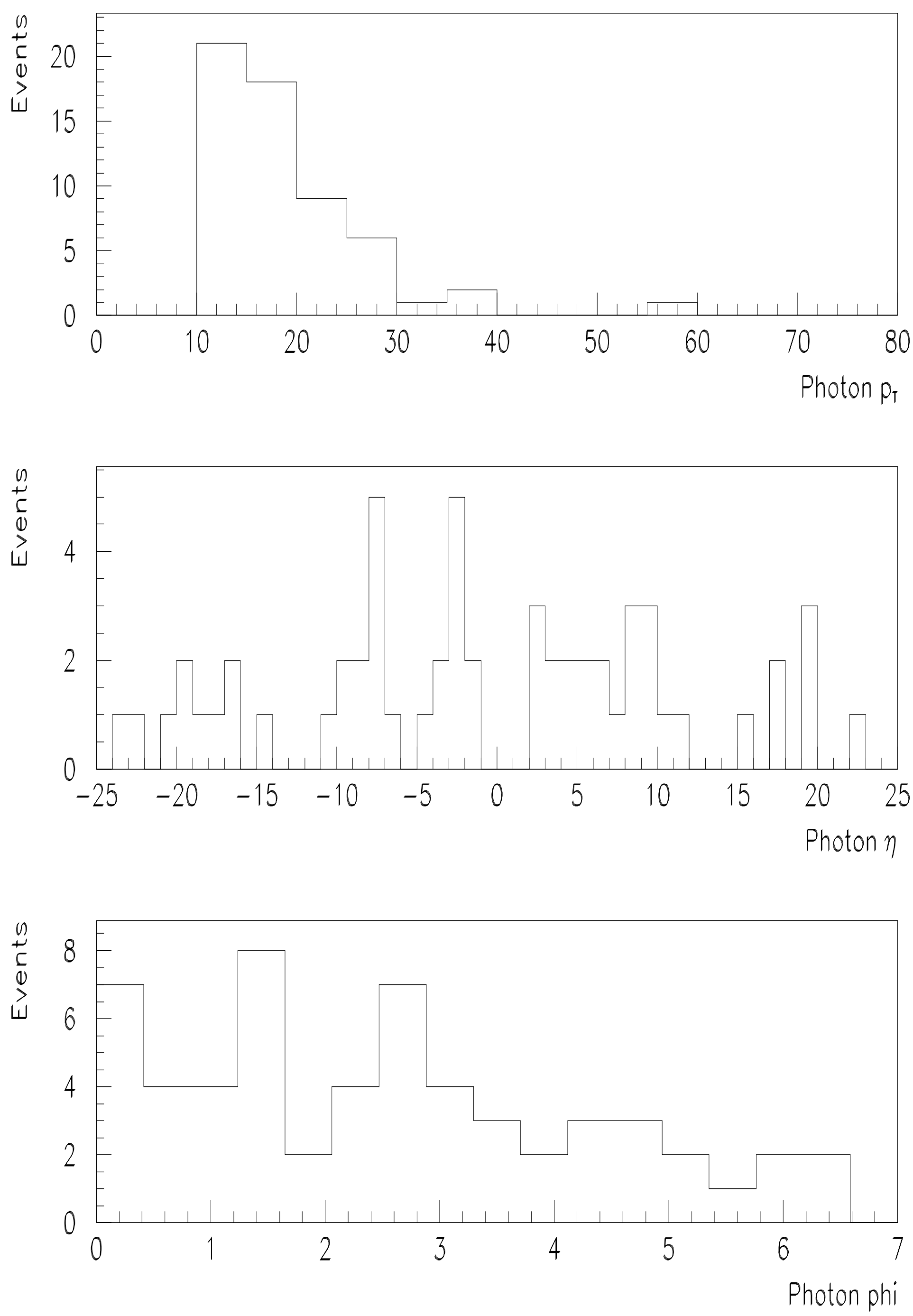

Figure 5.2: Kinematical distributions for the photon in $W\gamma$ events.

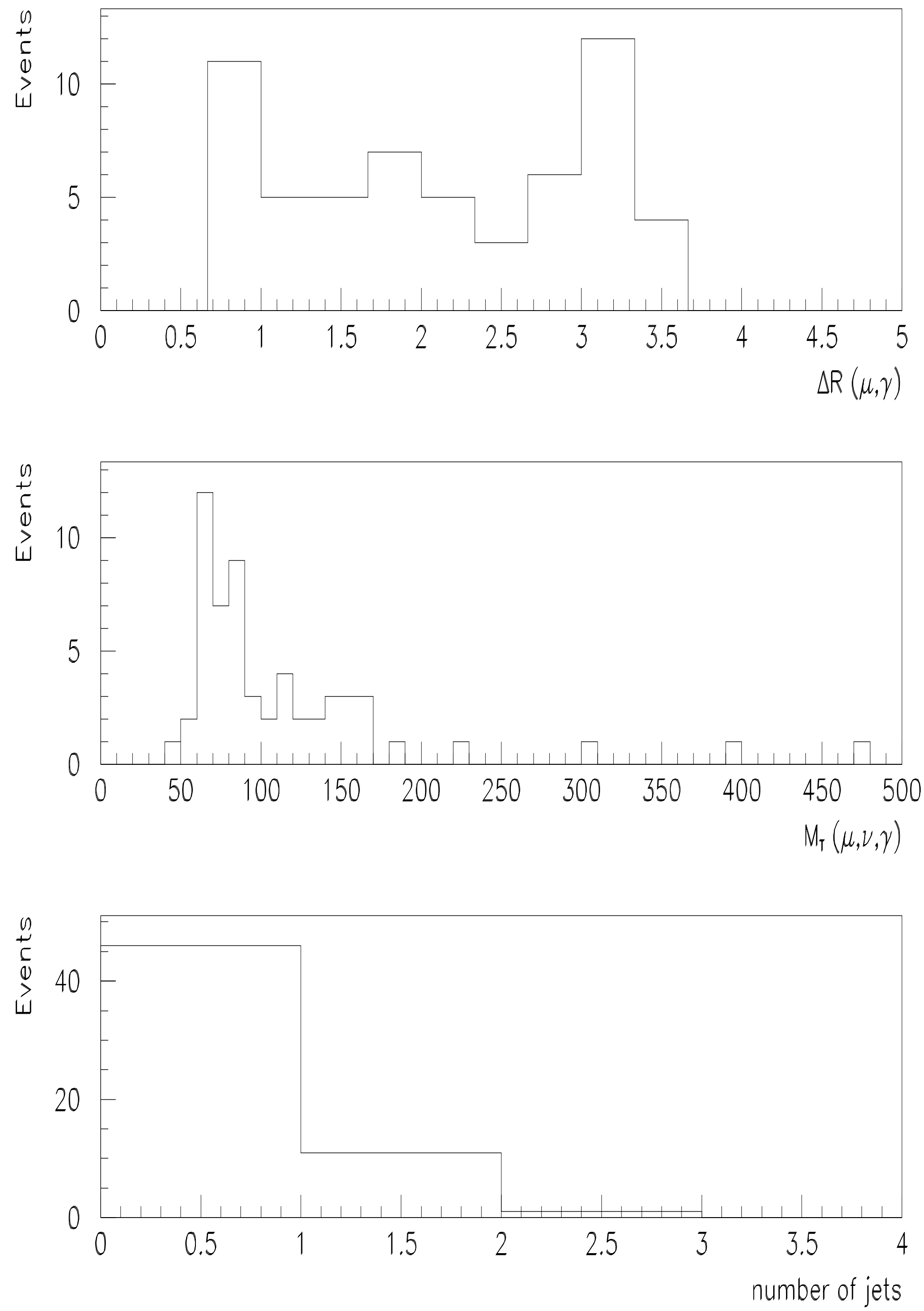

Figure 5.3: Kinematical distributions including ΔR, cluster transverse mass, and the jet multiplicity for jets with $E_T > 10$ GeV.

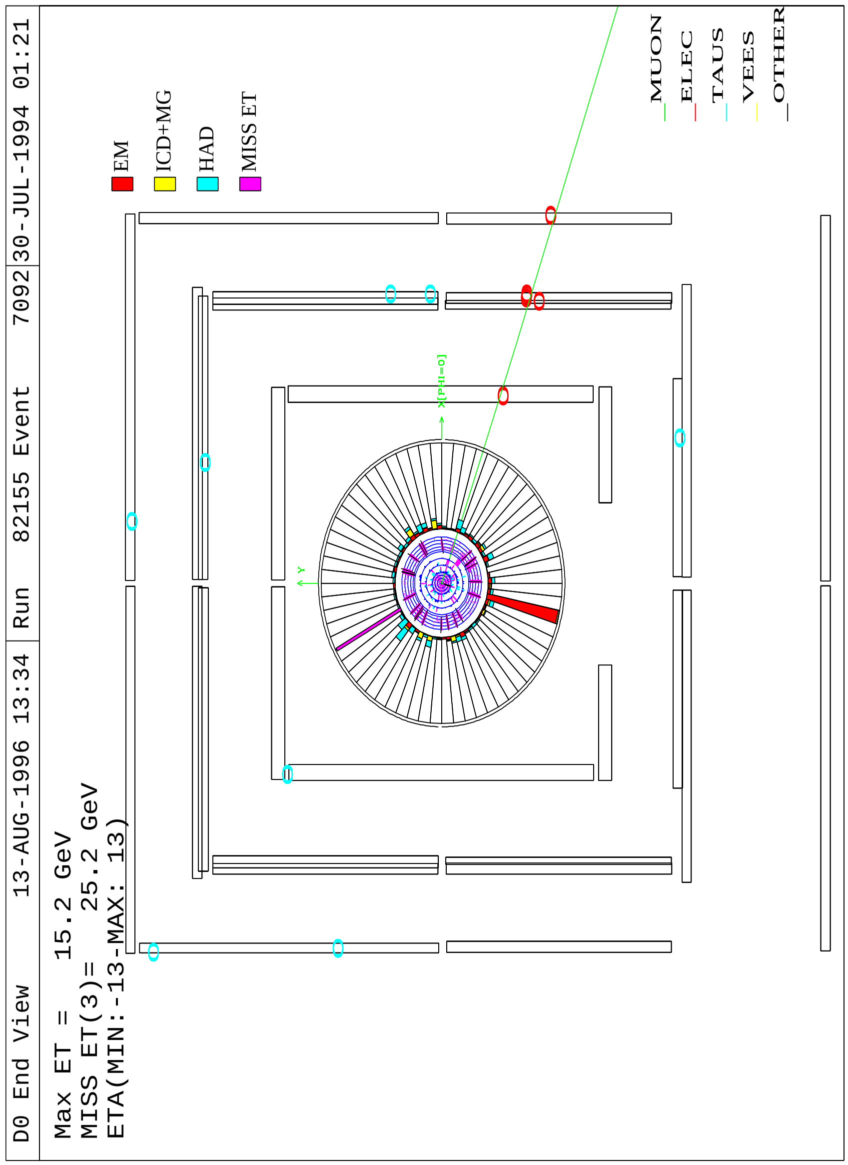

Figure 5.4: Event display showing the end view of the detector. The event shows a clean muon with hits on three layers and contains a calorimeter track matching to it. The photon is shown opposite the muon.

5.3 Efficiencies

In order for a cross section to be calculated, all the efficiencies must be measured including the trigger efficiency, the particle ID efficiency, and the geometric and kinematic acceptance. Both data and Monte Carlo events are used to determine efficiencies, with the data being used as much as possible.

5.3.1 Trigger Efficiency

The trigger as was mentioned in the detector section is broken up into two main levels, the L1 trigger and the L2 trigger. The L1 trigger used for this analysis was called MU_EM_1. This trigger was never prescaled and required 1 muon in WAMUS ($|\eta| < 1.7$) and 1 electromagnetic cluster with $E_t > 7$ GeV. The L2 filter MU_ELE was used; this filter had no L1.5 trigger requirement for the muon or electromagnetic object. A muon with $p_t > 8$ GeV/c (no calorimeter energy requirement) and an electromagnetic cluster with $E_t > 7$ GeV were required. This filter was primarily designed for a top quark search and turned out to be an ideal trigger for this analysis since it contained loose requirements and was never prescaled.

The muon portion of the trigger efficiency was measured using the standard technique of selecting events in an unbiased manner and then seeing how often the trigger is fired. We studied a sample of events collected without a muon trigger requirement, but with an EM trigger requirement which was tighter than the electromagnetic portion of the MU_ELE trigger. The tighter requirements for the electromagnetic portion of the trigger are required to obtain the efficiency for only the muon portion of the trigger. The triggers used were single electromagnetic triggers which were often used as monitor triggers. After the trigger requirement, all the final muon offline cuts were applied to this sample; then the number of surviving events which passed the MU_ELE trigger were counted. The muon trigger efficiency is given by

$$\text{Trig. Eff} = \frac{\text{Events (passing MU\_ELE + muon offline cuts)}}{\text{Events(passing muon offline cuts)}}$$

There is no muon p_T dependence of the trigger since the p_T requirement offline (15 GeV/c) is well away from the trigger threshold (8 GeV/c). The muon portion of the trigger is found to have an efficiency of 73.3 $\pm$ 2.7 %. The photon trigger efficiency was estimated as a function of E_T from Monte Carlo data. By parameterizing the trigger efficiency as a function of E_T, a turn-on-curve can be determined for the trigger efficiency. Monte Carlo data were used because there is no clean source of low energy photons that are unbiased. The photon trigger efficiency is dominated by the Level 1 efficiency which is E_T dependant. The turn on curve for the Level 1 electromagnetic trigger, the trigger efficiency as a function of the photon E_T, is shown in Figure 5.5 [45]. The points are fitted to an error function, giving about 80% efficiency at the offline cut of 10 GeV. The trigger becomes fully efficient for $E_T^\gamma > 14$ GeV and has an average efficiency of about 97% for photons where the E_T follows a Standard Model distribution.

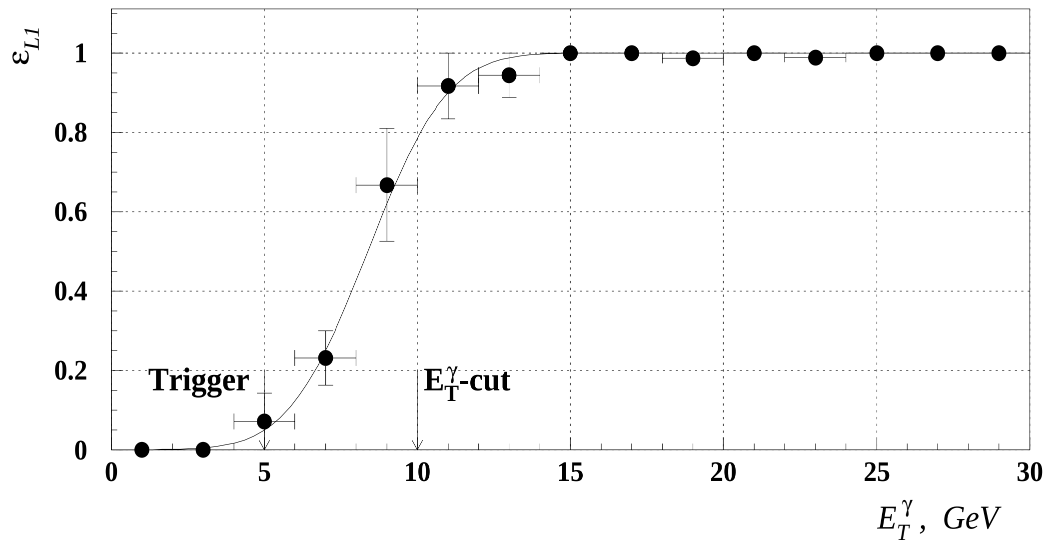

Figure 5.5: Level 1 trigger turn-on curve for the electromagnetic trigger with a threshold of 7 GeV.

5.3.2 Particle ID Efficiency and Acceptance

The particle efficiencies were measured using a combination of Monte Carlo events and collider data.

Muon Efficiencies

The muon ID efficiencies were measured by using both collider and Monte Carlo data. The standard technique to measure particle ID efficiencies is to find a sample of unbiased events to study the efficiencies. For both the muons and electrons, the ideal sample is the Z sample (events which have been selected to be $Z \to l^+l^-$ decays where $l = \mu, e$) . For the muon ID efficiencies, the Z sample was used by requiring a sample of two high p_T muons where one of the muons passes extremely tight quality cuts (tighter than used for the $W\gamma$ selection) and there is no ID selection on the 2nd muon. The second muon is then unbiased and used for efficiency studies.

Some of the muon efficiencies can only be calculated from Monte Carlo data. These are the efficiencies that depend on the muons kinematic distributions and are essentially the acceptances of the muon detector system. They include the A layer requirement, the $\int B \cdot dl$ cut, plus the overall geometric acceptance of the muon system.

The Monte Carlo data used to study the kinematic efficiencies and acceptances is produced in three steps. The first stage is the event generator, the Baur Monte Carlo that was described in section 2.3.1. This Monte Carlo program was modified to produce the 4-vectors of the generated particles in the event and then to convert these into the data structure that is used in DØ software (ZEBRA). Following this stage, the generated events were passed through a complete detector simulation package (GEANT) which tracks all the particles through the detector and stores all the information as if there were a real event coming out of the detector. In the final stage, the data is reconstructed and run through an additional package called MUSMEAR [46].

MUSMEAR is a software package used to add to Monte Carlo generated data the characteristics of actual detector performance. This package is developed by using real cosmic ray data to measure muon chamber efficiencies, related to the muon chamber drift time, pad latch inefficiencies, and misalignment with respect to other chambers. GEANT assumed 100% chamber efficiency while generating data; MUSMEAR modifies this data by eliminating some hits, in order to match the efficiency that was determined from cosmic ray data. MUSMEAR also smeared the position of hits in the muon modules, using a gaussian distribution with a sigma of 3 mm. This smearing of Monte Carlo data was adjusted to make the $Z \to \mu\mu$ Monte Carlo data agree with data reconstructed with D0RECO. For the central region, the exact efficiencies for the muon chambers changed a small amount during the course of the run, due to aging of the chambers over time. The efficiencies were calculated for different running periods and were luminosity-weighted to calculate the effective efficiency for the entire data sample. This effect is very small but was nonetheless included (via MUSMEAR) in the Monte Carlo data.

The muon ID efficiencies are shown below together with the sources of data used to determine them.

Table 5.1: Muon efficiencies

A layer + $\int B \cdot dl$	0.81 ± 0.02	MC
IFW4 + MTC	0.91 ± 0.03	data & MC
Tfloat + XY + RZ + isolation	0.85 ± 0.02	data

The A layer + $\int B \cdot dl$ efficiency is the acceptance for requiring the A layer and the $\int B \cdot dl$ cut. This is simply the geometric acceptance of these two cuts for the $W\gamma$ signal. The IFW4 and MTC cut take into account the muon reconstruction efficiency (IFW4) and the calorimeter track match requiement (MTC). The remaining particle ID cuts (Tfloat + XY + RZ + isolation) are correlated and all calculated from the Z sample.

Photon Efficiencies

The photon ID efficiencies were determined using both $Z \to ee$ events selected from the collider as well as Monte Carlo data from simulations. Electrons interact almost identically to photons in the DØ calorimeter, so the $Z \to ee$ data (with electrons of p_T typically 45 GeV/c) can be used to determine the efficiency for high p_T photons. Monte Carlo based studies are used to extract the low energy behavior of photons, since the analysis based on the $Z \to ee$ data is only valid for high E_T photons. Unbiased electrons were obtained by requiring one electron from the $Z \to ee$ decay to pass tight quality cuts; then the second electron from the decay was used for efficiency studies. If both the electrons passed tight quality cuts, both were used to measure the efficiency. Due to the good resolution of the electromagnetic calorimeter, a narrow window in the invariant mass spectrum for the Z can be used to define a signal region, and help to reduce the background. This $Z \to ee$ data sample does contain some background but this contamination can be estimated using a 'sidebands' technique. By looking at both the invariant mass regions outside the Z peak, the background can be averaged for the two regions to determine the fraction of the background in the signal region. Besides fitting the background to a flat function, the background can also be fit to a linear function to help determine systematic errors on the background fraction. The signal region for the $Z \to ee$ data was chosen to be between an invarient mass of 81 GeV/c^2 and 101 GeV/c^2. The sidebands were choosen in the range $60 < M_{ee} < 70$ GeV/c^{2}and $110 < M_{ee} < 120$ GeV/c^2. The true efficiency for the signal is given by

$$\varepsilon = \frac{\varepsilon_s - \varepsilon_b f_b}{1 - f_b} \tag{5.1}$$

where ε_s is the efficiency measured in the signal region, ε_b is efficiency measured in the background region, and f_b is the fraction of background events in the signal region to the total number of events in the signal region. The efficiencies are shown below [47]

Table 5.2: Photon efficiencies

Hmatrix χ^2, EMF, Isolation	0.917 ± 0.004 CC 0.915 ± 0.004 EC
Random track overlap probability	0.139 ± 0.005 CC 0.161 ± 0.008 EC
Track in road efficiency	0.831 ± 0.005 CC 0.856 ± 0.008 EC

The final errors on the photon efficiencies are determined by adding in quadrature the statistical and the systematic errors, where the systematic error was determined by taking half the difference in the efficiencies from the two different methods used to determine the background.

The random track overlap rate is the probability that a random track falls within the road of the photon and is reconstructed as an electron. This is a measure of an inefficiency since photons become electrons and are thus not contained in the final data sample. The overlap rate was determined by using the $Z \to ee$ data to produce 'emulated' photons. Since the $Z \to ee$ data can be used as a source of good photons as far as calorimeter information is concerned, this data can also be used to determine the random track overlap rate. By rotating the ϕ of the electrons by increments of $\pi/2$, 'emulated' photons can be created in the detector with new tracking roads defined. By seeing how often this new 'photon' is reconstructed as an electron, the random track overlap rate can be measured [48]. This technique implicitly takes into account the effects of multiple interactions since additional interactions create more tracks. The random track overlap rate is larger in the EC as one expects, since the track multiplicity is higher and the roads used for track reconstruction are wider. The track-in-road efficiency is the efficiency to reconstruct a track from the tracking system and be matched to the electromagnetic cluster. The efficiency is explicitly used for electron ID, but is also used to determine the overall photon efficiency since one needs to know the tracking efficiency when determining the random track overlap rate. This efficiency was determined the same way as the calorimeter quantities, but in selecting the $Z \to ee$ data, one must select events which were also reconstructed as photons.

Another inefficiency for photons occurs when the photons undergo pair production ($\gamma \to e^+e^-$) in the presence of nuclei. If the pair production occurs before the drift chambers, the photon will be reconstructed as an electron. The rate for this process is calculated using the z-position of the vertex, the polar angle of the photon, and the amount of material in the detector. The photon conversion probability is calculated from D0GEANT and ranges from 10% in the central region to about 30% in the forward region. The conversion factor must also be multiplied by the efficiency to reconstruct a track.

One additional effect must be taken into account in calculating the efficiency for the detection of the photons. The efficiency measured from the $Z \to ee$ data is only valid for high E_T electromagnetic objects but photons are accepted down to an E_T of 10 GeV. There does not exist a high statistics high purity sample of low energy photons so a full 'plate level' (including detailed simulation of the interactions in the calorimeter) Monte Carlo is used to extract the low energy behavior of the efficiency. The efficiency drops somewhat at low E_T because the H-matrix and isolation variables used in identifying electrons are tuned to high E_T electrons. The isolation cut becomes less efficient because noise and energy from the underlying event can contribute enough energy around the cluster so the isolation cut will not be satisfied. The low E_T efficiency for both the CC and the EC is shown in Figure 5.6. The efficiencies shown here are normalized to the efficiency that was determined by the Z sample so only the shape is used from the Monte Carlo [48].

The total efficiency for photons is given by

$$\varepsilon_{tot} = \varepsilon_{cal}(1 - P_{overlap} - P_{conv}\varepsilon_{trk}) * g(E_t) \tag{5.2}$$

where ε_{trk} is the track in road efficiency determined from the Z sample and given in Table 5.2, and $g(E_t)$ is the low E_T dependent efficiency from Monte Carlo.

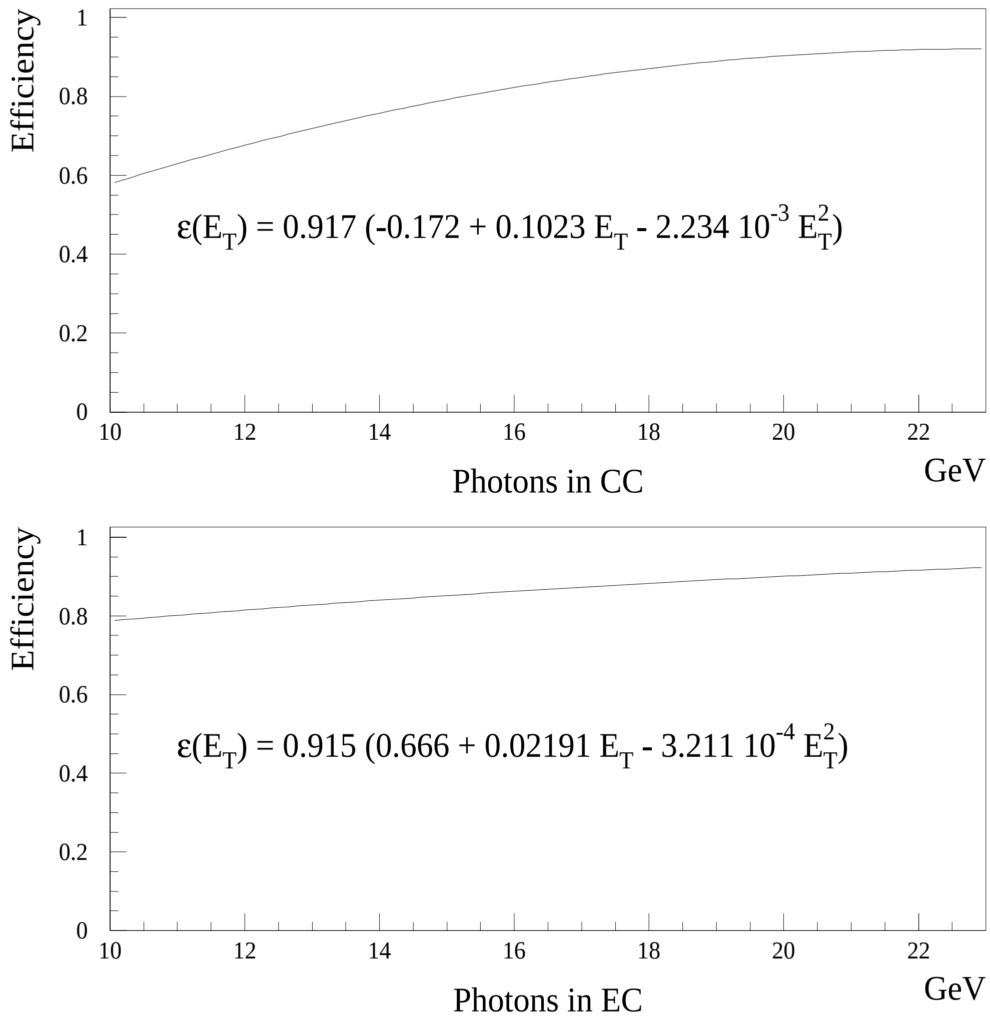

Figure 5.6: The E_T dependent efficiency for photons with E_T below 23.0 GeV. Central photons are more sensitive because for a given p_T the energy is lower and the efficiency drops with energy.

Overall Efficiency

All the efficiencies and acceptances are shown below.

Table 5.3: Summary of efficiencies and acceptances

kinematic and geometrical	19.38 ± 0.3 %
total muon efficiency	$50.1 \pm 2.9\%$
total photon (id,random track, conversions)	$51.0 \pm 2.57\%$
trigger efficiency	$71.1 \pm 3.4\%$
total acceptance $\times$ efficiency	$3.53 \pm 0.32\%$

The kinematic and geometric acceptance accounts for all the p_T, $\not\!\!E_T$, and η cuts applied to the signal and is determined from the Baur Monte Carlo. The total muon efficiency is the product of all the ID efficiencies and the muon acceptance. The muon acceptance accounts for the lost muons within the η coverage that includes all the cracks in the system. The trigger efficiency includes the muon and photon portions giving a total acceptance $\times$ efficiency to be $3.53 \pm 0.32\%$.

Chapter 6

Backgrounds

This chapter goes into detail about all the backgrounds to the $W\gamma$ signal and the calculation of these backgrounds. The $W\gamma$ signal has a very small cross section and can contain a significant amount of background. Studying these backgrounds, determining the amount, and finding ways to reduce them is a significant portion of the analysis. Both particle identification and kinematic cuts were chosen to optimize the signal with respect to the various backgrounds.

There are two types of backgrounds that can contaminate a signal, fake backgrounds and physics backgrounds. Fake backgrounds occur when an event from a different type of process is misidentified for some reason and fakes the desired signal. Physics backgrounds occur when another signal contains the same final state as the desired signal. The backgrounds that dominate the $W\gamma$ signal are fake backgrounds; including the QCD background and the $Z\gamma$ background where one muon is not reconstructed. The estimations of the backgrounds are determined from data as much as possible and several cross checks were performed to fully understand the background calculations. The individual backgrounds are described below in detail.

6.0.3 QCD

The largest background to this analysis is due to QCD processes which include W + jet production where a jet is misidentified as a photon, and Z + jet where a jet is misidentified as a photon and one muon is lost. A jet can be misidentified as a photon; for example, when a jet fragments into a leading π^0 the resulting $\gamma\gamma$ decay is indistinguishable from a single real photon in the detector. When the misidentification occurs along with a muon from W production, the resultant event can fake the signal. A jet fragmenting into a leading π^0 is the main source for fake photons, although leading η's also give a substantial contribution. Since some of the processes that contribute to this background are not well understood, i.e. fragmentation, a data-based method is used to estimate the background.

In order to determine the amount of background, the rate at which a jet is misidentified as a photon needs to be calculated. The total QCD background can be expressed as

$$\#\,\text{of events} = \sum_{\text{CC,EC}} \text{N} \times \text{prob}(\text{jet} \to \gamma) \times \text{N}_{\text{jets}} \tag{6.1}$$

where N is a normalization factor to account for the difference in triggers between the signal and background data samples. N_{jets} is the number of jets in the W + jet sample where all the identicle cuts are applied as in the signal except for any photon ID cuts. The quantity prob($jet \rightarrow \gamma$) is the E_T dependant rate; and the sum extends over the central and endcap calorimeters, which have different fake rates.

This background calculation is somewhat complicated due to the difference in triggers between the signal and background samples. Different triggers were used because the signal trigger included the requirement of an electromagnetic object, so signal data could not directly be used for the background calculation. Two triggers were used to collect the background data, the W inclusive triggers labeled MU_1_MAX and MU_1_CENT_MAX. The W inclusive triggers were prescaled during the run while the MU_ELE trigger used for the signal never was. As a further complication, the signal trigger MU_ELE contained looser requirements than the W inclusive triggers; these differences between the two must be accounted for. The W inclusive triggers needed a L1.5 trigger confirmation, something that wasn't required for MU_ELE. The L2 trigger criteria was also different; MU_ELE had no calorimeter confirmation requirement (energy deposited in the calorimeter around the projected track of the muon) while the W inclusive triggers did. Also the track quality for MU_ELE was somewhat looser than that for the W inclusive triggers. The last difference between the triggers is the p_T requirement in L2. The W inclusive trigger had a 15 GeV/c p_T cut while MU_ELE had an 8 GeV/c p_T cut.

The total normalization factor applied to calculate the background is given by eqn 6.2.

$$N = \frac{(\text{Lum Prescale})\times(\text{L2 } p_T \text{ cut})}{(\text{best track req.})\times\ (\text{cal confirm})\times\ (\text{L1.5 trigger})} \tag{6.2}$$

N $= 2.469 \pm 0.263$

The individual factors used to normalize the background triggers to the signal trigger are shown below in Table 6.1.

Table 6.1: Individual factors contributing to the overall normalization factor

LUM Prescale	1.289 ± 0.069
L1.5 trigger efficiency	0.677 ± 0.024
track requirements	0.97 ± 0.012
cal confirmation	0.936 ± 0.016
L2 p_T cut	1.176 ± 0.103

All of the above factors were calculated from data except for the L2 p_T cut. The prescale ratios were determined by measuring with the luminosity utilities [49, 50], the luminosity seen by each trigger. The L1.5 trigger introduces an additional inefficiency and also explicitly requires 3 layer muon tracks. To properly take this into account the ratio of 2 layer tracks to $2+3$ layer tracks was determined for good muons. This ratio was multiplied by the efficiency of L1.5 trigger for 3 layer tracks (since the efficiency for 2 layer tracks $\approx$ 0) to determine the L1.5 trigger factor [51]. The effect of the different L2 p_T thresholds was found using $W\gamma$ Monte Carlo since the p_T spectrum of the muon from $W\gamma$ events is somewhat different than for the muon from the background data samples.

Determining the probability for a jet to mimic a photon was determined from a large QCD multijet sample. Extremely large data samples are required to do this study since the fake probability is very small (on the order of 10^{-4}). The sample of data was collected by requiring various single jet triggers. This sample of data is dominated by multijet production so any photons identified in the sample (once real direct photon production is subtracted) are likely to come from jet misidentification. By removing the leading jet from the event and examining only the non-triggered jets, an unbiased sample of jets can be studied. Also, a $\not\!\!E_T$ cut of 15 GeV was applied to remove W events or events with a large jet mismeasurement. About 1.5 million events were used for this study.

The photon fake probability is in general a function of E_T. The photon and jet spectrums were divided and a linear binned fit was performed for both the CC and EC. The fits are shown in Figure 6.1 with the corresponding binomial errors. The fits give the following values.

$$\text{Fake CC} = 0.78 \times 10^{-3} + 1.02 \times 10^{-5} \times E_t$$

$$\text{Fake EC} = 0.156 \times 10^{-2} - 0.360 \times 10^{-5} \times E_t$$

One should note this data contains both fake photons and real photons from direct photon production; thus direct photons must be subtracted to give the real fake rate. The amount of real photons can be expressed as a

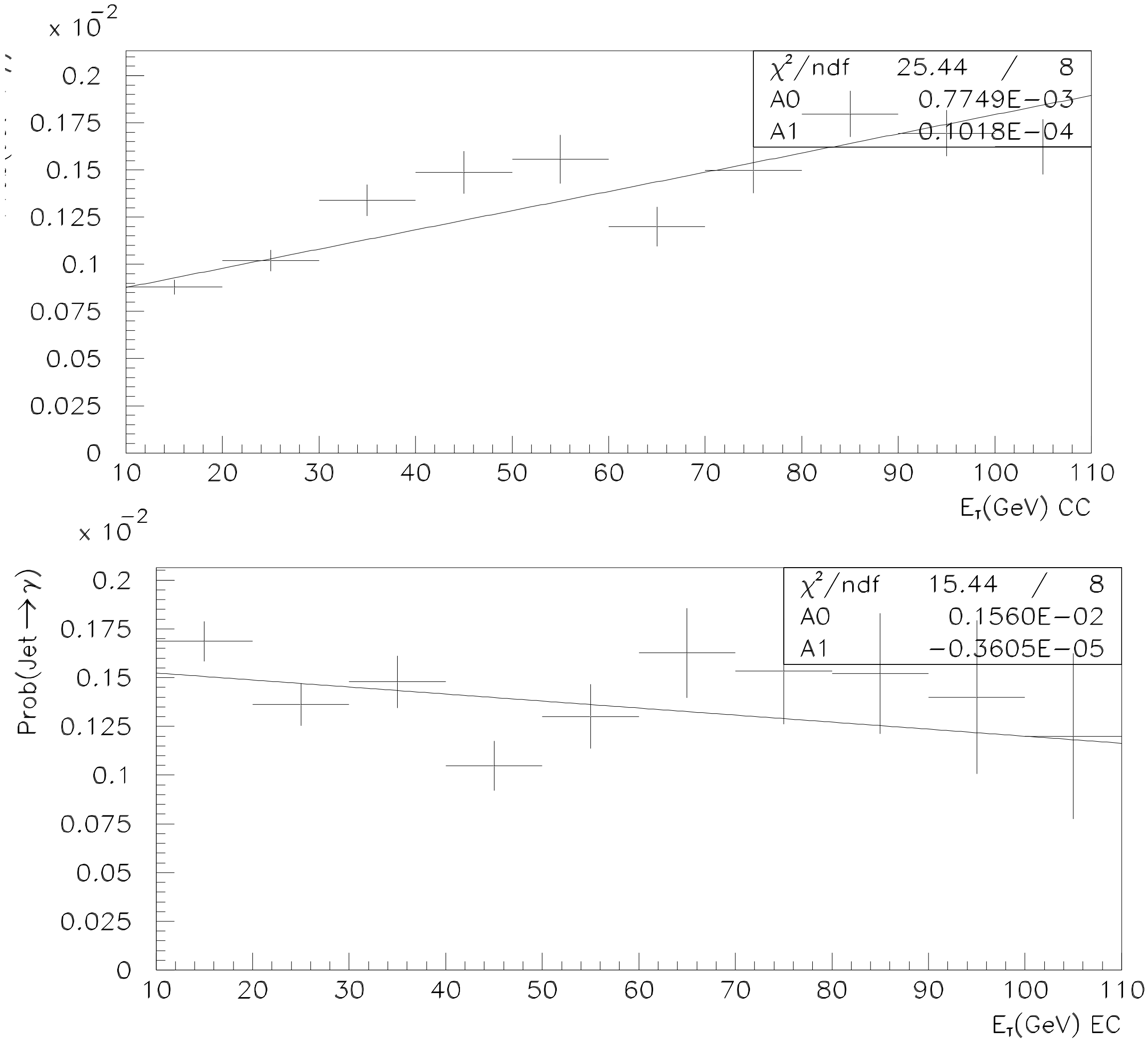

Figure 6.1: Combined fake rates for (jet$\rightarrow \gamma$) and direct photon production, for the CC and EC. A linear binned fit is performed with the binomial errors shown.

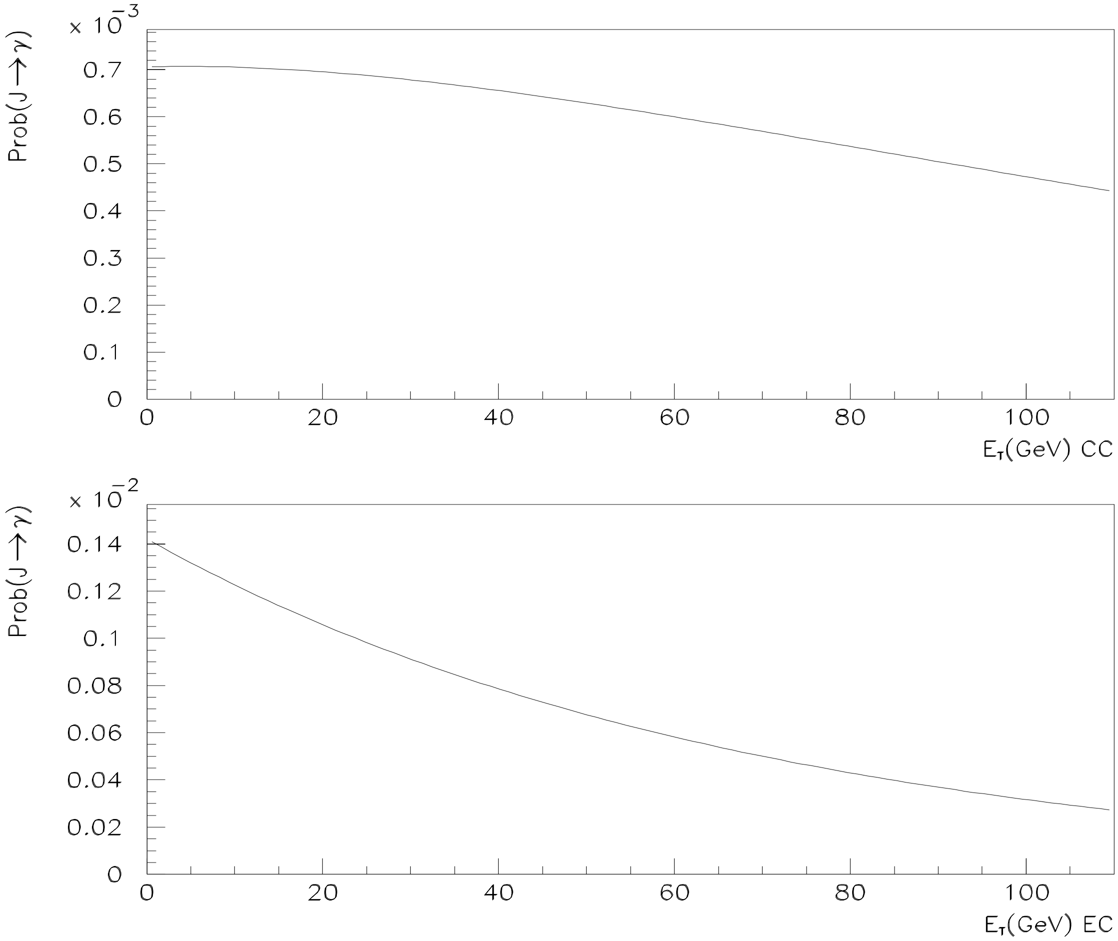

Figure 6.2: The final (jet$\rightarrow \gamma$) fake rates after direct photon subtraction. The difference in shapes is due to the positive (CC) and negative (EC) slopes of the fake rates before photon subtraction.

function of E_T by the 'photon fraction'; this function gives the probability that a photon is a real photon and is given by:

$$\text{photon fraction} = 1 \; - \; [0.911 \times \exp(-0.0124 \times \mathrm{E_T})] \; \pm 25\% \tag{6.3}$$

The photon fraction is obtained from a study where one looks at the ratio of energy deposited in the 1st layer of the calorimeter and performs a statistical analysis to determine how often clusters are one or two photons, two photons being a signature for π_0's and η's [52, 53]. The probability of a jet not being a photon (photon fraction - 1) is multiplied by the E_T dependant fake rates to obtain the final prob(jet$\rightarrow\gamma$). The final fake rates are shown in Figure 6.2. The error on the background calculation is dominated by the error on the direct photon contamination. In the W plus jet sample, there contained 5634 jets in the CC and 2322 jets in the EC. The total QCD background as given by equation 6.1 is given below with the errors coming from the error on the photon fraction, the normalization factor, and the linear fit to the fake rate.

$$\text{QCD BKG} = 15.45 \pm 4.55 \text{ events.}$$

6.0.4 QCD Cross Check

A cross check was made on the QCD background calculation that is somewhat independent of the previous method. Since the background calculation involves measuring many factors to account for the difference between the triggers for the signal and background, an independent measurement is important. This method involves using the same trigger, MU_ELE, for both the background and the signal. Instead of measuring a fake probability for a jet to be misidentified as a photon, a new probability is defined as

$$(f^*) = \frac{\text{\# of good photons(passing all ID cuts)}}{\text{\# of jets which pass `ELE' portion of trigger}} \tag{6.4}$$

This fake rate represents how often a jet, which passes the electromagnetic portion of the MU_ELE trigger will be reconstructed as a good photon. Instead of having on the order of a million events, only a few hundred events will pass this criteria to be used for the fake rate. The new fake rate will be on the order of 10% instead of the order of 10^{-4} for the standard fake rate. The advantage of this technique is that is does not contain any of the normalization factors that the previous method does. The disadvantage is that it suffers greatly in statistics since the trigger requirement is imposed. The fake rates for the CC and the EC are shown in Figure 6.3.

The fake probabilities are fit to straight lines which seem to model the data reasonably well. For the CC, the fake probability is estimated to be $11.5 \pm 2.9\%$, while the EC gives $13.7 \pm 3.4\%$. The total background estimation from this method is given by

$$\text{bkg} = \sum_{CC,EC} (W\gamma \text{ events with no EM quality cuts} - \frac{\text{signal events}}{\varepsilon}) * f^* \tag{6.5}$$

where f^* is the new fake rate and ε is the efficiency of the χ^2 and isolation cuts.

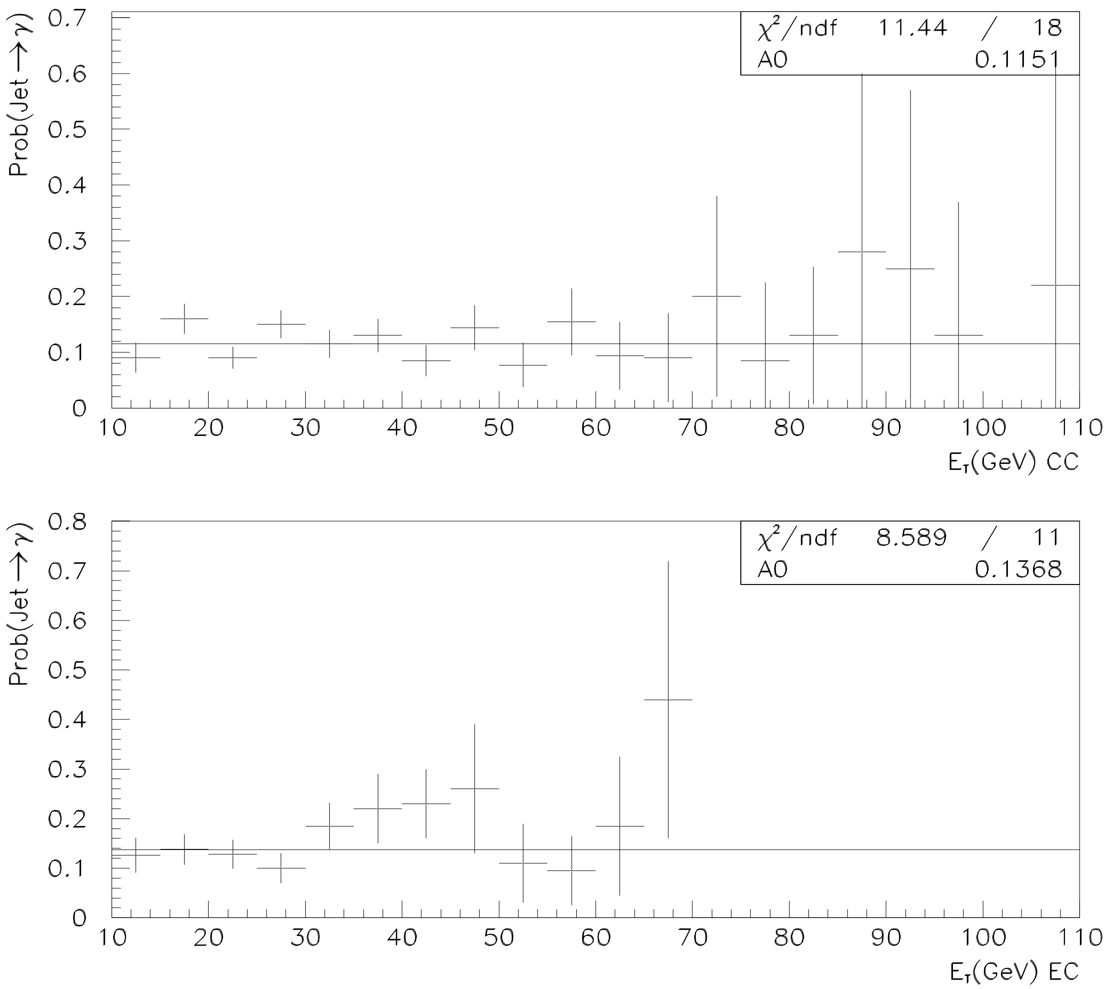

Figure 6.3: The fake probabilities for an electromagnetic object which passed the electromagnetic portion of the MU_ELE trigger for the CC and EC.

The $W\gamma$ events with no EM quality cuts include the sample of events that pass all the selection cuts except the χ^2 and isolation cuts. There were 163 events in the CC and 44 events in the EC. This background calculation is similar to the standard method, but since this background sample contains about 10^3 fewer events, the signal must be directly subtracted from the background sample since it would contribute significantly to the total background. Thus the sample used to calculate the background is the $W\gamma$ candidates with no χ^2 and isolation cuts minus the candidates which pass the χ^2 and isolation cuts. The number of signal events is corrected for the efficiency of the χ^2 and isolation cuts.

The total background from this method gives 17.1 $\pm$ 4.3 events which is consistent with the standard method which gives 15.45 $\pm$ 4.55 events.

6.0.5 $Z\gamma$

Another significant background is the process $Z\gamma \rightarrow \mu\mu\gamma$ where one muon is not reconstructed and fakes $\not\!\!E_T$ in the event. Like the QCD background, the $Z\gamma$ background is a fake background; but the $Z\gamma$ background must be computed from Monte Carlo since there is insufficient data for this process. The $Z\gamma$ Monte Carlo was also provided by Baur and Berger and was run through the same complete detector simulation as was the $W\gamma$ Monte Carlo. The standard method to calculate this background is to apply the $W\gamma$ selection criteria to the $Z\gamma$ Monte Carlo and remove events where a second muon is found. This method gives poor rejection and the $Z\gamma$ channel contributes $\approx$ 35% to the signal. This poor rejection occurs because a muon fails to be reconstructed or pass ID cuts a significant amount of the time, and the $Z\gamma$ cross section is about 1/3 that of $W\gamma$.

The sensitivity for finding the lost muon is increased by using the MTC (Muon Tracking in Calorimeter) package [44]. The MTC tools are very important for reducing the $Z\gamma \rightarrow \mu\mu\gamma$ background. The MTC package relies on the good segmentation and hermeticity of the calorimeter to find and track muons. This package uses information about how muon interact in the calorimeter to distinguish them from other particles. As mentioned in the event selection section, the computed MTC variables are normally used as muon ID variables; that is, once a muon is found, the relevant MTC quantities are calculated for that muon. In this case a lost muon must be found to reduce the background, so MTC is used in full tracking mode, independent of any muon information. The entire hadronic calorimeter is scanned for muon candidates independent of any information in the muon system. Once all the candidates are found (determined by requiring a loose set of cuts), the track verification is run on all candidate tracks to compute the relevant MTC quantities which are then used for analysis.

Using only the information from the MTC package, the results have a significant improvement over the standard method of rejecting events with two muons present. A 30% reduction in the background can be achieved with an efficiency of about 90% for the signal. A larger improvement can be made by using the topology of $Z\gamma$ events to reduce the phase space in which one looks for the lost muon. The two muons from the Z are produced back to back in ϕ, in the rest frame of the Z. When one muon is lost this becomes a source of $\not\!\!E_T$ which fakes the $W\gamma$ signal. With the addition of jets and the $Z\gamma$ system boosted, the lost muon should be located around the ϕ of the $\not\!\!E_T$. Restricting the search for the lost muon within a small band around the ϕ of the $\not\!\!E_T$, the phase space is sufficiently decreased so the MTC ID cuts can be loosened. With looser ID cuts more muons are found, and there is a larger rejection of the background.

Figure 6.4 shows the difference in ϕ between the $\not\!\!E_T$ and all the MTC tracks found in the event. Three different data samples are shown: $Z\gamma \to \mu\mu\gamma$, $Z \to \mu\mu$, and $W\gamma \to \mu\nu\gamma$. The Z$\gamma \to \mu\mu\gamma$ sample shown is a Monte Carlo sample that passes all the selection cuts for $W\gamma$ and has events removed where a second muon is found (p_T of muon > 10 GeV/c). The $Z \to \mu\mu$ sample is real data which was used for the efficiency, since one doesn't expect any additional muons in this sample. The $W\gamma \to \mu\nu\gamma$ sample is a Monte Carlo sample that shows the relevant distributions for the signal. For the $Z\gamma$ data sample, there is a distinctive peak at zero as one expects from the lost muon and also around π where the reconstructed muon is found. The $Z \to \mu\mu$ data shows two pronounced peaks also at zero and π being the two reconstructed muons in the event. The $W\gamma$ data shows a peak at π where the one muon is found opposite the $\not\!\!E_T$.

As shown in Figure 6.4, Many MTC tracks are pointing to existing muons.

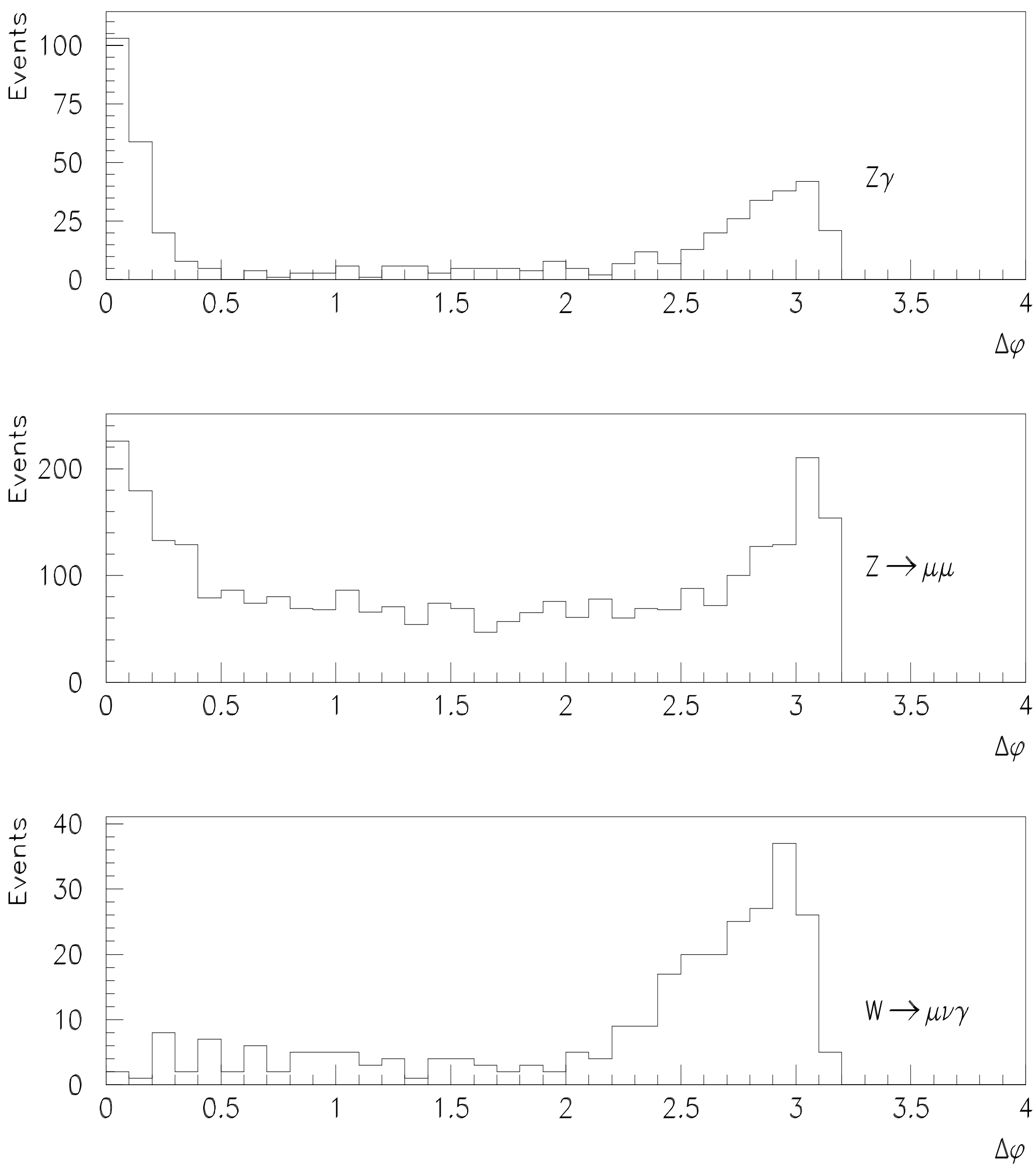

Figure 6.4: The difference in ϕ between the $\not\!\!E_T$ and the MTC track, for all MTC tracks, $Z\gamma \rightarrow \mu\mu\gamma$ (with one muon found), $Z \rightarrow \mu\mu$, and $W\gamma \rightarrow \mu\nu\gamma$ data.

In order for an event to be rejected as a possible $Z\gamma$ event, the MTC track must not match to any existing particle. For a given MTC track, every muon and jet is checked to see if a match can be found. If a muon or jet are within ΔR(MTC track $-\mu$, jet) ≤ 0.4 then the MTC track is thrown out as a possible new muon. Figure 6.5 shows the same $\Delta\phi$ distribution for the three data samples, calculated for only unmatched MTC tracks. This figure illustrates the rejection power of this technique. Most of the $Z\gamma$ MTC tracks are around $\Delta\phi$ of zero radians while the events at $\Delta\phi = \pi$ are removed. The $Z \rightarrow \mu\mu$ data shows a fairly flat distribution as one expects since the two MTC tracks matching the muons are removed. Similarly the $W\gamma \rightarrow \mu\nu\gamma$ sample is flat after the MTC track matching the existing muon is removed. By making a cut close to zero for the $\Delta\phi$, the $Z\gamma$ background can be significantly reduced while keeping high efficiency for the signal.

Figure 6.5 shows the MTC tracks with no quality cuts except some minimal cuts to perform the search for tracks. To further clean up the sample, additional quality cuts on the MTC tracks can be applied to increase the efficiency of this procedure. In addition to the $\Delta\phi$ cut, two other quantities are useful to maintain high efficiency. The hadronic fraction (Hfract) is the fraction of layers where energy was deposited by the muon in the hadronic calorimeter (also described in event selection section). This variable is usually equal to 1 for muons since they penetrate the entire calorimeter, while jets and electrons/photons are contained. The energy along the MTC track (Etrack) is also used. This is the total energy of all the cells in the calorimeter along the

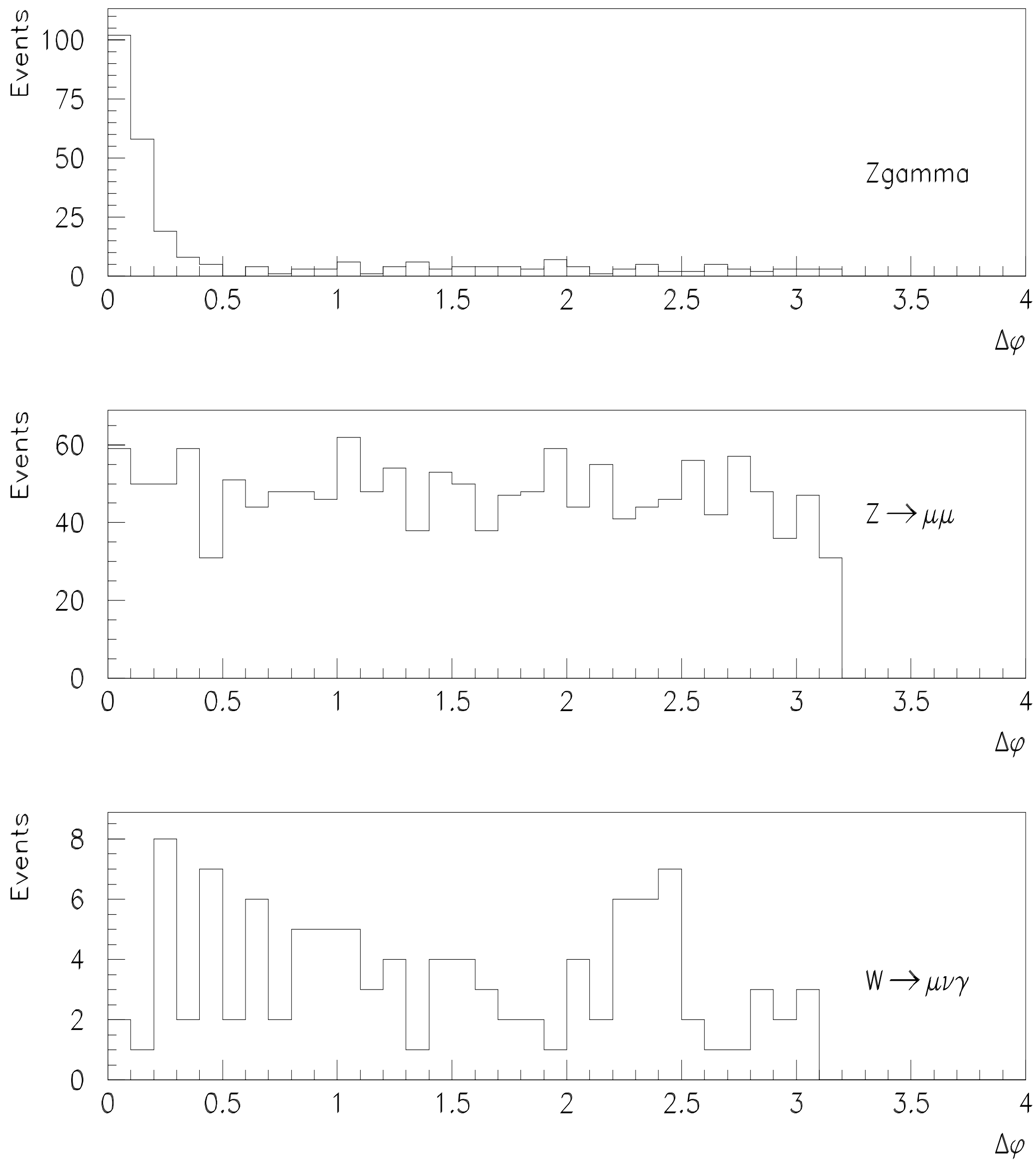

Figure 6.5: The difference in ϕ between the $\not{E}_T$ and the MTC track for tracks that do not match an existing muon or jet.

MTC track. The distributions of these variables are shown in Figures 6.6 and 6.7; we placed cuts of 0.8 GeV for Etrack and 0.8 for Hfract. Cutting loosely on Hfract and Etrack helps keep high rejection while rejecting hot cells and noise in the calorimeter to keep the efficiency high. For the Hfract cut of 0.8, the $Z\gamma$ data is almost all removed while for the $Z \rightarrow \mu\mu$ data a significant portion is thrown out by this cut. Calorimeter noise and hot cells dominate the low values for Hfract. For the Etrack variable, a good muon should deposit a reasonable (> 1 GeV) amount of energy while hot cells and noise contribute less energy. The $Z\gamma$ data shows most of the muons deposit more than 0.8 GeV of energy, while the $Z \rightarrow \mu\mu$ data has a large portion dominated by noise, which peaks at low values for Etrack. One additional cut is added, an η cut on the MTC track. This cut is applied since beyond η of 2.7 the number of MTC tracks increases dramatically due to the higher track multiplicity, while the $Z\gamma$ signal drops off rapidly for large η. An event which is tagged as a $Z\gamma$ candidate is shown in Figure 6.8. This figure 6.8 shows the top view of the DØ detector which contains a reconstructed muon with an associated matching MTC track. The ϕ view represented in the figure is shown in the lower left-hand corner. Figure 6.9 is the side view of the same event, showing a blowup view of the MTC track that is in the same direction as the $\not\!\!E_T$. There are many hits in the A-layer muon chambers, indicating that a muon penetrated this area. Also the track points in the direction of a crack in the outer layers, which explains why the muon was not reconstructed. With all of the above cuts applied to the MTC tracks, the following results are obtained.

Rejection factor = 2.9 ± 0.2 Efficiency = (93.0 ± 2.0) %

The rejection factor of 2.9 is determined from the $Z\gamma$ Monte Carlo; this being the factor by which the background is reduced by applying the MTC cuts. The efficiency, as was stated, is determined from the $Z \rightarrow \mu\mu$ data. 93% of these events survive the MTC cuts.

Now that the cuts are optimized for the signal, the $Z\gamma$ background can be calculated. Two methods are used to calculate the $Z\gamma$ background. Both methods are from Monte Carlo and are very correlated. The first method is a direct Monte Carlo calculation given by:

$$\text{(6.6)} \quad \mathrm{Z}\gamma \text{ bkg} = \text{Ratio}(\mathrm{Z}\gamma \text{ events passing } \mathrm{W}\gamma \text{ selection}) \times \text{Lum} \times \sigma \times \varepsilon$$

where the ratio of $Z\gamma$ Monte Carlo events passing $W\gamma$ event selection accounts for all the kinematic and geometric acceptance. σ is the cross section for the $Z\gamma$ Monte Carlo generated events. ε is the efficiency for all the muon and photon ID cuts as well as the MTC efficiency. This method gives a total background of 5.13 ± 0.32 events. The second method used was to find the percentage of $Z\gamma$ events in the $W\gamma$ signal by looking at the ratio of both the Monte Carlos. By applying the $W\gamma$ selction to both the $Z\gamma$ and $W\gamma$ Monte Carlo samples and normalizing to the number of events generated, the fraction of $Z\gamma$ events in the $W\gamma$ sample can be computed. Using this method gives 13.68 ± 2.0 % for the fraction of $Z\gamma$ events in the $W\gamma$ signal giving a bac kground of 4.9 ± 0.1 events. The total $Z\gamma$ background = 5.0 ± 0.4 events

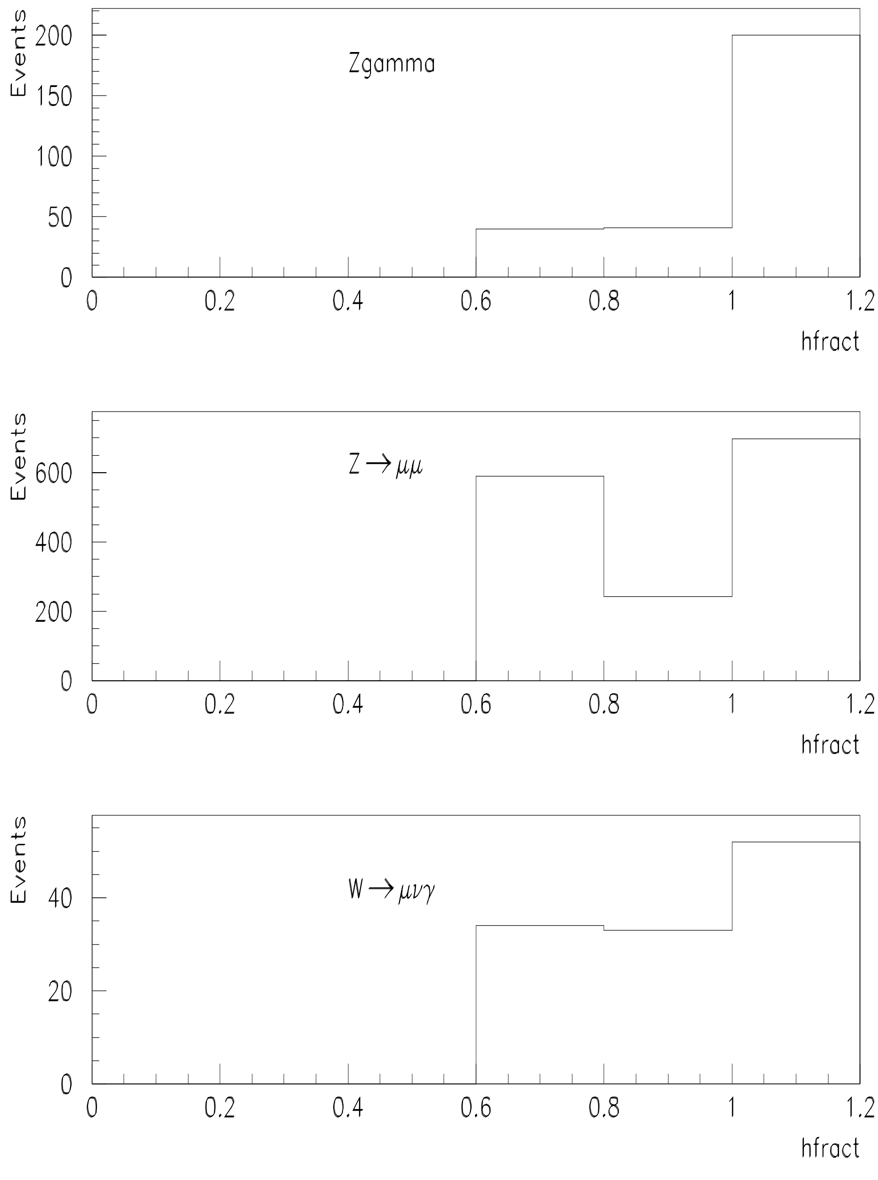

Figure 6.6: The variable Hfract (fraction of hadronic layers hit in calorimeter) for all unmatched MTC tracks. A cut of Hfract ≥ 0.8 is applied showing good efficiency for rejecting $Z\gamma$.

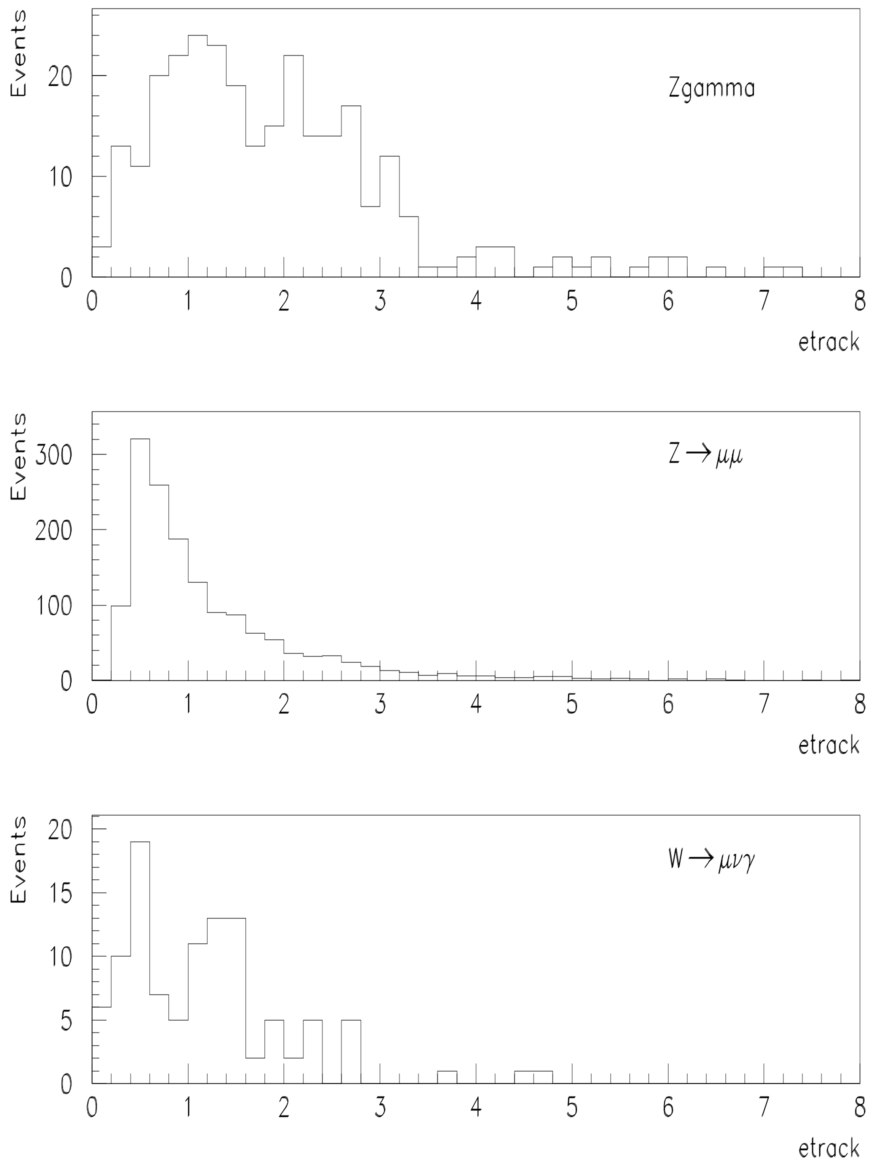

Figure 6.7: The variable Etrack (sum of energy along road in calorimeter) for all unmatched MTC tracks. A cut of Etrack $\geq$ 0.8 GeV is applied.

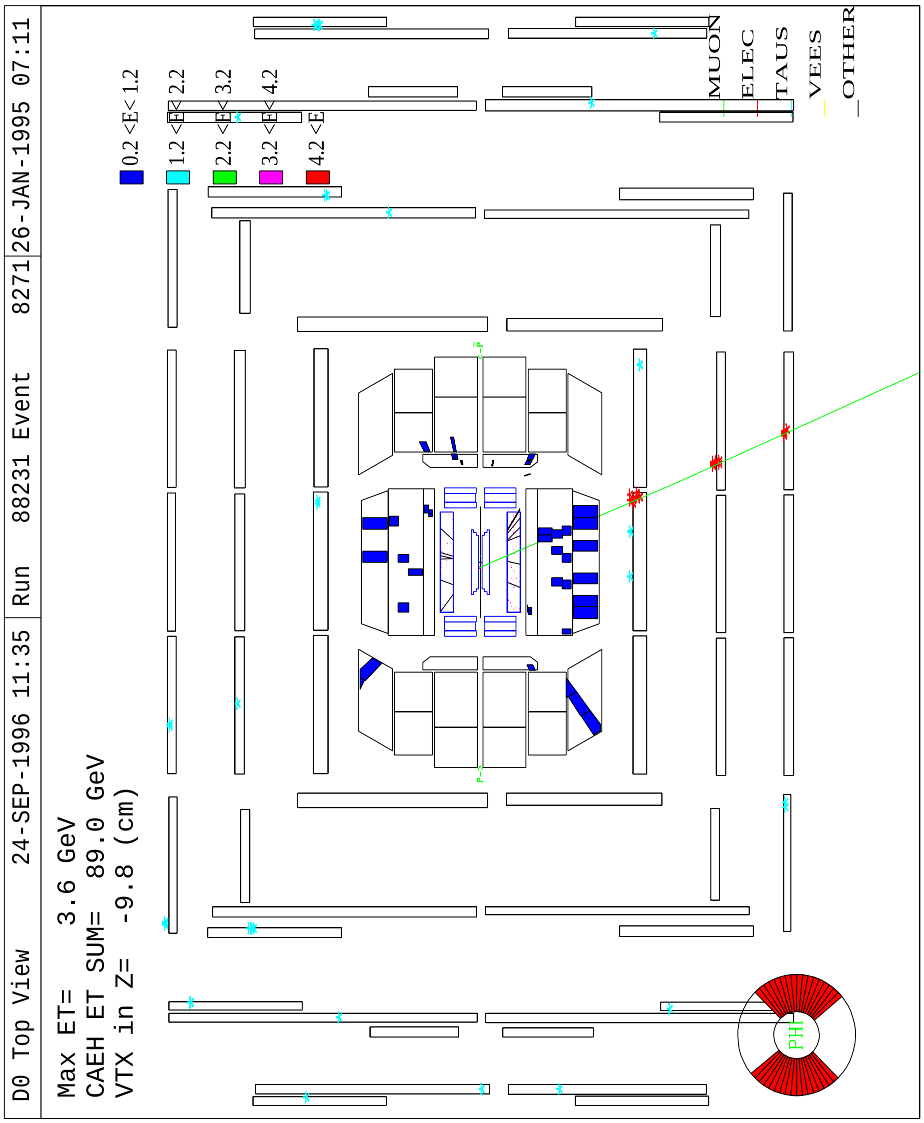

Figure 6.8: An event display of a $Z\gamma$ candidate. This view shows the reconstructed muon with its associated MTC track.

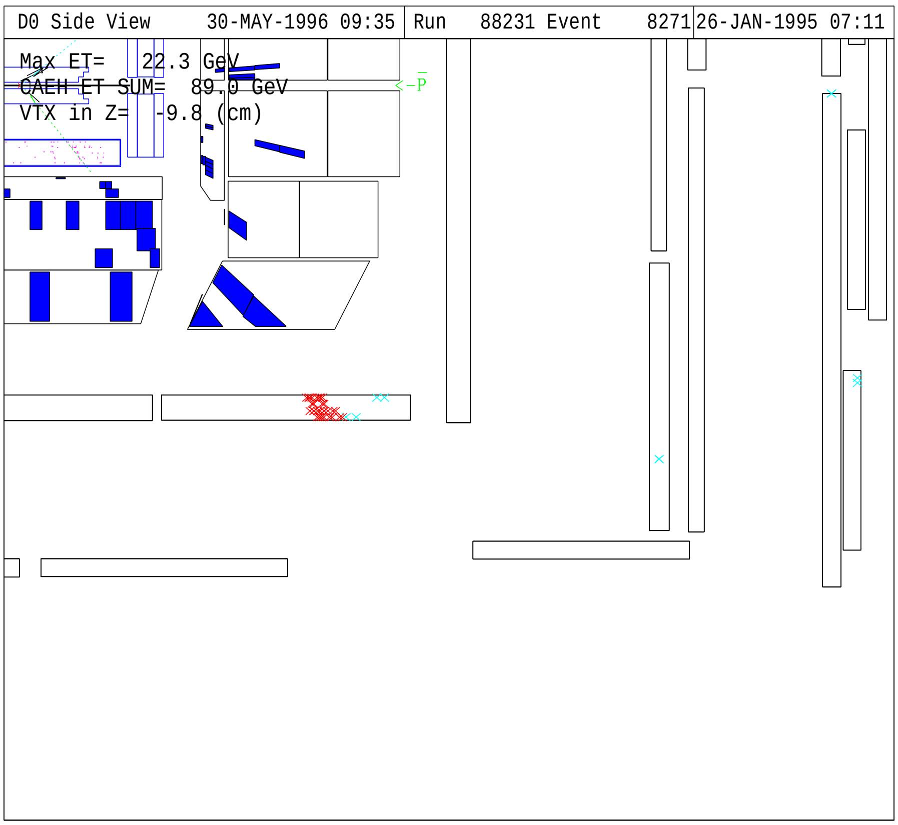

Figure 6.9: Event display showing the blowup view of the area where the lost muon is found from an MTC track. The MTC track points to an area where A-layer hits are present, indicating a muon.

(average of two methods). The error on the $Z\gamma$ background does not come from the average of the two methods, but rather is a conservative error to account for the difference between the two methods. Also the errors from the two different methods are highly correlated.

6.0.6 Other Backgrounds

The QCD and $Z\gamma$ fake backgrounds are the two most significant backgrounds to the $W\gamma$ signal. There are a few small but non-negligible physics backgrounds that have the same final state as the $W\gamma \rightarrow \mu\nu\gamma$ signal. These are shown below.

$W\gamma \rightarrow \tau\gamma \rightarrow \mu\nu\gamma$

A full $W\gamma \rightarrow \tau\gamma$ Monte Carlo doesn't exist so this background is calculated by looking at the ratio of the numbers of $W \rightarrow \tau\nu \rightarrow \mu\nu$ and $W \rightarrow \mu\nu$ events which pass the selection criteria. This method should be valid since W and $W\gamma$ production have similar kinematic properties. This procedure gives the background as a percentage of the signal.

$$\begin{aligned} W\gamma \rightarrow \tau\gamma \rightarrow \mu\nu\gamma = & \quad (5.3 \pm 0.8)\% \\ = & \quad 1.6 \pm 0.3 \text{ events} \end{aligned}$$

Top and WW

Two additional sources of backgrounds were studied, top quark and WW production. These backgrounds contribute a very small amount but were nonetheless calculated for completeness. The acceptances for both processes were measured from Monte Carlo while the efficiencies were calculated from the data. These two backgrounds are shown below.

Top $= 0.396 \pm .246$ events

$WW = 0.478 \pm .048$ events

6.0.7 Summary of signal and backgrounds

A summary of all the backgrounds and the observed number of events is shown in Table 6.2. The asymmetric errors on the final signal are the Poisson errors that arise with a given background [54].

Table 6.2: Summary of signal and backgrounds

	$\mu\nu\gamma$
Luminosity	72.9 pb^{-1}
Backgrounds	
QCD	15.5 ± 4.5
$Z\gamma$	5.0 ± 0.4
$W(\tau\nu)$	1.6 ± 0.3
other(Top,WW)	0.87 ± 0.25
Total BKG	23.0 ± 4.6
# Observed	58
Total Signal	$35.0^{+8.6}_{-7.6}$

Chapter 7

Results

This chapter describes in detail the experimental results of this study of $W\gamma \rightarrow \mu\nu\gamma$ events, including the cross section measurement and the calculation of the limits on the anomalous couplings. As briefly mentioned in the theoretical section, two different methods are used to calculate the coupling limits: a fit to the total production cross section and a fit to the differential cross section for the transverse energy of the photon. By comparing the experimental measurements to the predictions of the theory with different anomalous couplings, quantitative measurements of the limits of these couplings are made. The fast 'parametric' Monte Carlo that is used to calculate these limits is described. Finally, results from this analysis of $W\gamma \rightarrow \mu\nu\gamma$ events are combined with the results from the $W\gamma \rightarrow e\nu\gamma$ analysis to produced combined limits which are significantly tighter than those obtained from only the $W\gamma \rightarrow \mu\nu\gamma$ analysis.

7.1 Cross Section and Comparison with the Standard Model

Before calculating limits on the $WW\gamma$ couplings, it is useful to compare the observed data to the predictions of the Standard Model. Some important kinematic distributions are shown in Figure 7.1.

The three distributions show the selected $W\gamma \to e\nu\gamma$ candidate events (58 events) as data points, the background as the shaded region, and the background plus the Monte Carlo (based on the Standard Model) prediction as the histogram. As was discussed in detail in the section on backgrounds, QCD processes provides the single largest source of background. The p_T^γ distribution shows very good agreement with the Standard Model; there exist no significant excess of events at high E_T. The muon-photon separation $\Delta R(\mu - \gamma)$ and the cluster transverse mass distribution $M_T(W,\gamma)$ also show good agreement with the Standard Model. The events with a small $\Delta R(\mu - \gamma)$ separation tend to be from radiative decays while the production events tend to peak at around a $\Delta R(\mu - \gamma)$ of π. The cluster transverse mass distribution peaks at around 80 GeV/c^2 as is expected from radiative decay processes.

The measured signal (number of observed candidates minus the total number of estimated background events) is found to be

$$34.7^{+8.6}_{-7.6} \pm 5.44\ (syst)\ \pm 4.2\ (lum) \text{ events;}$$

where the first asymmetric error is the 68.2% confidence level interval (1σ)

given by Poisson statistics and the second error represents the total experimental systematic error, consisting of the uncertainties in the trigger and offline efficiency, acceptances, and the backgrounds. The uncertainties in the backgrounds dominate the total systematic error. The error due to luminosity is shown separately since this error is the same for all analyses at DØ. All the systematic errors will be discussed in more detail later in this chapter. The Standard Model prediction using the Baur and Berger Monte Carlo is 31.50 ± 2.52 events. The measured signal is in good agreement with this prediction.

The measured number of events can be expressed in terms of a cross section. The cross section for $W\gamma$ production times the $W \rightarrow \mu\nu$ branching ratio is given by

$$\sigma(p\overline{p} \rightarrow W\gamma) \times \mathrm{BR}(W \rightarrow \mu\nu) = \frac{\text{\# of observed W}\gamma\rightarrow\mu\nu\gamma\text{ events}}{\varepsilon\mathcal{L}}$$

$$= 13.1^{+3.2}_{-2.8} \pm 2.11\ (syst)\ \pm 1.6\ (lum)\ \mathrm{pb};$$

where ε is the overall efficiency and $\mathcal{L}$ is the total integrated luminosity. The overall efficiency (ε) is the efficiency calculated in chapter 5; this represents all the selection efficiencies and acceptances. As shown in the predicted number of events, the first asymmetric error is the 1σ statistical Poisson error. The statistical error is the largest error indicating that this analysis is still limited by statistics. The systematic errors are also quite large but are also statistics limited, since with more data, the backgrounds become better modeled and the efficiencies are more constrained.

The Standard Model prediction using the MRSD$-'$ structure function gives 12.5 ± 1.0 pb. The overall theoretical uncertainty is derived from uncertainties in the structure function choice, the structure function scale, and the p_T kick of the $W\gamma$ system. The method used to calculate the theoretical error is shown in section 7.3.1. There is good agreement between the measured cross section and the predicted value from the Standard Model. As there exists no striking evidence for the presence of anomalous couplings, the next step is to derive quantitative limits on these anomalous couplings. This analysis is based on a large number of data sets generated for different values of the couplings. A fast 'parametric' Monte Carlo was used to generate this data; this Monte Carlo is described in the next section.

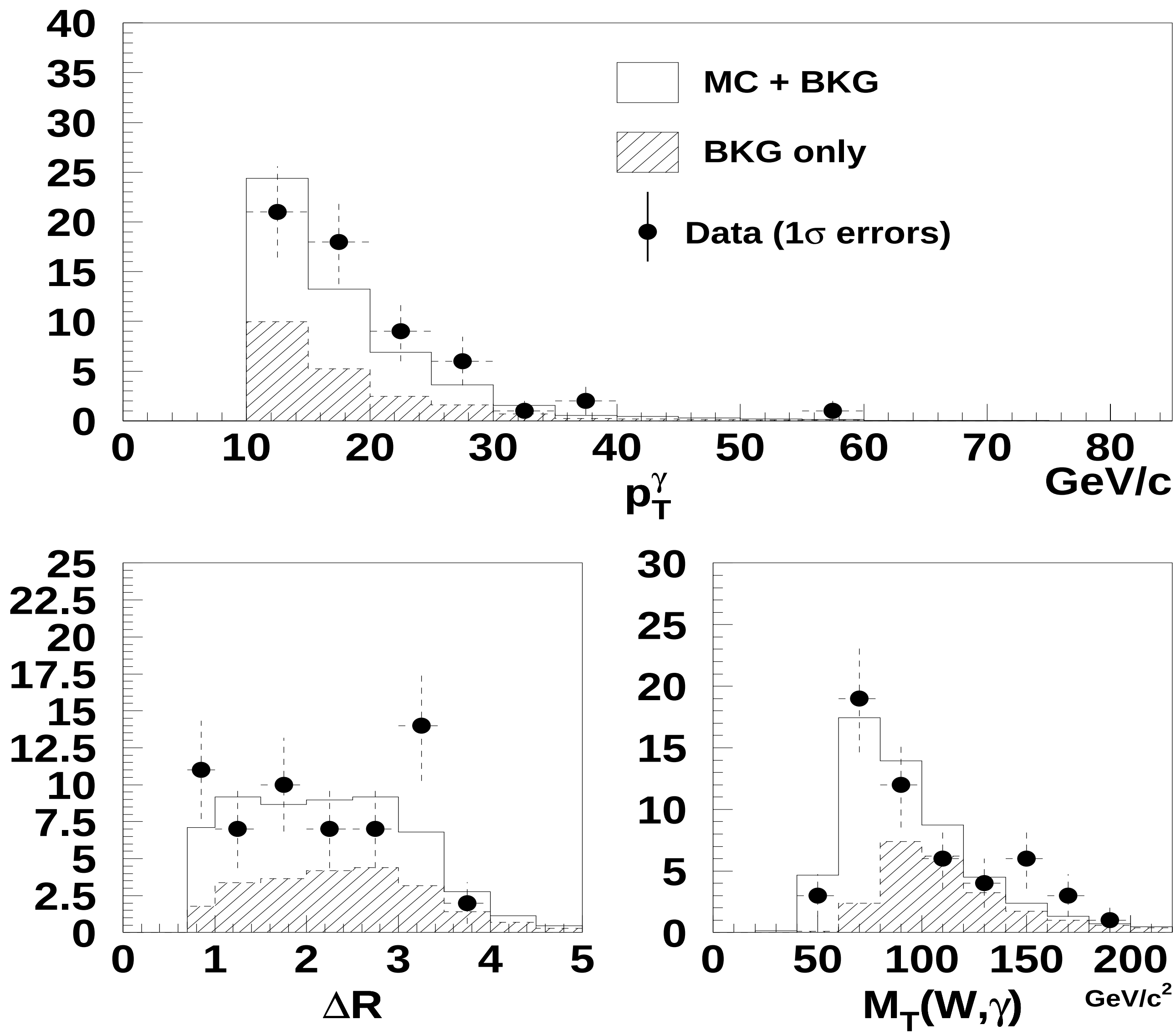

Figure 7.1: Event distributions for selected $W\gamma \rightarrow \mu\nu\gamma$ candidate events (data points), background (shaded region), and background plus Monte Carlo (solid histogram). The variables shown are the photon transverse momentum P_T^γ, the separation ΔR between the (μ, γ), and the transverse mass M_T of the W, γ system.

7.2 Fast Monte Carlo Simulation

To determine confidence level limits on the anomalous couplings and to determine various systematic errors (for example, Structure Function dependence), a large number of Monte Carlo experiments must be performed. Since a full detector simulation such a D0GEANT [55], which tracks all particles through a detailed geometry, requires a very large amount of computation, a parametric simulation has been developed to enable the necessary acceptances and efficiencies to be quickly calculated. A further advantage of this parametric simulation is that real data from the collider run is used to determine all the smearings (spreading simulated measurements with the experimental results) and corrections for underlying events (including data to model the effect of multiple interactions). A full detector simulation such as D0GEANT is necessary for a few studies such as the modeling the details of material and cracks in the detector. On the other hand, the parametric simulation should give the most accurate information about the environment (underlying energy, $\not\!\!E_T$ energy resolution smearing) of the interactions. A complete description of the fast Monte Carlo is given in [56].

The fast Monte Carlo takes as input, a list of four vectors generated from some type of event generator. In this case, the event generator is the Monte Carlo provided by Baur and Zeppenfield [10]. A list of four vectors is produced for every particle (W, μ, ν, γ), and these four vectors are then input in the fast Monte Carlo where the modeling of the detector begins. Depending on the type of particle, the appropriate smearing is performed to model correctly the detector response. All smearing parameters and resolutions are determined from data. Before smearing occurs, the kinematics are modified to reflect higher-order processes by including a hadronic recoil. This hadronic recoil (E_T^{had}) is determined from data by using the measured p_T spectrum from the $Z \rightarrow ee$ data sample, p_T^Z. The system is then boosted opposite the hadronic recoil, ready to be smeared by the detector resolutions.

7.2.1 Data Smearing

This section describes all the smearing that occurs in the Monte Carlo in order to correctly simulate the detector response.

Electron/Photon Smearing

Electron and photon energies are smeared using the measured resolutions from the DØ electromagnetic calorimeter. The resolution is parameterized as

$$(\sigma/E)^2 = C^2 + S^2/E + N^2/E^2 \tag{7.1}$$

where C, S, and N are respectively the constant term, sampling term, and noise term. The numerical values are given in Table 7.1.

Muon Momentum Smearing

The muon momentum resolution can be parameterized as

$$(\frac{\sigma_{(1/p)}}{(1/p)})^2 = (a(p-p_0)/p)^2 + (bp)^2 \tag{7.2}$$

where p is the momentum measured in GeV/c. The constants are also given in Table 7.1.

Jet/Hadronic Energy Smearing

The jet energies are also smeared using the measured resolutions from the DØ hadronic calorimeter [57]. The energies of partons are first scaled by a hadronic response factor (R_{Had}), then smeared with the resolution parameterized as

$$(\sigma/E)^2 = C^2 + S^2/E + N^2/E^2 \tag{7.3}$$

where as before C, S, and N are respectively the constant term, sampling term, and noise term. These valuse are shown in Table 7.1.

Table 7.1: Smearing parameters for fast Monte Carlo

Constant term in CC EM energy resolution	0.017
Sampling term in CC EM energy resolution	0.140
Noise term in CC EM energy resolution	0.490
Constant term in EC EM energy resolution	0.0094
Sampling term in EC EM energy resolution	0.157
Noise term in EC EM energy resolution	1.140
Constant term in hadronic jet energy resolution	0.04
Sampling term in hadronic jet energy resolution	0.80
Noise term in hadronic jet energy resolution	0.00
Constant term in hadronic jet energy resolution	0.04
Sampling term in hadronic jet energy resolution	0.80
Noise term in hadronic jet energy resolution	0.00
Hadronic ET response factor	0.83
Constant term in hadronic ET resolution	0.00
Sampling term in hadronic ET resolution	0.56
Noise term in hadronic ET resolution	0.00
Muon Resolution term A	0.18
Muon Resolution term B	0.003
Muon Resolution term P_0	2.0

Missing Transverse Energy Calculation

The $\not\!\!E_T$ is computed in a few steps. First the quantities of each particle, such as the energy and momentum, are smeared according to the formulas given above. Then the hadronic recoil energy is also smeared according to the calorimeter resolutions. The total transverse energy is then summed and the $\not\!\!E_T$ is set equal to the energy imbalance. Finally energy is added to the event to account for the underlying event. The underlying event is due to the contribution from the breakup of the proton and antiproton in the interaction. The quarks not involved in the interaction (spectator quarks) deposit energy in the detector. The underlying event energy was calculated from real min-bias data and is added to the event in a random direction. The total $\vec{\not\!\!E}_T$ vector is given as

$$\vec{\not\!\!E}_T = -(\vec{E}_T^{UE} + \vec{E}_T^{\mu,e,\gamma,j} + \vec{E}_T^{Had}) \tag{7.4}$$

where $\vec{E}_T^{UE}$ is the contribution from the underlying event.

The vertex position is smeared with a Gaussian distribution as was determined from the observed vertex distribution of the data. The four-vectors of all the particles from the Baur generator are converted into detector geometry variables (E_T, η, ϕ) and compared to selection criteria, to determine if a given event passes the kinematic and fiducial requirements. All the efficiencies measured from the data are put into the Monte Carlo to model the particle ID cuts. The kinematic acceptance and particle ID efficiencies are determined using a random hit-or-miss method. A random number is generated and examined to see if it falls within a range for a given efficiency; thus determining if a given event passes all requirements. Using this method, the correct cross sections can be calculated and used for the calculation of the confidence level limits on the anomalous couplings. With this parametric Monte Carlo, a large number of Monte Carlo experiments can be performed in a relatively short time. The amount of phase space that needs to probed would not be possible using D0GEANT. Many other physics analyses are using this type of Monte Carlo since the CPU time is significantly faster and the efficiencies used are derived from real collider data.

7.3 Limits on the Anomalous Couplings

Since the measured number of events is in good agreement with the theoretically predicted number of events and there does not appear to be a signature for anomalous couplings, one can now make a quantitative measurement of the limits on the anomalous couplings. This section will go into the details of calculating these limits. Two methods are used to obtain these anomalous coupling limits: a fit to the total cross section, and a binned likelihood fit to the p_T^γ distribution. All the systematic errors that are relevant to this calculation are shown and discussed. Finally this analysis is combined with the similar analysis for the channel $W\gamma \rightarrow e\nu\gamma$ to produce the tightest possible limits on the anomalous couplings from our $W\gamma$ data. The limits obtained here, from DØ, are compared with limits from other high energy experiments.

7.3.1 Limits from the Total Cross Section Measurement

As was mentioned in the theoretical discussion, one way the anomalous couplings manifest themselves is an increase in the total production cross section. From the observed number of events, quantitative limits can be calculated on the presence of anomalous couplings. The total production cross section can be expressed as:

$$\sigma(\Delta\kappa, \lambda) = \sigma_{SM} + a\Delta\kappa + b\Delta\kappa^2 + c\lambda + d\lambda^2 + e\Delta\kappa\lambda, \tag{7.5}$$

where σ_{SM} is the Standard Model cross section for no anomalous couplings. The CP-violating parameters $\Delta\tilde{\kappa}$ and $\tilde{\lambda}$ can also be expressed in this form. The determination of $\Delta\tilde{\kappa}$ and $\tilde{\lambda}$ is similar to $\Delta\kappa$ and λ and only the results will be shown.

An upper limit σ^β on the production cross section at a given confidence level (CL) β from the observed number of events can be translated into a CL limit of the anomalous couplings ($\Delta\kappa$,λ) by solving the equation:

$$\sigma(\Delta\kappa, \lambda) = \sigma^\beta \tag{7.6}$$

The contour defined by this equation is an ellipse in the ($\Delta\kappa$,λ) plane and thus the limits are defined by a finite area in this plane. By counting the number of $W\gamma$ candidates produced, limits can be set on the anomalous couplings.

A Bayesian approach is used to set CL limits on the cross section as a function of the anomalous couplings ($\Delta\kappa$,λ). For small statistics, the Poisson probability is used to determine the expected number of events. This probability for observing n events with an expectation value μ is given by:

$$P = \frac{e^{-\mu}\mu^n}{n!} \tag{7.7}$$

The expected number of events μ for an experiment is given by the following relation

$$\mu = b + \mathcal{L}\varepsilon\sigma(\Delta\kappa, \lambda) \tag{7.8}$$

where b is the measured background, $\mathcal{L}$ is the total integrated luminosity, and ε is the total efficiency times acceptance for the signal.

In setting CL limits, one is only interested in the values of the anomalous couplings, $\Delta\kappa$ and λ. The expectation value μ also contains terms for the total background, efficiency, and the luminosity. These items can be referred to as 'nuisance parameters' since they decrease the sensitivity of the CL limits on anomalous couplings. To take into account the errors on these measured values, they are folded into the likelihood function, giving a new likelihood function given below.

$$P = \int \mathcal{G}_{\mathcal{L}}\, d\mathcal{L} \int \mathcal{G}_b\, db \int \mathcal{G}_\varepsilon\, d\varepsilon\, \frac{e^{-(b+\mathcal{L}\varepsilon\sigma(\Delta\kappa,\lambda))}(b + \mathcal{L}\varepsilon\sigma(\Delta\kappa, \lambda))^n}{n!}. \tag{7.9}$$

The $\mathcal{G}$ stands for the appropriate Gaussian distribution for the nuisance parameters. By folding in the nuisance parameters as Gaussian distributions, the measured uncertainties are taken into account. The Gaussian distributions for each nuisance parameter are represented with a mean $\mu = 1$ and a Standard rms deviation σ as:

$$\mathcal{G}_x = \frac{1}{\sigma_x\sqrt{2\pi}} \exp \frac{-(x-\mu)^2}{2\sigma_x^2}. \tag{7.10}$$

where the standard rms deviation is the 1σ error measured from the data. This method of folding in the uncertainties is only valid if the errors are uncorrelated. This method is also useful when combining results from different channels which share some common systematics. More will be discussed on this subject when the results from the electron channel are combined.

The errors are grouped into 3 categories which are all uncorrelated. The errors for efficiencies include all the errors on particle ID and trigger efficiencies. The combined error for all backgrounds is completely dominated by the error on the QCD background. The efficiencies were discussed in chapter 5 and the backgrounds were discussed in chapter 6. A table of all the errors is given in Table 7.2.

Table 7.2: Relative uncertainties used in the likelihood fit

Muon ID/trigger efficiencies	6.8%
photon ID/trigger	3.6%
conversion probability	5.0%
random track overlap	0.5%
luminosity uncertainty	12.0%
choice of structure functions	6.0%
structure function scale	1.0%
$P_t^W -$ kick to the $W\gamma$ system	3.9%
Total background	28.0 %

The Muon ID/trigger efficiency error is due to the statistics of the samples used and the systematics arising mainly from using the 'musmeared' Monte Carlo. The photon ID/trigger error is determined by the trigger turn-on curve used to model the E_T dependant trigger efficiency. The error from the conversion probability of the photon is a conservative error that comes from the knowledge of the amount of material in the detector. The error on the random track overlap rate is from the statistical error from the data sample used. The luminosity uncertainty is derived from the error on the total inelastic cross section for $\overline{p}p$ interactions and the experimental measured error on the interaction rate [25]. Two theoretical errors arise from the choice of structure functions used and the scale at which they are used. Figure 7.2 shows the variation of the cross section for different structure functions [47].

The central value of the cross section shown in Figure 7.2 uses the $MRSD-'$ structure function. This structure function was chosen because it has the best agreement with data pertaining to the W boson decay asymmetry. The structure functions are grouped into two categories, leading order (LO) and next-to-leading order (NLO). Twenty one different structure functions were used to study the dependence of the cross section on the choice of structure functions. The (LO) structure functions give a systematically lower result for the cross section compared to the (NLO) results. An error of 6% is used for the structure function uncertainty which, as seen from Figure 7.2 is rather conservative.

One more theoretical uncertainty arises from the scale used in the structure function calculations. By varying the value of $Q^2 = \hat{s}$ (momentum transfer) from $\hat{s}/2$ to $2\hat{s}$ the cross section was observed to change by 1%. A final theoretical uncertainty comes from the P_t^W kick to the $W\gamma$ system. Variations in the P_t^W kick result in cross section variations of 3.9%. The total systematic error from the experimental measurement, excluding the background error, is found by adding the errors in quadrature, giving 15.1%.

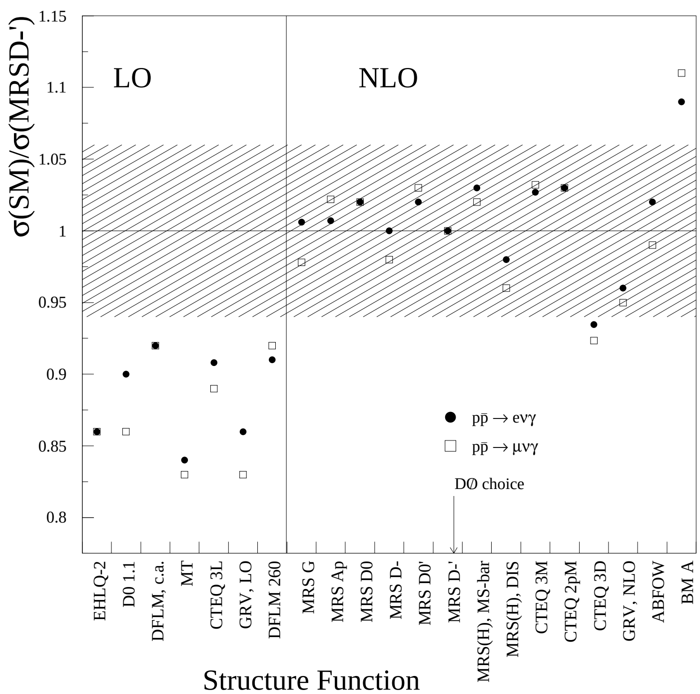

Figure 7.2: SM $W\gamma$ cross sections for different NLO and LO structure functions, normalized to the cross section with the $MRSD-'$ set. The band shows the 6% systematic uncertainty about the NL0 results. The cross sections from L0 structure functions are shown for comparison.

In calculating the CL limits on anomalous couplings, one background is treated differently than the other backgrounds, namely the process $W\gamma \rightarrow \tau\nu\gamma$. This background is treated separately because if anomalous couplings were present, this background would rise as does the signal. Instead of representing this source as a fixed background, this background was calculated as a percentage of the signal. By treating this background as proportional to the signal, its dependence on the anomalous couplings is correctly taken into account.

As mentioned earlier, a large amount of phase space is probed in order to generate CL limits. A grid of 17×17 (289) grid points was generated, where for each grid point the cross section is calculated for a given $\Delta\kappa$, λ. The grid space spans the region from -2.4 to 2.4 in both $\Delta\kappa$, λ. This region extends past the current limits measured from earlier Tevatron results. The large number of grid points generated is why a fast Monte Carlo was used instead of the full detector simulation provided by the D0GEANT program.

In calculating the CL limits, for technical convenience the negative log likelihood ($L = -logP$) is used instead of the Poisson probability given by equation 7.9. The likelihood is generated for each grid point in $(\Delta\kappa, \lambda)$ space and the points are fit to a bilinear function. The likelihood function is shown in Figure 7.3.

To calculate the CL limits, contours are evaluated on the surface of the negative log-likelihood function. The confidence level desired is obtained by using the relation for standard-deviation errors given by $L_{max} - s^2/2$ where (s) is the standard-deviation. The contours are shown in Figure 7.4. The two contours shown correspond to one-degree-of-freedom CL limits of 95% and 68% which correspond to 1.96σ and 1σ. It is common to quote the limits of one coupling when the other coupling is fixed to the Standard Model value.

The 'axis' limits are shown below, in Table 7.3.

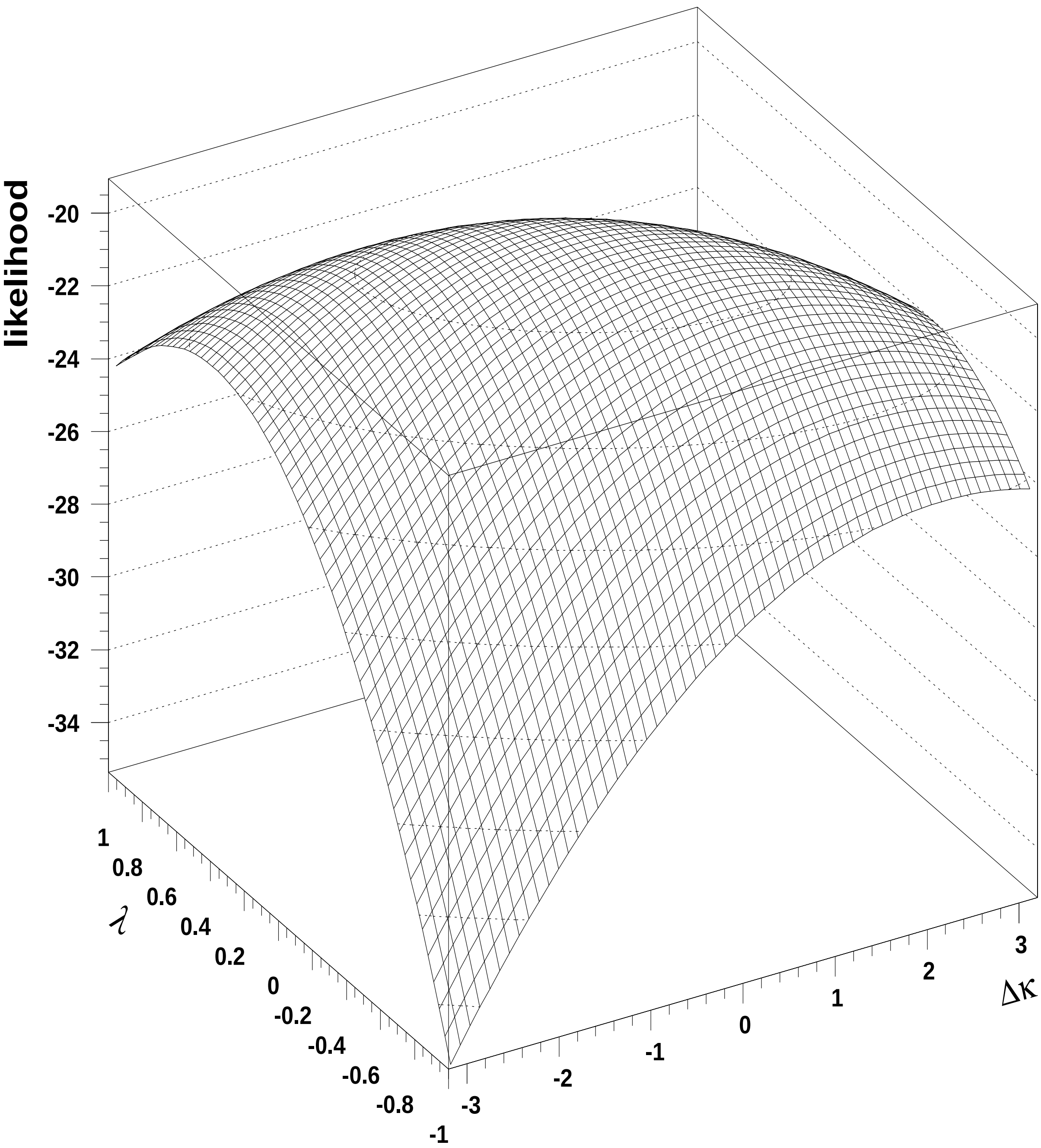

Figure 7.3: The 95% CL contour negative log-likelihood function fit to a bilinear function. The function peaks around the Standard Model predicted valuse of $\Delta\kappa$,$\lambda = 0$.

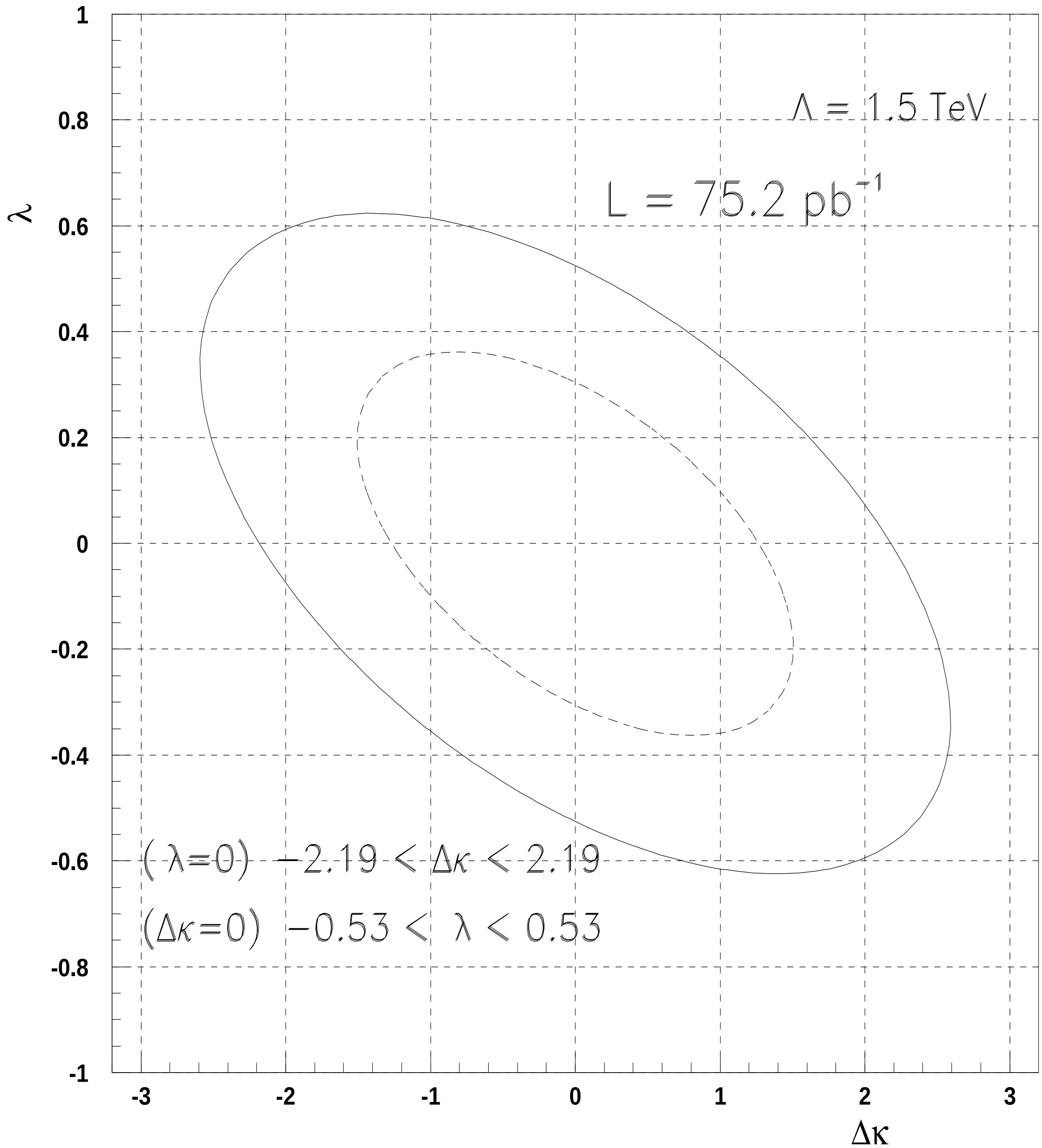

Figure 7.4: The CL limits on $\Delta\kappa$ and λ from the cross section measurement. The two contours are for the 95% and 68% CL limits. The dipole form factor scale of $\Lambda = 1.5$ TeV was used.

Table 7.3: Cross section limits from $W\gamma \rightarrow \mu\nu\gamma$

	95% axis limits	
$-2.2 < \Delta\kappa < 2.2$		$-2.2 < \tilde{\kappa} < 2.3$
$-0.53 < \lambda < 0.53$		$-0.53 < \tilde{\lambda} < 0.53$
	Unitarity limits	
$\lvert\Delta\kappa\rvert < 3.3$		$\lvert\tilde{\kappa}\rvert < 23.3$
$\lvert\lambda\rvert < 1.8$		$\lvert\tilde{\lambda}\rvert < 1.8$

7.3.2 Limits from Fitting the p_T^γ Spectrum

The limits obtained from the total cross section have one advantage; they are relatively easy to calculate. However, limits from the total cross section are sensitive to overall normalization factors, i.e., luminosity, efficiencies, and QCD corrections. A more sophisticated method to obtain limits on anomalous couplings employs fits to the shape of kinematical distributions which are sensitive to anomalous couplings. By fitting to the shape of distributions, there is much less sensitivity to overall normalization factors. Also, differential distributions contain more information and usually result in tighter limits.

The differential distribution which is most sensitive to anomalous couplings is the p_T^γ distribution. Figure 2.4 shows how the p_T^γ spectrum varies with anomalous couplings. The good resolution of the photon energy means the results are essentially not affected by smearing affects. Also, the shapes of the dominate backgrounds are well understood, which allows this method to be valid. Since the photon is common to both the muon and electron channels, combining the results from both channels is also fairly straightforward. In combining channels, the photon is smeared the same for both channels, whereas if an invariant mass was used, it would have to be treated differently for the different decay modes of the W boson.

In fitting to the shape of the p_T^γ distribution, it is possible to use either a binned or unbinned method. The binned method is used here for a few reasons. The unbinned fits rely on the exact shape of the background over the entire kinematic range, whereas a binned fit decreases the sensitivity of small fluctuations in the background. Since the number of photons expected decreases as the photon p_T increases, the bin size increases with increasing photon p_T. Also the binned fit avoids the problem that arises from smearing the data points with the known detector resolutions. By choosing bins which are wide enough compared with the detector resolutions, this problem is avoided. For large statistics, the estimators of the parameters for a given distribution should not depend on bin size, but for small statistics, this is generally not the case. The bin width should be much larger than the resolution of the data that is binned, but at the same time, there should be a sufficient number of bins to reflect as much detail as possible about the shape.

The same likelihood method is used as was used for the total cross section. For each bin, a Poisson likelihood is given as:

$$P_i = \frac{e^{-(b_i + \mathcal{L}\varepsilon\sigma_i)}(b_i + \mathcal{L}\varepsilon\sigma_i)^{n_i}}{n_i!} \tag{7.11}$$

where n_i is the number of events in the ith bin. Therefore, the probability of observing the given distribution, assuming uncorrelated bins (ok since the bins are much wider than the photon energy resolution) is given by the following relation:

$$P = \prod_{i=1}^{N} \frac{e^{-(b_i+\mathcal{L}\varepsilon\sigma_i)}(b_i + \mathcal{L}\varepsilon\sigma_i)^{n_i}}{n_i!} \tag{7.12}$$

where N_b is the number of bins in the histogram.

The data should be binned in such a way as to have a reasonable number of events in each bin. Since the spectrum is falling off as the photon transverse energy increases, the bin size increases with increasing p_T^γ. The standard method of having approximately equal number of events per bin would result in the last bin extending to some large value, p_T^{max}, independant of the highest p_T photon event. This would however neglect a major difference between Standard Model behavior and that predicted by anomalous couplings. For the Standard Model case, the events are concentrated in the low p_T region, while in the case of anomalous couplings, a large excess at high p_T is expected. The events with the highest observed p_T therefore contains essential information about the limits on the anomalous couplings. By having the last bin extend to this p_T^{max}, one ignores the information about the highest p_T event. In order to maximize the sensitivity to the anomalous couplings, the last bin is chosen so it contains no events. This uses the 'null experiment' [45] approach to increase the sensitivity to the anomalous couplings. The last E_T bin should be chosen slightly above the E_T of the highest E_T photon so the smearing affect could not fluctuate the last data point into the last bin. By using this method of introducing a bin with zero events contained in it, the results are more or less insensitive to the number of bins introduced as long as there are bins which contain the observed events and a bin which is empty.

The bin size along with the number of events in each bin and the estimated background in each bin are shown in Table 7.4. As with the cross section

Table 7.4: Information about bins used in the fit to the p_T^γ spectrum

p_T^γ Bin (GeV/c)	Number Observed	Background
10 - 15	22	10.1
15 - 20	18	5.1
20 - 30	15	4.0
30 - 60	3	2.6
60 and above	0	1.1

likelihood fit, the likelihood surface for the fit to the p_T^γ spectrum is found using a bilinear function given by the following form:

$$\frac{d\sigma(\Delta\kappa,\lambda)}{dp_T^\gamma} = \frac{d\sigma_{SM}}{dp_T^\gamma}(p_T^\gamma)+a(p_T^\gamma)\Delta\kappa+b(p_T^\gamma)\Delta\kappa^2+c(p_T^\gamma)\lambda+d(p_T^\gamma)\lambda^2+e(p_T^\gamma)\Delta\kappa\lambda, \tag{7.13}$$

where the coefficients are functions of the photon transverse momentum. The same grid spacing is used for this fit, namely a grid of 17×17 points with a spacing of 0.3 for both $\Delta\kappa$ and λ The contours of the 95% and 68% CL limits for $\Delta\kappa$ and λ are shown in Figure 7.5. The axis limits are given in Table 7.5. The resulting limits in this analysis are somewhat tighter than those obtained from the total cross section fit. In the following section the results presented here are combined with the results from an analysis of the process $W\gamma \rightarrow e\nu\gamma$, to produce the tightest limits on the anomalous couplings from our $W\gamma$ data .

Table 7.5: p_T^γ Limits from $W\gamma \to \mu\nu\gamma$

	95% axis limits	
$-1.95 < \Delta\kappa < 1.95$		$-1.94 < \tilde{\kappa} < 1.96$
$-0.52 < \lambda < 0.52$		$-0.52 < \tilde{\lambda} < 0.52$
	Unitarity limits	
$\lvert\Delta\kappa\rvert < 3.3$		$\lvert\tilde{\kappa}\rvert < 23.3$
$\lvert\lambda\rvert < 1.8$		$\lvert\tilde{\lambda}\rvert < 1.8$

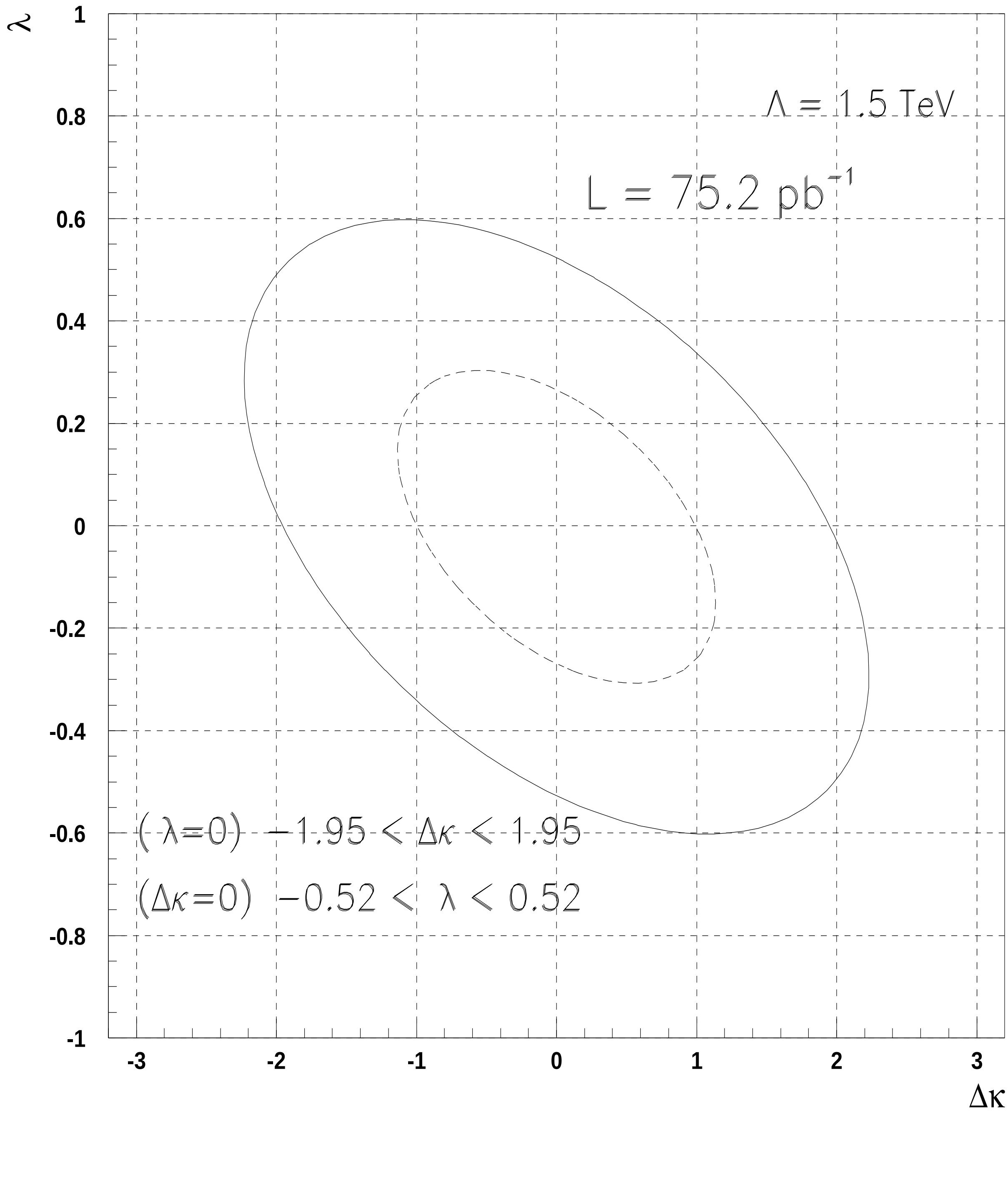

Figure 7.5: The CL contours on $\Delta\kappa$ and λ from a fit to the p_t^γ spectrum. The two contours are for the 95% and 68% CL limits. The dipole form factor scale of $\Lambda = 1.5$ TeV was used.

7.3.3 Combined Limits on Anomalous Couplings

The primary focus of this work is the study of $W\gamma$ production, with the $W \rightarrow \mu\nu$ decays. To obtain the tightest limits possible with the DØ data, the results from this analysis of $W\gamma \rightarrow \mu\nu\gamma$ events are combined with results from the electron channel [58]. Also, both the electron and muon channels from the earlier data run (run 1A) are combined into this analysis to produce the tightest possible limits on the anomalous couplings. The four different channels (1A electron and muon, 1B electron and muon) are treated as four different experiments with each experiment having its own likelihood. The likelihoods are combined for the four different channels and any common systematics are taken into account. More details on the combined analysis can be found in [59].

A summary of all the calculated signal and background events for the four different channels is shown in Table 7.6. As the table shows, the luminosity for Run 1A is about a factor of five less than the Run 1B data sample. The kinematic cuts for the electron channel are somewhat tighter due to the better resolution of the electromagnetic calorimeter. The electron E_T cut and the $\not{E}_T$ are both at 25 GeV, while the fiducial cuts for the electron are similar to those of the photon: $|\eta| < 1.1$ and $1.5 < |\eta| < 2.5$. The remaining kinematic and fiducial cuts are similar to those made in the muon channel. In the electron channel, the photon identification cuts are slightly different; in addition to requiring no track, a hits-in-road cut is also required. This cut looks for hits in a narrow road in the central tracker about the photon position. If there are more hits than a certain threshold, the event fails the requirement. The electron identification cuts are similar to the photon ID criteria, except a track match is required.

Table 7.6: Summary of signal and backgrounds.

	Run 1a $e\nu\gamma$	Run 1a $\mu\nu\gamma$	Run 1b $e\nu\gamma$	Run 1b $\mu\nu\gamma$
Luminosity	13.8 pb^{-1}	13.8 pb^{-1}	75.3 pb^{-1}	75.2 pb^{-1}
Backgrounds				
W + jets	1.7 ± 0.9	1.3 ± 0.7	11.5 ± 2.3	15.5 ± 4.5
$Z\gamma$	0.1 ± 0.1	2.7 ± 0.8	0.4 ± 0.1	5.2 ± 0.4
$W(\tau\nu)$	0.2 ± 0.1	0.4 ± 0.1	0.6 ± 0.1	1.7 ± 0.3
Other ($t\bar{t}$, WW)	-	-	0.7 ± 0.1	0.9 ± 0.3
Total BKG	2.0 ± 0.9	4.4 ± 1.1	13.2 ± 2.3	23.3 ± 4.6
# Observed	11	12	46	58
Total Signal	$9.0^{+4.2}_{-3.1}$	$7.6^{+4.4}_{-3.2}$	$32.8^{+7.8}_{-6.8}$	$34.7^{+8.7}_{-7.6}$

A combined cross section can be calculated from the results of Table 7.6. The cross section is found to be:

$$\sigma(p\bar{p} \rightarrow W\gamma + X) \times \mathrm{BR}(W \rightarrow \ell\nu) = 11.8^{+1.7}_{-1.6} \pm 1.6\ (syst)\ \pm 1.0\ (lum)\ \mathrm{pb}.$$

As before the statistical error is from Poisson statistics which is valid for small statistics. The systematic uncertainty includes the uncertainty in the amount of background in each channel and the uncertainties in the trigger, lepton ID, and all photon uncertainties. Each uncertainty is weighted by the amount of integrated luminosity in each experiment. For the four experiments, there consists a total of 127 observed events with a calculated signal of $84.4^{+12.3}_{-11.3}$ events. The characteristic spectra shown in Figure 7.6.

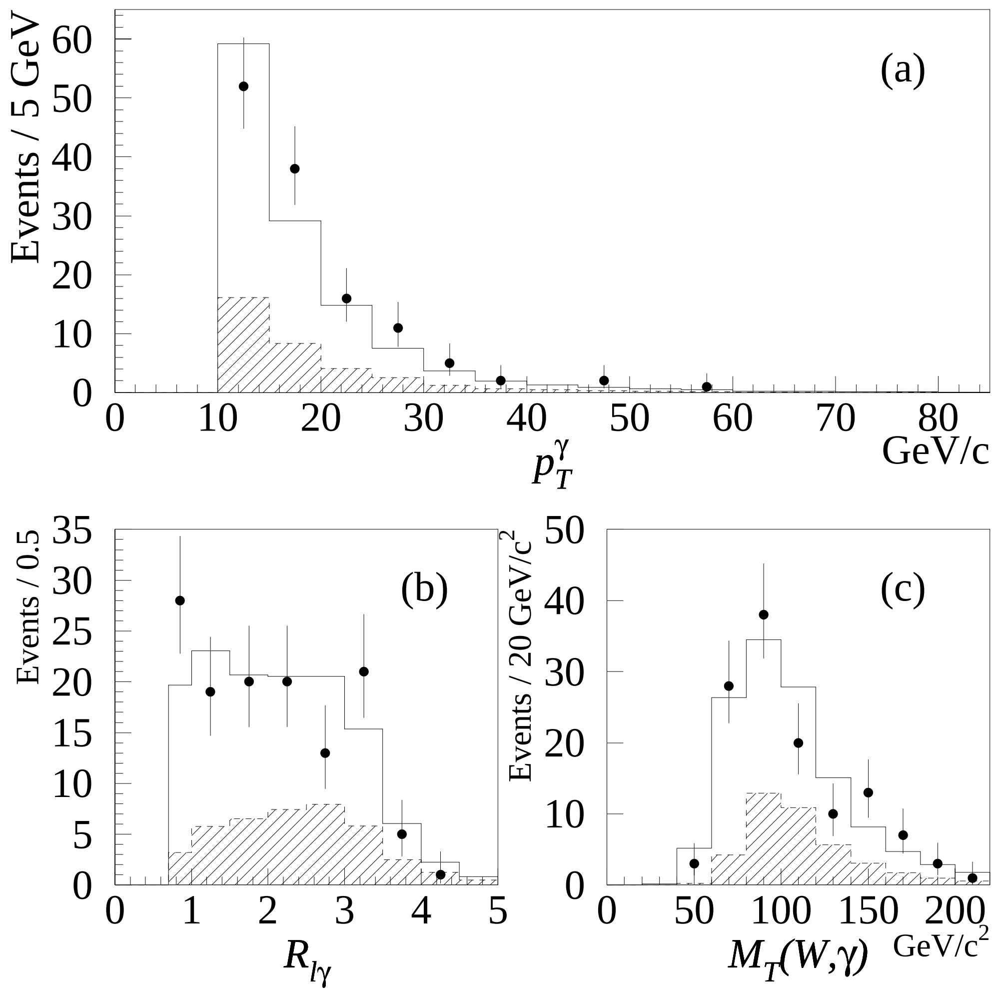

Figure 7.6: (a) The p_T^γ spectrum for the 127 Run 1 $W\gamma$ candidates. The $\Delta R_{\ell\gamma}$ and $M_T(\gamma\ell;\nu)$ distributions (b,c) are also shown. The points are the data with 1σ error bars. The solid histograms are the Standard Model Monte Carlo predictions plus the background estimates (shown as shaded histograms).

All the systematic errors for the four experiments are shown in Table 7.7. When combining more than one analysis, it is critical to properly take into account the correlated and uncorrelated errors of each experiment. Table 7.8

shows uncorrelated and correlated components of the systematic uncertainties. As the table shows, the luminosity and QCD background are completely correlated with each other. Also, various components of efficiencies are correlated within a given channel for both of the data taking runs.

Table 7.7: The values of the nuisance parameters used in the limits setting procedure.

Source of error	Nuisance Parameters			
	$e\nu$ channel Run 1a	$\mu\nu$ channel Run 1a	$e\nu$ channel Run 1b	$\mu\nu$ channel Run 1b
Photon, Luminosity and Theoretical				
Luminosity Uncertainty	5.4%	5.4%	12.%	12.%
Structure function choice	6.0%	6.0%	6.0%	6.0%
Structure function scale	1.0%	1.0%	1.0%	1.0%
$p_T^{W\gamma}$ kick	3.9%	3.9%	3.9%	3.9%
Conversion Probability	5.0%	5.0%	5.0%	5.0%
Random track overlap	1.0%	1.0%	0.5%	0.5%
Photon ID efficiency	7.0%	7.0%	3.1%	0.5%
Total ($\sigma_{\mathcal{L}}$)	12.5%	12.5%	15.5%	15.1%
Leptons				
Trigger and ID efficiency (σ_{ε})	5.2%	11.0%	1.3%	6.8%
Backgrounds				
Total Background (σ_b)	50.0%	50.0%	25.4%	28.0%

Figure 7.7 shows the DØ combined contour limits for the entire Run 1 data sample. Two DØ contours are shown which correspond to 95% CL intervals for both one degree of freedom and two degrees of freedom.

The combined limits on anomalous couplings from both the muon and electron channels are show in Table 7.9. These are currently the tightest limits in the world; more will be said about this in the conclusions.

Table 7.8: The (un)correlated components of the nuisance parameters

	Correlated Uncertainty	Uncorrelated Uncertainty			
		Run 1a		Run 1b	
		$e\nu$	$\mu\nu$	$e\nu$	$\mu\nu$
Luminosity + photon	10.3%	6.9%		7.3%	6.6%
Run 1 $\sigma_{\mathcal{L}}$	12.4%				
QCD background	25.0%	43.0%		—	
Run 1 σ_b	28.5%				
Electron ID	—	5.2%	—	1.3%	—
Run 1 σ_e	2.4%				
Muon ID	—	—	11.0%	—	5.9%
Run 1 σ_μ	6.9%				

Table 7.9: p_T^γ Limits from combined analysis of $W\gamma \to \mu\nu\gamma$ and $W\gamma \to e\nu\gamma$

	95% axis limits	
$-0.98 < \Delta\kappa < 1.01$		$-0.99 < \tilde{\kappa} < 1.00$
$-0.33 < \lambda < 0.31$		$-0.32 < \tilde{\lambda} < 0.32$
	Unitarity limits	
$\lvert\Delta\kappa\rvert < 3.3$		$\lvert\tilde{\kappa}\rvert < 23.3$
$\lvert\lambda\rvert < 1.8$		$\lvert\tilde{\lambda}\rvert < 1.8$

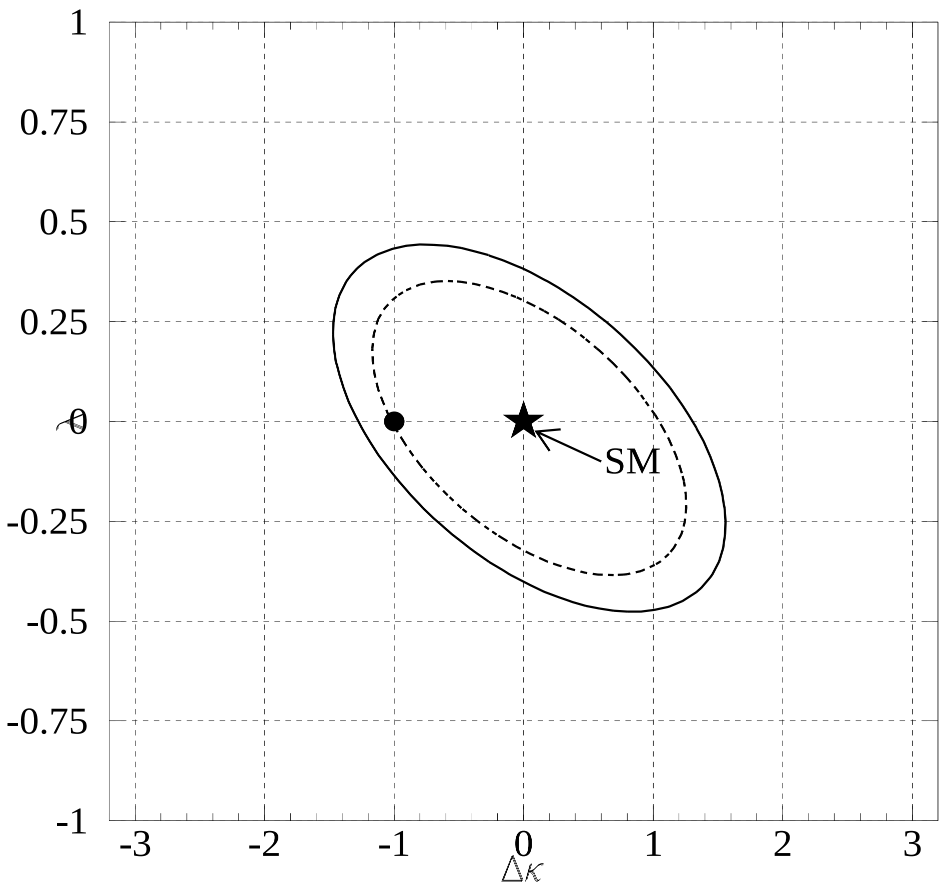

Figure 7.7: Contour plots for 95% CL limits for both one degree of freedom and two degrees of freedom on the anomalous couplings, $\Delta\kappa$ and λ, for the combined analysis of $W\gamma \rightarrow \mu\nu\gamma$ and $W\gamma \rightarrow e\nu\gamma$ events.

Chapter 8

Conclusions

A test of the electroweak sector of the Standard Model was performed using the Run 1b data sample from the Tevatron. In particular, the $WW\gamma$ interaction was probed by searching for W plus photon events with the W decaying into a muon and neutrino. The electron channel was combined with the muon channel to give a single combined analysis for $W\gamma$ production, which was further extended by including Run 1a data.

One hundred and twenty-seven $W\gamma$ candidates were observed with an estimated signal of $84.4^{+12.3}_{-11.3}$ events and a background of 42.9 events for both the leptonic decay channels, from both the Run 1a and Run 1b data samples. The results are determined using a form-factor behavior which is necessary to preserve unitarity. In the analysis a form-factor scale of 1.5 TeV is used with a dipole form-factor. With these parameters, limits on the anomalous couplings ($\Delta\kappa$, λ) are extracted from the data using a fit to the photon transverse momentum distribution. The limits from the combined analysis are shown below.

95% axis limits	
$-0.98 < \Delta\kappa < 1.01$	$-0.99 < \tilde{\kappa} < 1.00$
$-0.33 < \lambda < 0.31$	$-0.32 < \tilde{\lambda} < 0.32$

These are currently the tightest limits in the world on anamalous couplings, derived from a direct measurement. Assuming the CP-violating couplings are zero, the $U(1)_{EM}$-only coupling ($\kappa = 0, \lambda = 0$) is excluded at the 86% CL. Making the further assumption that $\lambda = 0$, this point is excluded at the 95% CL. The exclusion of this point is direct evidence that the photon does not simply couple to just the electric charge of the W boson. It is interesting to compare the results here with other curent measurements from different experiments. Figure 8.1 shows the contour limits from the DØ combined analysis for the entire Run 1 data sample. The results are compared with those from CDF and CLEO. The CDF result is based on a portion of the Run 1B data sample and the CLEO result is derived from an analysis of the process $b \rightarrow s\gamma$ (b quark decaying into a strange quark plus a photon). Two DØ contours are shown which correspond to 85% and 68.2% CL intervals for two degrees of freedom. The CLEO and CDF results are for 95% CL intervals for one degree of freedom, which should be compared to the 85% CL interval for DØ.

Measurements which limit the anomalous couplings should continue to improve in the future. In the short term, improved sensitivity could be achieved by combining the results from CDF and DØ into one result. In the not so dis-

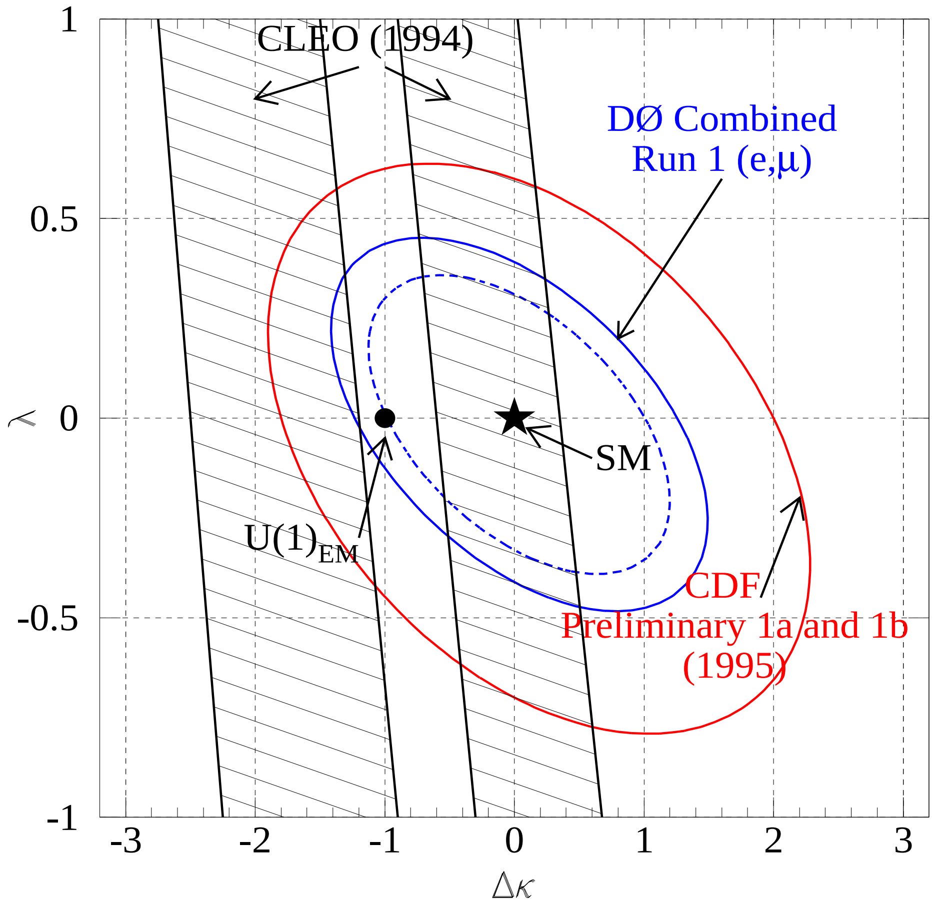

Figure 8.1: Comparison of the 95% CL limits (both one degree of freedom (inner) and two degrees of freedom (outer)) on $\Delta\kappa$ and λ from Runs 1a and 1b (both e and μ channels) with the published CLEO and preliminary CDF results. The CDF results use $e\nu\gamma$ and $\mu\nu\gamma$ events found in 67 pb^{-1} of data from a combined Run 1a and Run 1b analysis. The Run 1a DØ result was similar to the CDF (1995) ellipse. The direct experiments assume a dipole form factor scale of $\Lambda = 1.5$ TeV.

tant future, the upgraded Tevatron and LEP2 should improve the sensitivity on the anomalous couplings a significant amount. The LHC should be able to probe quartic couplings as well as trilinear couplings to gain insight into the electroweak syemetry breaking sector of the Standard Model. With the large amount of data sets expected from future experiments, many different aspects of the $WW\gamma$ interaction can be probed.

Appendix A

Event Variables

The three tables in this appendix show some relevant information for the 58 $W\gamma \rightarrow \mu\nu\gamma$ candidates. The first table shows some of the information about the muon in the event, the second table shows some information about the photon in the event, and the third table shows some kinematics of the events.

Table A.1: Muon Information for the 58 $W\gamma \rightarrow \mu\nu\gamma$ candidates

run	event	p_T	η	ϕ	Hfract(MTC)	$b\cdot$ dl
76143	2490	28.701	-0.98275E-01	1.0571	1.0000	0.64564
77548	10684	19.716	-0.46034	1.3924	1.0000	0.72590
79482	9467	16.436	-0.50137	5.7270	1.0000	0.75803
79489	9523	46.568	0.16554	2.8002	1.0000	0.63948
80887	23533	22.118	-0.54099	5.5709	1.0000	0.69573
81582	15292	60.734	-0.15408	6.1369	1.0000	0.63060
82155	7092	18.655	-0.66613	5.9340	1.0000	0.76593
82302	9433	21.389	-0.11100	0.61409	1.0000	0.62561
82694	28710	20.650	-0.19619	0.55218	1.0000	0.68396
82727	5318	67.514	-0.28077	3.8572	1.0000	0.62287
83077	8815	15.738	0.14955	2.4711	1.0000	0.61866
84226	15522	59.704	-0.53755	1.9349	1.0000	0.75845
84327	1524	90.152	0.44380	4.2145	1.0000	0.69227
84470	33136	17.786	-0.50676	2.2624	1.0000	0.77252
84695	43614	19.486	0.18162E-01	2.1054	1.0000	0.64002
85111	16843	26.092	0.30872	3.5803	1.0000	0.65294
85371	14595	39.547	-0.30443	6.2046	1.0000	0.64913
85459	17197	25.460	0.17790	0.28597	1.0000	0.64175
85796	19063	27.116	0.52555	5.6029	1.0000	0.75905
86042	12485	68.628	0.29907	3.1605	1.0000	0.65569
86102	21005	142.51	-0.29840	2.9725	1.0000	0.65176
86178	37140	54.743	0.12037	3.4782	1.0000	0.63756
86258	6265	42.730	-0.31169	1.0886	0.75000	0.71579
87064	11067	22.176	0.15223	3.0503	1.0000	0.63302
87070	19605	15.722	-0.12098	5.3203	1.0000	0.64699
87104	5959	23.971	-0.68744	2.7362	1.0000	0.84307
87298	8351	36.085	0.10343	5.7707	1.0000	0.62885
87446	21957	24.610	-0.21110	0.37398	1.0000	0.64947
87482	7191	34.497	0.61962	5.8223	1.0000	0.79633
87537	28487	32.604	0.64170	2.7577	1.0000	0.79068
87556	7766	15.761	0.24704	1.3305	0.75000	0.66139
87603	6415	64.553	0.45721	5.7568	1.0000	0.70575
87711	9672	78.698	-0.29258	3.3630	1.0000	0.64640
87823	42272	23.708	0.31708E-01	4.2113	1.0000	0.64195
87855	19627	23.533	-0.50621	5.7725	1.0000	0.70919
88044	9513	22.134	-0.37612	4.1708	1.0000	0.67886
88203	15514	17.007	0.63309	0.43540	1.0000	0.74839
88506	8596	25.471	0.39197	3.4882	1.0000	0.69066
88681	25934	37.763	-0.14397	0.82213E-01	0.75000	0.63104
88698	3569	20.828	-0.22595	4.2277	1.0000	0.67001
89554	16819	29.530	-0.36068	5.3466	1.0000	0.71183
89687	1492	30.560	-0.73891	0.45952E-01	1.0000	0.82233
90232	12157	31.453	0.20790	4.1699	1.0000	0.66457
90278	2155	68.531	-0.51595	5.2339	1.0000	0.75727
90310	11016	189.13	0.48790	1.1590	1.0000	0.71906
90371	4400	15.428	0.20303	0.58069	1.0000	0.65405
90404	3933	83.432	0.55048	3.7421	1.0000	0.75886
90424	11070	204.81	0.16528E-01	2.5081	1.0000	0.62142
90499	183	41.914	0.86685	1.5671	1.0000	0.86213
90684	3204	21.224	0.43138	0.11290	1.0000	0.69250
90757	25573	17.696	-0.62917	6.1432	1.0000	0.73258
90914	9173	31.186	-0.53820	4.2407	1.0000	0.74443
91361	16446	36.239	-0.19487E-01	3.3464	1.0000	0.63240
91876	19500	36.219	-0.66911	1.9421	1.0000	0.87494
91903	3108	39.448	0.55112	1.4569	1.0000	0.73558
91948	9566	48.426	0.33650	0.70692	1.0000	0.64233
92014	9369	33.352	-0.21975	6.0191	1.0000	0.63152
92226	14119	16.239	0.48591E-01	3.1069	1.0000	0.62765

Table A.2: Photon Information for the 58 $W\gamma \rightarrow \mu\nu\gamma$ candidates

run	event	E_T	η	ϕ	χ^2	isolation
76143	2490	12.065	0.62488	1.6457	24.137	0.95955E-01
77548	10684	27.826	0.50716E-02	5.8948	28.129	0.41894E-01
79482	9467	18.480	-0.78014	4.7806	48.885	0.67897E-01
79489	9523	35.402	0.90355	0.78373E-02	14.914	0.31050E-01
80887	23533	12.652	-0.97018	6.2552	57.059	0.36833E-01
81582	15292	19.127	-1.0902	2.9063	14.841	0.31637E-01
82155	7092	15.799	0.41550	4.4645	45.007	0.30245E-01
82302	9433	26.488	-0.87463	2.0415	28.030	0.30912E-01
82694	28710	21.422	-2.2094	3.6099	39.371	0.23109E-01
82727	5318	14.131	-2.1959	1.0444	43.353	0.17392E-01
83077	8815	22.566	1.2397	1.4170	53.267	0.45461E-01
84226	15522	10.490	0.97846	3.0154	51.859	0.66859E-01
84327	1524	19.320	-1.6939	1.2603	18.734	0.25055E-01
84470	33136	10.776	-0.77726	3.9635	55.600	0.67492E-01
84695	43614	11.224	0.92906	2.5889	51.255	0.35753E-01
85111	16843	13.295	0.95196	6.2253	50.083	0.61872E-01
85371	14595	29.331	1.7730	0.25756	31.980	0.35273E-01
85459	17197	11.197	-2.0675	2.8990	74.598	0.32631E-01
85796	19063	15.164	0.97790	0.74165	21.669	0.38489E-01
86042	12485	17.721	-0.69097	6.0118	28.750	0.83426E-01
86102	21005	18.121	0.43152	0.15545	80.413	0.34332E-01
86178	37140	37.578	-0.78613	0.30744	12.555	0.21018E-01
86258	6265	13.381	1.7295	4.7935	46.990	0.45035E-01
87064	11067	34.092	-1.9628	2.7033	41.450	0.42757E-01
87070	19605	18.219	-0.45524	3.4799	20.584	0.65325E-01
87104	5959	10.926	0.61568	1.2307	25.548	0.65242E-01
87298	8351	19.091	-2.3807	1.2971	44.304	0.58294E-01
87446	21957	15.739	0.68206	4.2258	26.063	0.24557E-01
87482	7191	21.806	1.8631	2.4236	167.22	0.49775E-01
87537	28487	22.874	-0.89226	0.27327	40.770	0.26363E-01
87556	7766	11.299	-1.8092	1.3618	53.828	0.98480E-01
87603	6415	17.520	1.4828	2.7626	43.785	0.49141E-01
87711	9672	12.476	-0.30733	0.23468	12.065	0.34195E-01
87823	42272	17.443	-0.51872	4.9406	31.768	0.26069E-01
87855	19627	16.867	0.38859	2.8676	78.639	0.85542E-01
88044	9513	24.799	-0.25265	0.57377	40.716	0.39844E-01
88203	15514	24.484	0.38635E-01	1.2598	17.038	0.36310E-01
88506	8596	20.248	-0.38098E-01	2.5967	19.941	0.70231E-01
88681	25934	15.436	-1.8847	0.72153	79.102	0.45045E-02
88698	3569	16.862	0.82052E-01	3.4632	13.728	0.81031E-01
89554	16819	12.951	-0.64020	0.41395	21.674	0.24629E-01
89687	1492	16.571	1.7284	4.1163	24.914	0.11212E-01
90232	12157	13.824	0.86932E-01	0.53254E-01	41.956	0.44811E-01
90278	2155	23.250	-1.5325	1.8074	27.545	0.65123E-01
90310	11016	28.265	-0.18747	4.3278	52.259	0.88748E-01
90371	4400	12.182	0.69379	2.9806	44.309	0.40332E-01
90404	3933	12.248	2.0094	1.3560	98.846	0.45120E-01
90424	11070	23.089	1.7554	0.89790	72.293	0.78927E-01
90499	183	18.398	0.60125	2.6008	76.499	0.80437E-01
90684	3204	57.579	0.44989	1.2541	73.936	0.72196E-01
90757	25573	10.779	-0.78385	5.4343	93.282	-0.15038E-01
90914	9173	11.190	-0.49461	2.3824	12.674	-0.31026E-01
91361	16446	25.318	0.25620	5.1732	19.061	0.67386E-01
91876	19500	13.095	-0.93046	2.7027	11.354	0.84467E-01
91903	3108	16.031	-1.4379	2.2807	46.577	0.33520E-01
91948	9566	29.242	-0.27653E-01	5.1440	13.931	0.61788E-01
92014	9369	10.248	0.47716	1.1377	23.247	-0.22092E-01
92226	14119	14.858	0.89295	2.1353	78.178	0.64809E-01

Table A.3: Kinematic Information for the 58 $W\gamma \rightarrow \mu\nu\gamma$ candidates

run	event	# of jets	$\Delta R(\mu,\gamma)$	M_T
76143	2490	1	0.93239	82.099
77548	10684	0	1.8407	73.999
79482	9467	0	0.98655	65.837
79489	9523	0	2.8883	111.65
80887	23533	1	0.80771	60.882
81582	15292	2	3.1929	140.30
82155	7092	0	1.8246	67.569
82302	9433	1	1.6188	84.396
82694	28710	2	3.6609	84.523
82727	5318	2	3.4028	163.98
83077	8815	0	1.5164	87.576
84226	15522	0	0.88000	138.58
84327	1524	0	3.6466	222.75
84470	33136	1	1.7225	48.219
84695	43614	0	1.0313	64.744
85111	16843	1	2.7220	65.074
85371	14595	0	2.1045	167.19
85459	17197	0	3.4453	79.345
85796	19063	0	1.4921	67.904
86042	12485	1	3.0183	155.03
86102	21005	0	2.9101	304.80
86178	37140	0	3.2418	119.02
86258	6265	0	3.2884	119.54
87064	11067	0	2.1433	148.82
87070	19605	0	1.8706	58.810
87104	5959	0	1.9912	70.878
87298	8351	0	3.0733	133.84
87446	21957	0	2.5902	87.368
87482	7191	1	3.1410	89.851
87537	28487	0	2.9199	94.419
87556	7766	1	2.0565	60.296
87603	6415	0	3.1649	129.27
87711	9672	0	3.1283	161.45
87823	42272	0	0.91370	78.088
87855	19627	0	3.0396	61.681
88044	9513	4	2.6890	62.332
88203	15514	3	1.0164	79.614
88506	8596	0	0.98981	90.346
88681	25934	0	0.78000	101.08
88698	3569	0	0.82426	71.015
89554	16819	0	1.3791	82.103
89687	1492	1	3.3142	122.33
90232	12157	1	2.1699	87.653
90278	2155	0	3.0322	143.37
90310	11016	2	3.1868	392.56
90371	4400	2	2.4496	52.277
90404	3933	1	2.7968	180.78
90424	11070	0	2.3699	476.63
90499	183	0	1.0673	116.40
90684	3204	0	1.1414	156.43
90757	25573	0	0.72559	62.149
90914	9173	0	0.98000	72.660
91361	16446	1	1.8475	107.04
91876	19500	0	0.80428	90.449
91903	3108	0	2.1528	157.83
91948	9566	4	1.8817	85.708
92014	9369	2	1.5655	62.837
92226	14119	0	1.2872	65.143

Bibliography

[1] Particle Data Group, *Phys. Rev* **72**, 1173 (1994).

[2] V.D. Barger and R.J.N. Phillips, *Collider Physics*, Addison-Wesley Publishing Co., (1987)

[3] C. Quigg, *Gauge Theories of the Strong, Weak, and Electromagnetic Forces,* Addison-Wesley, 1983.

[4] F. Halzin and A. Martin, *Quarks and Leptons*, John Wiley & Sons, Inc., 1984

[5] M. Guidry, *Gauge Field Theories: An Introduction with Applications,* John Wiley & Sons, Inc., 1991.

[6] M. Kobayashi and T. Maskawa, Prog. *Theor. Phys.* **49** (1973)

[7] Review of Particle Properties, PDG, *Phys. Rev.* **D50** (1994) 1279-1308.

[8] S. Godfrey, *Quartic Gauge Boson Couplings,* in International Symposium on Vector Boson Interactions, edited by U. Baur, S. Errede, T. Müller, AIP Press (1996) p. 209.

[9] U. Baur, E.L. Berger, *Phys. Rev.* **D41**, 1476 (1990).

[10] U. Baur, D. Zeppenfeld, *Nucl. Phys.* **B308**, 127 (1988).

[11] J.M. Cornwall, D.N. Levin, G. Tiktopolous, *Phys. Rev. Lett.* **30**, 1268 (1973); Phys. Rev. **D10**, (1974) 1145; C.H. Llewellyn Smith, Phys. Lett. **46B**, (1973) 233; S.D. Joglekar, Ann. of Phys. **83**, (1974) 427.

[12] J. Cortes, K. Hagiwara, F. Herzog, *Nuclear Phys.* **B278** 26 (1986).

[13] R.W. Brown, *Understanding Something About Nothing: Radiation Zeros,* in International Symposium on Vector Boson Interactions, edited by U. Baur, S. Errede, T. Müller, AIP Press (1996) p. 261.

[14] T. Hahn, *Exact and Approximate Radiation Amplitude Zeros - Phenomenologica Aspects,* in International Symposium on Vector Boson Interactions, edited by U. Baur, S. Errede, T. Müller, AIP Press (1996) p. 224.

[15] J. Ohnemus, *QCD Corrections to Diboson Production,* in International Symposium on Vector Boson Interactions, edited by U. Baur, S. Errede, T. Müller, AIP Press (1996) p. 60.

[16] R. Walczak, *W and Z Boson Production at HERA,* in International Symposium on Vector Boson Interactions, edited by U. Baur, S. Errede, T. Müller, AIP Press (1996) p. 198.

[17] S.M. Playfer, *Rare b Decays and Anomalous Couplings,* in International Symposium on Vector Boson Interactions, edited by U. Baur, S. Errede, T. Müller, AIP Press (1996) p. 124.

[18] T. Kinoshita, W.J. Marciano, *Quantum Electrodynamics,* in Vol. 7 of *"Advanced Series on Directions in High Energy Physics",* edited by T. Kinoshita. World Scientific (1990).

[19] S. Abachi *et al.* (DØ Collaboration), *Nucl. Instr. and Methods* **A338** (1994) 185.

[20] FNAL, Design report Tevatron 1 project, FNAL internal note, September 1984.

[21] M. P. Church and J. P. Marriner, Ann. *Rev. Nucl. Part. Sci.,* **43**, 1993.

[22] *FNAL, A report of the design of the Fermi National Accelerator Laboratory superconduction accelerator,* FNAL internal note, May 1979

[23] D.A. Edwards, M.J. Syphers, *An Introduction to the Physics of High Energy Accelerators,* John Wiley & Sons, Inc., 1993.

[24] J. Thompson, *Introduction to Colliding Beams at Fermilab,* preprint FERMILAB-TM-1909 (1994) unpublished.

[25] N. Amos *et al.*, *Luminosity calculations for DØ.* DØ Note 2031, 1994

[26] Konrad Kleinknecht, *Detectors for Particle Radiation*, Cambridge University Press, 1987.

[27] J. F. Detoeuf *et al.*, *Nucl. Inst. Meth.,* **A265**, 1988

[28] A. R. Clark *et al.*, *Nucl. Inst. Meth.,* **A265**, 1989

[29] C. Fabjan, *Calorimetry in High Energy Physics,* In T. Ferbal, editor, Experimental Techniques in High Energy Physics, Addison-Wesley, 1987.

[30] C. Brown *et al.*, *Nucl. Inst. Meth.,* **A279**, 1989

[31] J. Bantly *et al., IEEE Trans on Nucl. Sci.* **41** (1994) 1274.

[32] M. Abolins *et al., IEEE Trans on Nucl. Sci.* **36** (1989) 384; Nucl. Instr. and Methods **A289** (1990) 543.

[33] D. Cutts, *et al., IEEE Trans. Nucl. Sci.* **36**, 1989.

[34] T. Behnke. *The Central Drift Chamber for the DØ Detector: Design, Construction, and Test.* Ph.D. thesis, State University of New York at Stony Brook, Stony Brook New York, 1989.

[35] Domenico Pizzuto. *DØ Central Tracking Chamber performance Studies.* Ph.D. thesis, State University of New York at Stony Brook, Stony Brook New York, 1991.

[36] Saul Youssef. *Comp. Phys. Comm.* **45**: 423-426, 1987.

[37] T. C. Awes *et al., Nucl. Inst. Meth.,* **A311**:130-138, 1991.

[38] T. Diehl and D. Hedin. *DØ Muon Level2 Filter.* DØ Note 1325, January 1992.

[39] C. Gerber *et al., Muon Momentum Determination.* DØ Note 2140, October 1994.

[40] N. J. Hadley. *Cone Algorithm for Jet Finding.* DØ Note 904, November 1989.

[41] Bob Kehoe. *Resolution Bias in Jet Response Measurement.* DØ Note 2052, 1994.

[42] R. Astur. *Correction of MET.* DØ Note 2088, 1994.

[43] Meena Narain. *Electron identification in the DØ detector.* In Carl H. Albright *et al.,* editors, The Fermilab Meeting: DPF 92, volume 2, 1678-1680. World Scientific, November 1992.

[44] E. Gallas, DØ Note # 2195 (1994), unpublished.

[45] G. Landsberg, *Test of the Standard Model of Electroweak Interactions by Measuring the Anomalous* $ZZ\gamma$ *and* $Z\gamma\gamma$ *Couplings,* Ph.D. Dissertation, SUNY @ Stony Brook (1994), unpublished.

[46] T. Diehl, Musmear Package Documentation, 1994, unpublished.

[47] M. Kelly, private communication.

[48] S. Glenn, private communication.

[49] N. Amos, J. Linnemann, R. Partridge, and L. Paterno. *Luminosity calculations for DØ.* DØ Note 2031, 1994.

[50] B. Choudhary, private communication.

[51] P. Quintas, private communication.

[52] J. Womersley, private communication.

[53] S. Jerger, private communication.

[54] Particle Data Group. *Physical Review D*, Particles and Fields. Volume 50 #3, 1281-1282. 1994.

[55] R. Raja, Q. Li-Demarteau, and S. Kunori. *D0GEANT*. DØ Note 1007, July 1990.

[56] S. Glenn. DØ Note 2846. *A Parametric Detector Simulation of Dibosons.* 1996.

[57] B. Kehoe and R. Astur. *Determination of the Hadronic Energy Scale of DØ Calorimetry.* DØ Note 2908, may 1996.

[58] M. Kelly. *Test of the Standard Model of Electroweak Interactions by Measuring the Anomalous $WW\gamma$ couplings at $\sqrt{s} = 1.8$ TeV.* Ph.D. thesis, Notre Dame, South Bend, Indiana. April 1996.

[59] Mike Kelly and Tom Fahland. DØ Note 3086. *The Run 1 $W\gamma$ Analysis.* 1996.